9-14-2017

Oblique Longwave Infrared Atmospheric Compensation

Daniel S. O'Keefe

Oblique Longwave Infrared Atmospheric Compensation

DISSERTATION

Daniel S. O'Keefe, Captain, USAF

AFIT-ENP-DS-17-S-030

DEPARTMENT OF THE AIR FORCE
AIR UNIVERSITY

AIR FORCE INSTITUTE OF TECHNOLOGY

Wright-Patterson Air Force Base, Ohio

AFIT-ENP-DS-17-S-030

OBLIQUE LONGWAVE INFRARED ATMOSPHERIC COMPENSATION

DISSERTATION

Presented to the Faculty

Graduate School of Engineering and Management

Air Force Institute of Technology

Air University

Air Education and Training Command

in Partial Fulfillment of the Requirements for the

Degree of Doctor of Philosophy

Daniel S. O'Keefe, B.S., M.S.

Captain, USAF

14 September 2017

AFIT-ENP-DS-17-S-030

OBLIQUE LONGWAVE INFRARED ATMOSPHERIC COMPENSATION

DISSERTATION

Daniel S. O'Keefe, B.S., M.S.
Captain, USAF

Committee Membership:

Kevin C. Gross, PhD (Chair)

Benjamin F. Akers, PhD (Member)

Joseph Meola, PhD (Member)

Michael A. Marciniak, PhD (Member)

ADEDEJI B. BADIRU, PhD
Dean, Graduate School of Engineering and Management

Abstract

This research introduces two novel oblique longwave infrared atmospheric compensation techniques for hyperspectral imagery, Oblique In-Scene Atmospheric Compensation (OISAC) and Radiance Detrending (RD). Current atmospheric compensation algorithms have been developed for nadir-viewing geometries which assume that every pixel in the scene is affected by the atmosphere in nearly the same manner. However, this assumption is violated in oblique imaging conditions where the transmission and path radiance vary continuously as a function of object-sensor range, negatively impacting current algorithms in their ability to compensate for the atmosphere. The techniques presented here leverage the changing viewing conditions to improve rather than hinder atmospheric compensation performance. Initial analyses of both synthetic and measured hyperspectral images suggest improved performance in oblique viewing conditions compared to standard techniques.

OISAC is an extension of ISAC, a technique that has been used extensively for LWIR AC applications for over 15 years, that has been developed to incorporate the range-dependence of atmospheric transmission and path radiance in identification of the atmospheric state. Similar to ISAC, OISAC requires the existence of near blackbody-like materials over the 11.73 micrometer water band. RD is a newer technique which features unsupervised classification of materials and identifies the atmospheric state which best detrends the observed radiance across all classes of materials, including those of low emissivity.

For an oblique synthetic scene with an atmosphere characterized by a MODTRAN Model 6 atmosphere, OISAC had a mean RMS error in transmission of (0.003, 0.005, 0.006) for the closest, middle, and furthest rows respectively. RD had comparable

RMS errors of (0.002, 0.003, 0.004), while FLAASH-IR, which had not been modified to account for the oblique geometry, had RMS errors of (0.052, 0.020, 0.194). For path radiance, OISAC, FLAASH-IR, and RD had mean RMS errors of (2.6, 4.1, 5.3), (47, 11, 121), and (1.1, 1.5, 2.3) microflicks. We also compared retrieved and true emissivities for a variety of materials using mean RMS and Pearson correlation. For roof slate, OISAC had a mean RMS error of (0.002, 0.003, 0.003) for the closest, middle, and furthest ranges and correlations of (1.000, 1.000, 0.999). FLAASH-IR had an RMS of (0.010, 0.029, 0.085) and correlations of (0.995, 0.987, 0.886). Finally, RD had an RMS of (0.002, 0.003, 0.005) and correlations of (1.000, 1.000, 0.999).

Acknowledgements

I would first and foremost like to acknowledge my Father in heaven, without which physical laws and their beauty would not even exist to be discovered. He not only blessed me with a passion for science and an opportunity to pursue the study of it, but I have been blessed with a supportive wife, prayerful family and friends, an incredibly sharp and encouraging advisor, and a vast suite of colleagues and professors always eager and available to help. The struggle to find a means of contributing to and advancing the scientific body of knowledge at all, let alone finishing within the brief window of time available, was a significant one for me. I could not have done it without every single individual's help. Lastly, I would like to thank God for giving me faith and hope for the future, however it unfolded. Thank you for adopting me as a son and giving me an identity and self-worth that is independent of my performance, of both my successes and failures. This work is for You.

Daniel S. O'Keefe

Table of Contents

Page

List of Figures

Figure Page

List of Tables

I. Introduction and Research Objectives

Remote sensing, which uses a sensor to measure radiation from a scene, has been applied across a wide variety of fields and applications. Some of these include detection and analysis of chemical and biological agents or investigating liquid and powder spills [11, 41], buried mines [18, 19] and disturbed earth in various soil types [15], tripwires [12], clouds [29, 37], aircraft coating degradation [44], and targets obscured by clutter [35] or vegetation [30]. Additionally, remote sensing is used in industrial process control [13], computer vision [45], facial recognition [16], the modeling and 3D surface reconstruction of transparent objects [26], highly reflective metallic objects [27], and dielectrics [3], and the classification and mapping of natural and resource objects, such as those related to vegetation, minerals, and atmosphere [8].

Passive remote sensing, in contrast to active remote sensing, is a subset of remote sensing in which the observer does not have control over illumination sources. This is a common technique for data collection, as it does not require active interrogation by the observation platform. Traditionally, overhead aircraft and satellites image scenes in nadir-viewing geometries; however, there has been a growing interest in capturing and analyzing scenes in oblique viewing geometries. These non-nadir observations not only allow for increased area coverage and reduced revisit times [2], but they also allow one to image scenes that may be dangerous for sensing platforms (e.g. in the monitoring of volcanic eruptions or forest fires) [38].

The focus of this research is to explore and tackle some of the unique complications associated with oblique viewing geometries, specifically, the impact from variable

path lengths throughout the scene. This research develops two oblique atmospheric compensation (AC) techniques which utilize the range-dependence of the measured radiance in a scene to compensate longwave infrared (LWIR) hyperspectral imagery in oblique scenarios: Oblique In-Scene Atmospheric Compensation (OISAC) and Radiance Detrending (RD).

1.1 Challenges of the Oblique Scenario

When trying to recognize materials in a scene, scenarios involving oblique viewing geometries face various challenges. First, difficulties arise from the fact that, since the path length varies across an oblique image, ground sample distance, transmission, and path radiance may all vary significantly. Standard atmospheric compensation algorithms, which were developed for nadir-viewing configurations, assume that these path lengths are nearly uniform across the scene. Thus, the more oblique the scene geometry, the more these assumptions are violated; the impact of variable path lengths will be explored in this research. Additionally, oblique viewing geometries tend to have longer slant paths through the more dense and humid part of the atmosphere, leading to more atmospheric absorption, larger atmospheric path radiances, weaker signals, a smaller usable band, fewer pixels on target and/or larger pixel adjacency effects, and jitter magnification leading to spectral mixing. When these smaller and mixed signals are analyzed, retrievals are more unstable and less accurate.[2, 25, 36] While the research here does not address this second set of challenges, they are factors to be considered when analyzing oblique hyperspectral datasets. Fig. 1 highlights the challenges identified in oblique imaging as compared to nadir imaging.

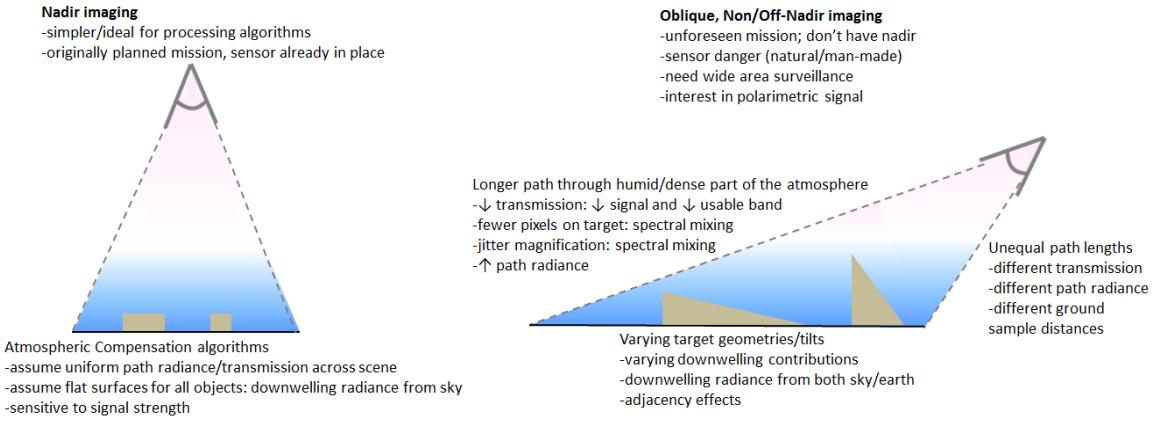

Figure 1. Comparison of nadir and oblique imaging.

1.2 Challenges of Oblique Atmospheric Compensation

Amid all of these oblique imaging challenges, this research hones in on improving oblique atmospheric compensation by distinctly accounting for transmission and path radiance differences. Much of the research in AC has been done for nadir or nearly nadir viewing geometries.[1, 14, 46] In these scenarios, an overhead sensor captures radiance from a scene and sensor-scene distance for all pixels throughout the scene is assumed to be nearly constant. However, there has been a growing need to detect targets in oblique-viewing geometries.[25] In oblique scenarios, the sensor-scene distance for the pixels throughout the image can vary greatly, depending on the viewing angle and altitudes involved. Since atmospheric path radiance and transmission depend heavily on the path length between the sensor and scene as explored in 2.2, oblique images may have considerable variation of these two atmospheric quantities. Applying nadir AC techniques to oblique images will lead to inaccurate, biased retrievals by ignoring the variability of transmission and path radiance across the image, which can significantly affect target detection, demonstrated later in Fig. 20.

Oblique AC is a relatively new area of study and limited work has been done to

tailor AC algorithms to this new operating scenario. Previous research in oblique AC has mainly been concerned with observing the impact of obliquely collected data on nadir algorithms [Adler-Golden] or segmenting the image before applying nadir techniques.[38] While direct or slightly modified applications of these nadir techniques have shown favorable results for oblique scenarios [2, 38], only a limited number of atmospheric conditions and ranges have been tested, and the nadir techniques do not capitalize on the additional information present in an obliquely viewed scene.

1.3 Research Objectives

This research aims to improve oblique atmospheric compensation of LWIR hyperspectral imagery, where detailed and highly accurate *a priori* knowledge of material characteristics and scene parameters, other than sensor altitude and view angle, are unknown. This is done by leveraging the scene's range dependence to aid in the AC rather than being hindered by it. Instead of allowing the oblique geometry to corrupt the algorithms such that changes in geometry is mistaken for changes in atmospheric state, techniques developed in this paper incorporate the changing geometry to better determine the atmospheric state. Rather than segmenting the image, as suggested by [38], which ignores the physics tying together the different parts of the image and reduces the data feeding each run of the nadir algorithms, the oblique algorithms developed here utilize range-dependent transmission and path radiance into their physics-based radiative models.

Here, two oblique atmospheric compensation algorithms are developed:

1. **Oblique In-Scene Atmospheric Compensation (OISAC).** OISAC is an oblique adaptation of In-Scene Atmospheric Compensation (ISAC), a common LWIR AC technique that had been previously used in a segmented approach to tackle oblique scenes.[38] OISAC does not require image segmentation and

instead utilizes information from the entire image as well as physics-based relations between different parts of the image to better compensation oblique imagery. Based on an adaptation of the scaling procedure of ISAC, OISAC fits a polynomial-based surface to obtain more accurate estimates of the transmission and path radiance line contributions. By incorporating the range dependence of these atmospheric features, these parameters are more accurately estimated for use in identification of the atmospheric state.

2. **Radiance Detrending (RD).** RD is a brand-new technique, based on finding the atmospheric state which best eliminates range-dependence in the ground-leaving radiance. While this technique assumes the range-dependence of ground-leaving radiance is caused entirely by coupled atmospheric/path length effects (e.g. rather than by range-dependent temperatures within a scene), this technique is able to compensate scenes that are challenging for OISAC (i.e. which requires materials with blackbody-like features near 11.73 μm).

These AC techniques are tested on both synthetic data and hyperspectral imagery, described in Chapter III. Analysis of these datasets suggests that these two novel techniques improve compensation for atmospheric effects, leading to improved emissivity and temperature retrieval.

From this research, there are now two separate techniques for performing oblique LWIR atmospheric compensation, a better understanding of the benefits and limitations of these techniques, and an initial evaluation of atmospheric compensation's general capability for handling oblique imaging scenarios. Additionally, by exploring the physics of this new and relevant viewing scenario and demonstrating techniques for developing oblique AC algorithms, this research hints how additional techniques may be adapted or developed.

1.4 Document Outline

First, the theory, mathematical framework, and background literature will be presented to give a context for the oblique LWIR AC techniques developed in this present work. This chapter covers the physics and phenomenology underlying measured radiance in the LWIR along with techniques to compensate for atmospheric effects and retrieve material emissivities from LWIR hyperspectral imagery. Additionally, the scientific body of literature concerning oblique atmospheric compensation will be reviewed, and the shortcomings in current approaches will be highlighted.

The third and fourth chapters detail the two techniques developed to overcome these shortcomings and improve oblique LWIR atmospheric compensation. Specifically, the third chapter discusses OISAC, an oblique adaptation and improvement of the standard ISAC technique. The fourth chapter summarizes the RD technique, a brand-new algorithm which shows promise for compensating oblique scenarios, particularly for scenarios more challenging for ISAC-based approaches.

A brief summary of the work will be given in the final chapter.

II. Background and Theory

Here the theoretical foundations and context of the oblique LWIR AC techniques developed in this present work will be introduced. It begins with an explanation of the LWIR model of sensed radiance model and atmospheric modeling. Next, various LWIR AC techniques are described, highlighting those used in this research for a baseline comparison. After a review of the current oblique AC literature and discussion of shortcomings, the chapter ends with a brief description of emissivity retrieval and additional performance metrics used in this study.

2.1 LWIR Model for Sensed Radiance

Techniques presented in this paper will focus on the LWIR region of the electromagnetic spectrum, an emission-dominated region extending from approximately 8-12 micrometers. The LWIR region contrasts with the shorter wavelength reflection-dominated region, where signatures are dominated by the reflection and scattering of radiation from objects considerably warmer than typical ground temperatures (e.g. the Sun).[21] The ground-leaving radiance in the LWIR, assuming a flat solid facet, is a summation of emitted radiance

$$L_e(\lambda) = B(\lambda, T)\left[1 - \int_0^{2\pi}\int_0^{\pi/2} \rho_{BRDF}(\theta_r, \phi_r, \theta, \phi, \lambda)\cos\theta\sin\theta d\theta d\phi\right], \tag{1}$$

and reflected radiance

$$L_r(\lambda) = \int_0^{2\pi}\int_0^{\pi/2} \rho_{BRDF}(\theta_r, \phi_r, \theta, \phi, \lambda) L_d(\theta, \phi, \lambda)\cos\theta\sin\theta d\theta d\phi, \tag{2}$$

where ρ_{BRDF} refers to the bi-directional reflectance distribution function (BRDF), (θ_r, ϕ_r) refers to the direction of the sensor and (θ, ϕ) refers to the facet coordinates.

The downwelling radiance, $L_d(\lambda)$, quantifies illumination that is incident on the facet, often referred to as the optical background.[42] Potential sources for downwelling radiation include the sky (water vapor, clouds), trees, vehicles, buildings, and other nearby objects. In this research, it is assumed that the earth is locally flat and that downwelling radiance is entirely due to skyshine, i.e. there are no adjacency effects from nearby objects.[10] The quantities in Eqs. 1 and 2 and are spectral in nature and have a wavelength dependence, λ, including the Planck radiation function

$$B(\lambda, T) = \frac{2hc^2}{\lambda^5}\Big[\exp\big(\frac{hc}{\lambda kT}\big) - 1\Big]^{-1}, \tag{3}$$

which describes how all objects of non-zero temperature emit radiation.

Employing the Beard-Maxwell BRDF model, the BRDF may be split into

$$\rho_{BRDF}(\theta_r, \phi_r, \theta, \phi, \lambda) = \rho_s(\theta_r, \phi_r, \theta, \phi, \lambda) + \rho_d(\lambda) + \frac{\rho_v(\lambda)}{\cos\theta + \cos\theta_r}, \tag{4}$$

with specular, diffuse, and volumetric scattering components respectively. Given the complexity (in terms of amount of data and number of free variables) of the BRDF and that the reflectance properties of relatively few materials have been fully characterized, most BRDFs are semi-empirical, and parameters of a first-principles model are fit to measured data.[12] For the purposes of this study, the facet was approximated as a diffuse Lambertian reflector such that $\rho_s = 0$, $\rho_v = 0$, and $\rho_d(\lambda) = \frac{\rho_{HDR}(\lambda)}{\pi}$, where the hemispherical directional reflectance (HDR) describes the reflected irradiance into the direction (θ_r, ϕ_r) from perfectly diffuse illumination and is related to the BRDF via

$$\rho_{HDR}(\theta_r, \phi_r, \lambda) = \int_0^{2\pi}\int_0^{\pi/2} \rho_{BRDF}(\theta_r, \phi_r, \theta, \phi, \lambda)\cos\theta\sin\theta d\theta d\phi, \tag{5}$$

where this angular dependence in the HDR does not exist for the Lambertian surfaces considered in this study.[39] The relative magnitude of the diffuse piece depends on surface roughness or how light penetrates the surface-air interface and scatters inside a object before re-emerging into the air.[47] The model used here will also ignore polarization.

With these assumptions, emissions in Eq. 1 are simplified to

$$L_e(\lambda) = [1 - \rho_{HDR}]B(\lambda, T). \tag{6}$$

Furthermore, the simplifying assumption that the downwelling radiance has no angular dependence is made, giving

$$\int_0^{2\pi} \int_0^{\pi/2} L_d(\theta, \phi, \lambda) \cos\theta \sin\theta d\theta d\phi = \pi L_d(\lambda), \tag{7}$$

which results in

$$L_r(\lambda) = \rho_{HDR}(\lambda) L_d(\lambda). \tag{8}$$

This downwelling radiance will represent the total integrated sky radiance, driven by radiative transfer equations, and adjacency effects from nearby objects will be ignored.[9] Later in 4.3, some features of non-uniform downwelling radiance will be incorporated.

It will also be assumed that objects are opaque (i.e. zero transmission, $\tau_o(\lambda) = 0$) in the LWIR and at local thermodynamic equilibrium. While materials that are transmissive in the LWIR exist, they are typically not of interest to remote sensing applications.[23] Local thermodynamic equilibrium is required to equate absorption, $a(\lambda)$, and emission, $\varepsilon(\lambda)$, from an object via Kirchoff's law, $a(\lambda) = \varepsilon(\lambda)$. Conservation of energy allows us to relate energy that is transmitted, absorbed, or reflected with the total energy incident on a target, i.e. $\tau_o(\lambda) + a(\lambda) + \rho_{DHR}(\lambda) = 1$. Combining

these expressions, the reflectance may be written in terms of emissivity, $\rho_{DHR}(\lambda) = 1 - \varepsilon(\lambda)$.[28] Like reflectance, emissivity is also a characteristic property of an object and is useful for identification and classification of materials. From this development, the ground-leaving radiance is finally expressed as

$$\begin{aligned} L_g(\lambda) &= L_e(\lambda) + L_r(\lambda) \\ &= \varepsilon(\lambda)B(\lambda, T) + [1 - \varepsilon(\lambda)]L_d(\lambda). \end{aligned} \tag{9}$$

As this ground-leaving radiance travels through the atmosphere to the sensor platform, the atmosphere absorbs a portion of this signal by an amount expressed in terms of the transmission $\tau(\lambda)$. Additionally, the atmospheric path radiates thermal energy, adding an amount $L_p(\lambda)$ to the signal. Thus, the total sensed radiance from a single ground pixel is modeled as

$$L(\lambda) = \tau(\lambda)L_g(\lambda) + L_p(\lambda), \tag{10}$$

where, like the downwelling radiance, these $\tau(\lambda)$ and $L_p(\lambda)$ terms may also be expressed in terms of the radiative transfer equation.

LWIR AC aims to estimate the three atmospheric parameters: transmission $\tau(\lambda)$, path radiance $L_p(\lambda)$, and downwelling radiance $L_d(\lambda)$. The ultimate aim of finding these atmospheric parameters is typically to estimate the properties of the object on the ground, characterized by an emissivity $\varepsilon(\lambda)$ and temperature T. This research uses hyperspectral imagery, and thus the spectral nature of all quantities in Eqs. 9 and 10 are considered. A picture of the various components in this sensed radiance model are captured in Fig. 2.

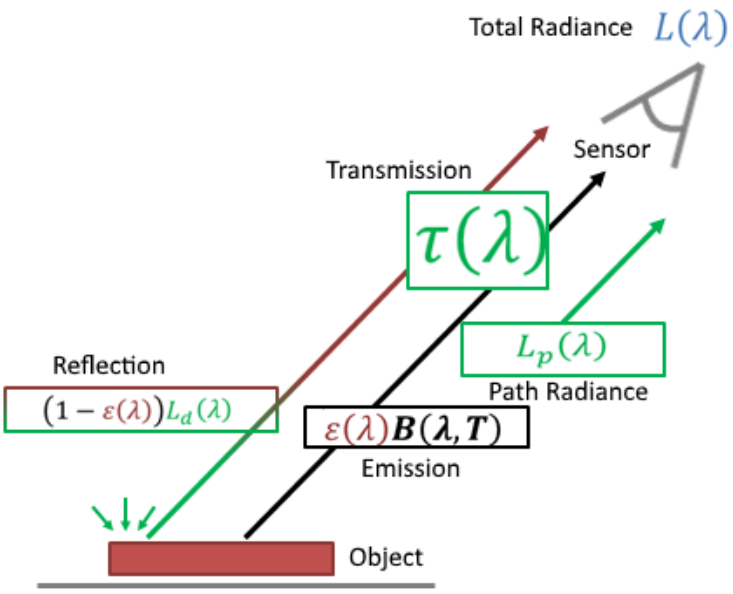

Figure 2. Pictorial representation of the sensed radiance model. Total radiance at the sensor, $L(\lambda)$, is a combination of path radiance contributions, $L_p(\lambda)$, emissions, and reflections.

2.2 Atmospheric Modeling

After introducing and discussing the model for sensed radiance, the three atmospheric components in the sensed radiance model will be described: transmission $\tau(\lambda)$, path radiance $L_p(\lambda)$, and downwelling radiance $L_d(\lambda)$. This begins by relating these terms to the radiative transfer equation. Afterwards, the computational modeling of these quantities will be discussed.

Radiative Transfer Theory.

Radiative transfer theory, as its name suggests, describes how electromagnetic radiation is transported along a particular line-of-sight. For an incremental path length ds, the radiative transfer equation under non-scattering, local thermodynamics

equilibrium conditions is given by

$$\frac{dL}{ds} = -k(s)\Big[L - B\big(T_a(s)\big)\Big], \tag{11}$$

where, as radiance L is transported through the atmospheric path, it is absorbed by the path at a rate determined by the equilibrium absorption coefficient $k(s)$. Meanwhile, blackbody radiance $B\big(T_a(s)\big)$ is emitted by the atmospheric path itself, adding to the total transported radiance. The absorption coefficient depends on the temperature, pressure, and atmospheric composition of the atmospheric path; like the radiance terms, it also contains a wavelength-dependence, λ. Temperature, pressure, and atmospheric composition will vary from point-to-point; thus, both $k(s)$ and $B\big(T_a(s)\big)$ are functions of the position along the path. Also, though not explicitly expressed, all quantities are functions of wavelength, λ.[22]

With a boundary condition specification of initial radiance at position $s = 0$, this differential equation may be solved to yield

$$L(s) = L(0)\exp\Big(-\int_0^s k(s')ds'\Big) + \int_0^s k(s')B\big(T_a(s')\big)\exp\Big(-\int_{s'}^s k(s'')ds''\Big)ds', \tag{12}$$

where the total line-of-sight transmission may readily be expressed as $\tau = \exp\Big(-\int_0^s k(s')ds'\Big)$.[22] When considering radiance leaving an object on the ground and observed by a sensor located at position s, it may be observed that the initial ground-leaving radiance is simply the ground-leaving radiance $L(0) = L_g$, and after properly ascribing the radiance due to emission along the atmospheric path to the path radiance, one may once again arrive at Eq. 10, $L(\lambda) = \tau(\lambda)L_g(\lambda) + L_p(\lambda)$. From this development, it may be observed that a longer atmospheric path will have a smaller transmission and larger path radiance, an observation used frequently throughout this research. For the downwelling radiance incident upon a target from the top of the

atmosphere, there is no initial radiance from space due to its cold background temperature. This just leaves the atmospheric path emission term. Path lengths through the atmosphere to the target from the horizon are longer than those originating from directly overhead, leading to an angle-dependent downwelling radiance. From the integral in Eq. 12, one may see that for this scenario, longer atmospheric paths will lead to larger radiances. As mentioned previously with Eq. 7, it will be assumed this range-dependence is negligible and will instead be using the total integrated sky radiance. Further discussion of angle-dependent downwelling is reserved for discussion in 4.3.

Computational Modeling.

Various atmospheric radiation transport models have been developed to predict atmospheric transmission, path radiance, and downwelling for user-specified viewing and meteorological conditions. One such model is the MODerate resolution atmospheric TRANsmission (MODTRAN) computer code.[5] By designating the location and viewing angle of the sensor along with the temperature, pressure, and humidity profiles of the atmosphere, MODTRAN may calculate a realistic estimate of the LWIR atmospheric contributions to the observed radiance. MODTRAN also has six built-in atmospheric models which each have their own characteristic atmospheric profiles. Model 2 (Mid-Latitude Summer) and Model 6 (U.S. Standard 1976) are commonly used models, corresponding to more humid and more dry atmospheres respectively. These two models will be used extensively for synthetic scene generation in this research.

As an example using the Model 6 atmosphere, one may visualize the relative sizes of the various contributions to the sensed radiance in Eqs. 9 and 10 for a 300 K, $\varepsilon = 0.5$ graybody, by observing Fig. 3. Radiance will be expressed in terms of microflicks,

where $1 \cdot 10^{-6} \frac{\mathrm{W}}{\mathrm{cm}^2 \cdot \mathrm{sr} \cdot \mu\mathrm{m}} = 1\mu-$flick. In this figure, one may see that the surface emission makes up the largest contribution, whereas the reflected and downwelling components are nearly equal. For many natural materials which tend to have larger emissivities, this reflected term may even be smaller than the path radiance for sufficient sensor-scene distances. The dominance of this surface emission term in the LWIR largely arises because surface temperatures are often larger than the effective downwelling temperature (which are inputs to the Planck radiation function).

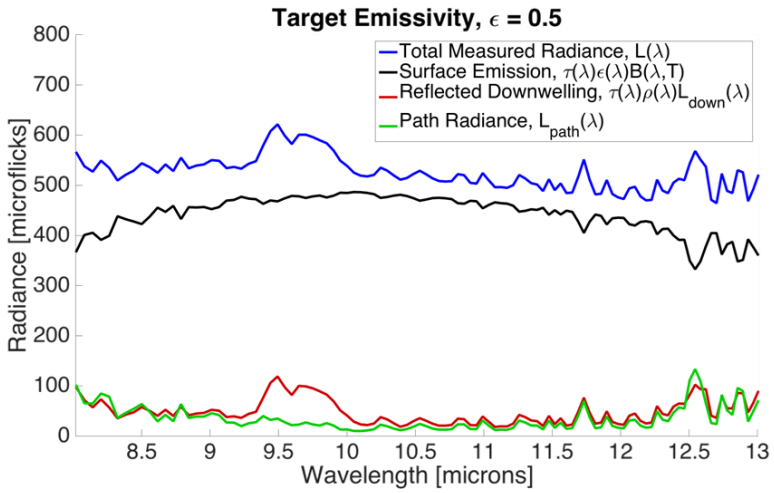

Figure 3. Example of relative contributions to the total sensed radiance for a $\varepsilon = 0.5$ graybody. The summation of the surface emission (black), reflected downwelling (red), and path radiance (green) terms yields the total radiance (blue).

Atmospheric State Approximation.

Rather than define altitude-based profiles for temperature, humidity, pressure and various species concentration (e.g. ozone, carbon dioxide, etc.), one technique used by [46] characterizes an atmospheric state by a single ground air temperature, T_0, and ground water concentration, C_0. From these ground values, an entire temperature/water column is established using a lapse rates similar to the U.S. Standard 1976 atmosphere. Specifically, temperature at a given height h (in km) is modeled as

$$T(h) = \begin{cases} T_0 - 6.49h & h \leq (T_0 - 216.7)/6.49 \\ 216.7 & h > (T_0 - 216.7)/6.49 \end{cases}, \tag{13}$$

while the water concentration is given by

$$C(h) = \begin{cases} C_{std}(h)[1 + (\frac{C_0}{C_{std}(h=0)})(1 - \exp[-0.8(16 - h)])^6] & h \leq 16 \\ C_{std}(h) & h > 16 \end{cases}, \tag{14}$$

where $C_{std}(h)$ is water profile for the U.S. Standard 1976 atmosphere. The pressure profile utilized is the U.S. Standard 1976 pressure profile, and the species concentrations are also assumed to follow the standard model, an assumption which holds reasonably well for low altitude observation (i.e. below 10 km) in high visibility weather conditions.[14]

By analyzing transmission, path radiance, and downwelling radiances for the Model 2 and Model 6 atmospheres, one is able to find their approximate (T_0,C_0) pairs and better understand modeling limitations. Fig. 4 shows a comparison of these three atmospheric quantities for the Model 2 atmosphere and various atmospheric states for a nadir-viewing sensor at 1 km. The top row of the figure shows the mean differences, while the bottom row highlights the maximum differences. The red dots identify the atmospheric state with the best match for the given metric. As a (T_0,C_0) pair is only an approximation for the true atmospheric state, there is no ideal candidate atmosphere that will optimize all six metrics. For this case, (295.25 K, 18300 ppmv) will be identified as the best match. Likewise, looking at Fig. 5 for Model 6, the pair (288 K, 7800 ppmv) will be identified. Neither of these pairs are perfect, particularly for the downwelling component; however, they are still close matches. Additionally, when calculating the metrics in these figures, the spectral region from

9.12-10.2 μm that is typically dominated by ozone was excluded, as the (T_0,C_0) pairs do not include ozone as an input.

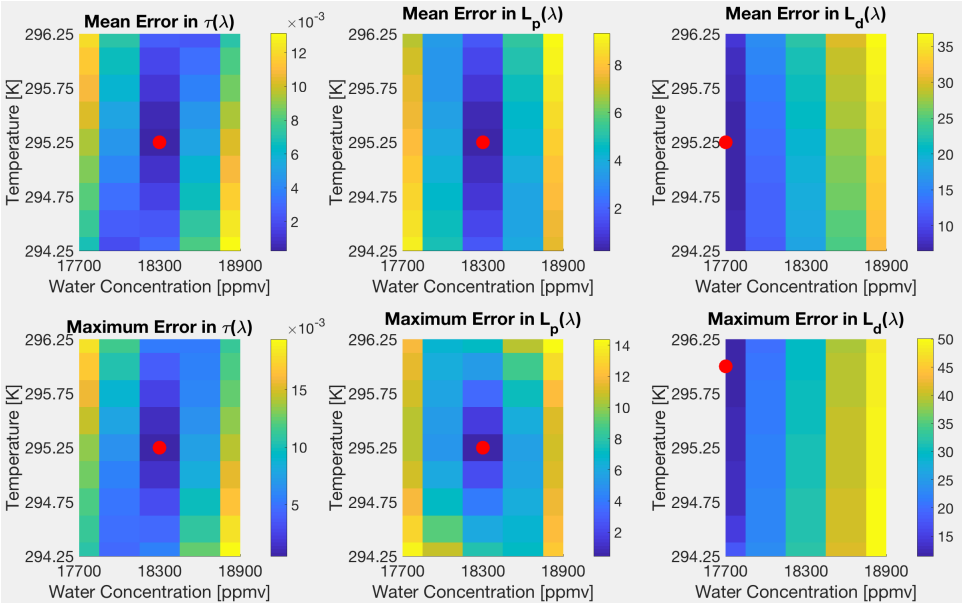

Figure 4. Comparison of transmission, path radiance, and downwelling radiances differences between Model 2 and atmospheric states defined by (T_0,C_0). Radiances are in microflicks.

In Fig. 6, one may see the temperature and water profiles for these four atmospheric states. Since the profiles assumed are based off the Model 6 atmosphere (though not directly matching it), it may be noted that the temperature and water profiles between the Model 6 and (288 K, 7800 ppmv) closely match. The spectral differences in transmission, path radiance, and downwelling radiance between these two atmospheric models is shown in Fig. 7, where the relatively large errors in the aforementioned ozone band may be highlighted. Likewise, results for the Model 2 atmosphere are shown in Fig. 8. Interesting to note is that the Model 2 atmosphere has a noticeably distinct temperature and water profile than the (295.5 K, 18300 ppmv) state, yet its mean/maximum deviations in the atmospheric parameters are comparable to the Model 6 atmosphere and its (T_0,C_0) pair. Mean and maximum spectral errors are shown in Table 1, where one may notice that path radiance error

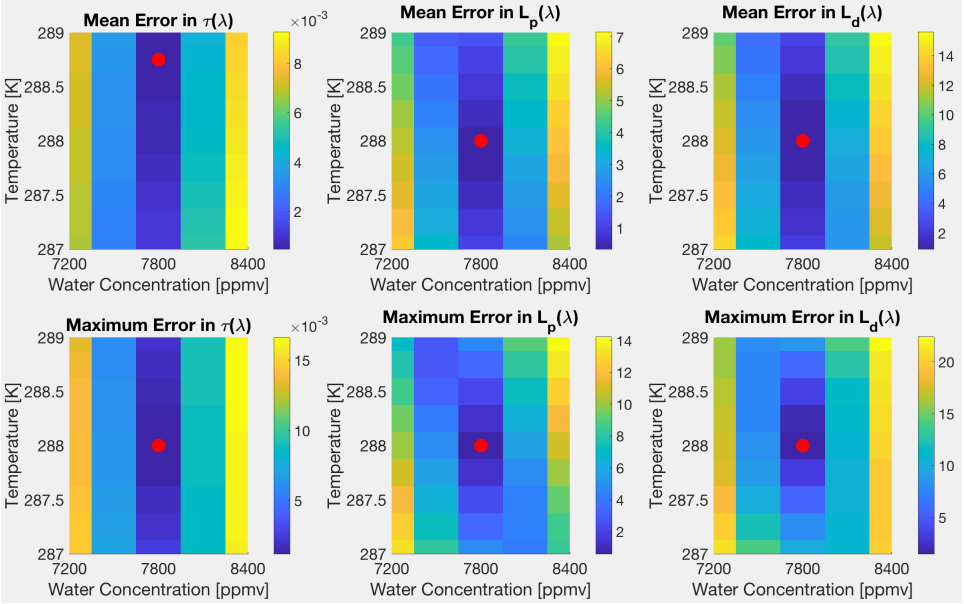

Figure 5. Comparison of transmission, path radiance, and downwelling radiances differences between Model 6 and atmospheric states defined by (T_0,C_0). Radiances are in microflicks.

is on the same order as the 1 microflick of at-sensor noise that will be modeled in 3.4. One may also see that downwelling radiance has a sizable error to it; thus, when retrieving emissivities for highly reflective materials (e.g. aluminum), more sizable errors are expected.

	Model 2 & (295.25, 18300)		Model 6 & (288, 7800)	
	Mean	Max	Mean	Max
Transmission, $\tau(\lambda)$ [unitless]	$2.50 \cdot 10^{-4}$	$5.43 \cdot 10^{-4}$	$9.03 \cdot 10^{-4}$	$3.76 \cdot 10^{-3}$
Path Radiance, $L_p(\lambda)$ [microflicks]	0.217	0.465	0.500	2.69
Downwelling Radiance, $L_d(\lambda)$ [microflicks]	17.2	31.0	2.02	18.3

Table 1. Mean and maximum spectral differences for atmospheric transmission, path radiance, and downwelling radiance between MODTRAN standard model atmospheres and nearly equivalent (T_0,C_0) pairs.

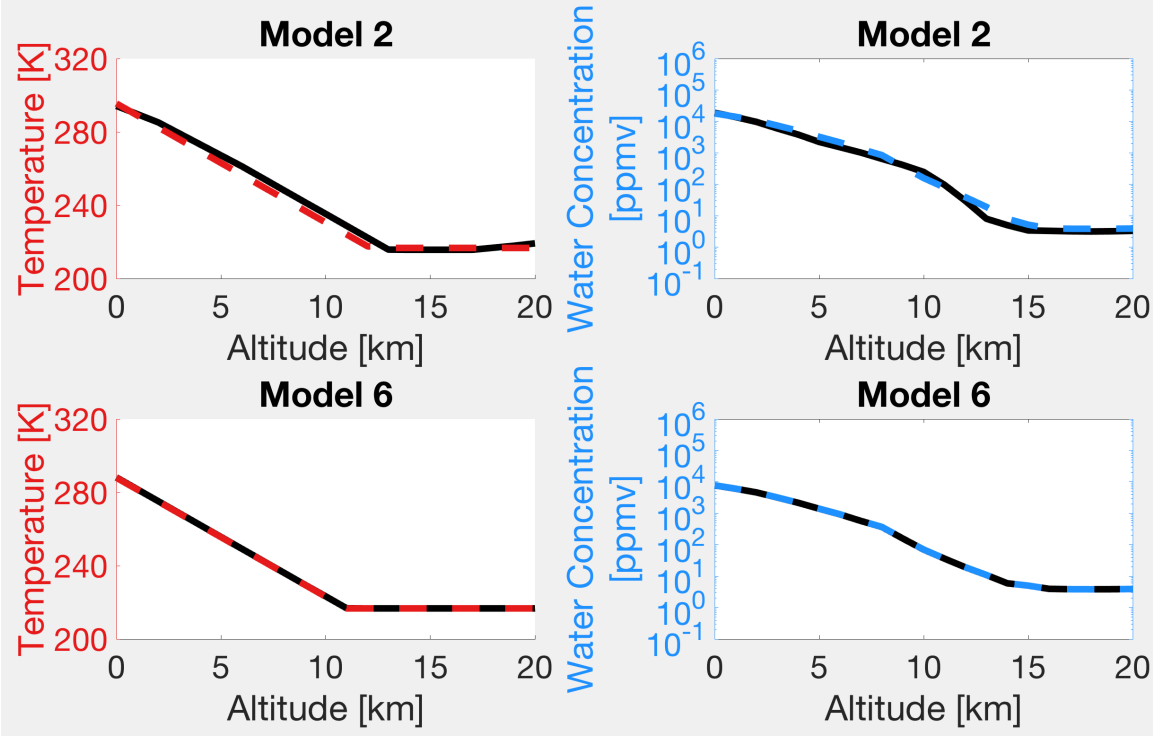

Figure 6. Comparison of temperature and water concentration lapse rates for Model 2, Model 6, and an atmospheric state defined by (T_0,C_0). Solid black lines represent the profiles from the standard MODTRAN models, while the dashed lines represent the profiles generated via Eq. 13 and Eq. 14 for the (T_0,C_0) atmosphere.

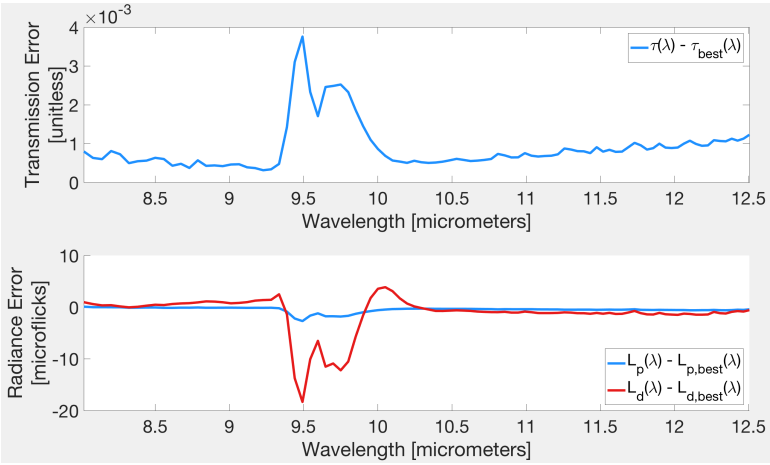

Figure 7. Spectral differences between transmission, path radiance, and downwelling radiance and truth for the Model 6 atmosphere and best (288 K, 7800 ppmv) pair.

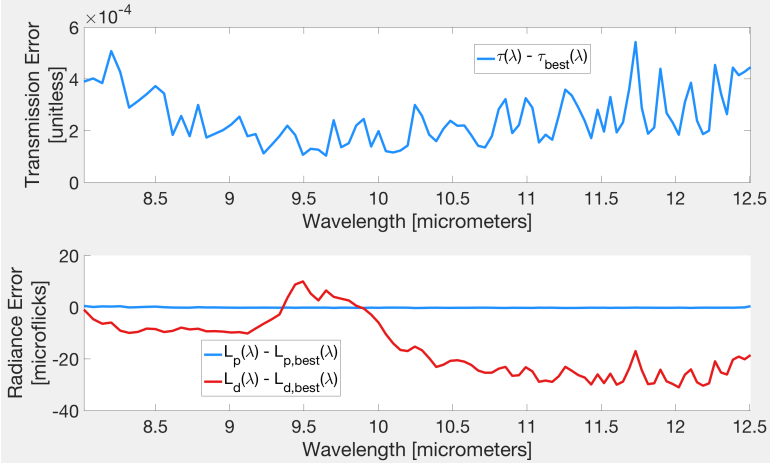

Figure 8. Spectral differences between transmission, path radiance, and downwelling radiance and truth for the Model 6 atmosphere and best (295.25 K, 18300 ppmv) pair.

2.3 Atmospheric Compensation

Numerous atmospheric compensation (AC) techniques have been developed to extract the spectral properties of objects within hyperspectral imagery. These algorithms are roughly divided among model-based and data-only techniques. Model-based techniques often use radiative transfer tools (e.g., MODTRAN, [5]) to estimate atmospheric terms for correction of the data. These techniques require knowledge of atmospheric properties, such as water content and temperature. Data-only techniques estimate atmospheric properties based entirely on data from within the image, often by assuming the scene contains materials with certain spectral characteristics [9]. Many of the AC techniques discussed here are a blend of both model-based and data-only techniques.

There are various AC techniques, all of which aim to estimate the atmospheric contributions to the sensed radiance (i.e. $\tau(\lambda)$, $L_p(\lambda)$, and $L_d(\lambda)$ for the LWIR). Since the sensed radiance model is different for the distinct wavelength regimes (e.g. shortwave infrared vs. LWIR), these nature of these techniques are often unique to their wavelength regime.

In the shortwave infrared (SWIR), the empirical line method (ELM) is a common technique which uses known reflectance spectra to determine atmospheric characteristics. A second SWIR technique, vegetation normalization, is an extension of ELM that instead uses vegetation in a scene to compensate for the atmosphere. Both of these techniques require precise material identification in order to compensate for the atmosphere. Quick Atmospheric Compensation (QUAC) is yet another SWIR technique; however, it does not have this requirement. Instead, QUAC uses the spectral variation in the standard deviation of diverse material spectra throughout the scene to characterize atmospheric illumination and transmission [9].

In the LWIR, two common AC techniques are In-Scene Atmospheric Compensation (ISAC) and Fast Line-of-sight Atmospheric Analysis of Spectral Hypercubes - InfraRed (FLAASH-IR), both of which will be described more in-depth here. This paper focuses on adapting ISAC for the oblique scenario; however, FLAASH-IR will be used to compare results since it is a fairly robust technique that is also widely used. Autonomous Atmospheric Compensation (AAC) will also be described since it bears a strong resemblance to ISAC. Other techniques exist (e.g. QUAC-IR, TEAS, OLSTER) but are not readily available for comparison.

ISAC.

ISAC, or blackbody normalization, is a data-driven technique which relies on the existence of near blackbodies (i.e. $\varepsilon \approx 1$) in a scene [46]. For blackbody pixels, the LWIR model for sensed radiance from Eq. 10 is reduced to a linear equation

$$L(\lambda) = \tau(\lambda)B(\lambda, T) + L_p(\lambda). \tag{15}$$

With an estimation of pixel temperatures, one may create a scatterplot of sensed radiance against Planck blackbody radiance (see Fig. 9) for the blackbody candidate

pixels. The more blackbody-like a pixel is, the more it will be towards the top edge of the scatterplot, given the underlying assumption that the effective atmospheric temperature is cooler than the scene temperature. A line is fit to the upper points of the scatterplot (e.g. by iteratively fitting a line through the data and trimming points below the fit), where the slope and intercept are related to transmission and path radiance respectively by Eq. 15, assuming the fit points are ideal blackbodies. This process is done spectrally.

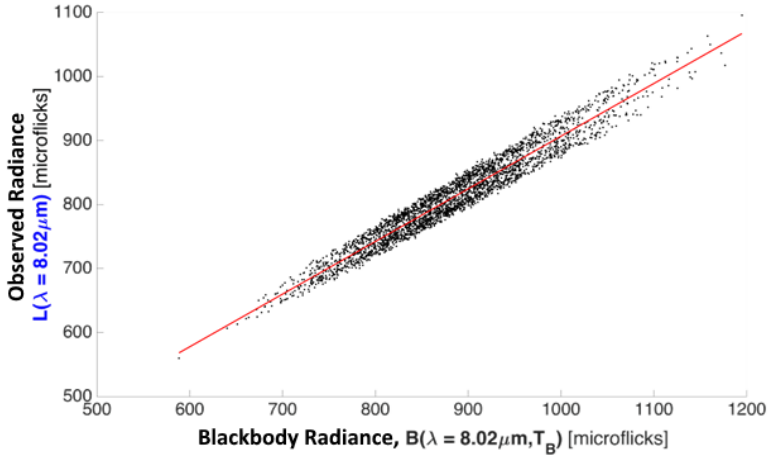

Figure 9. Scatterplot of observed radiance vs. blackbody radiance for the 8.02 μm spectral channel used in the ISAC procedure. Scene pixels are in black, and the best fit line through the points is shown in red.

Before creating this scatterplot, pixel temperatures need to be estimated and blackbody candidates needs to be identified. One common technique involves inverting Eq. 3 to solve for the spectral brightness temperature

$$T_B(L,\lambda) = \frac{hc}{kT \ln\left[\frac{2hc^2}{\lambda^5 L(\lambda)} + 1\right]} \tag{16}$$

in the "most hits channel", $\lambda = \lambda_m$. The most hits channel is found by first finding the wavelength band corresponding to the max spectral brightness temperature for each pixel in the scene, then by generating a histogram of these max temperature bands,

and finally by identifying the wavelength band that occurs most often. An example histogram is shown in Fig. 10. After λ_m is identified, the blackbody candidates are identified as those pixels whose maximum temperature occurred in the most hits channel. This somewhat heuristic method tends to select the most blackbody-like pixels, assuming these materials make up a significant portion of the scene and exhibit a nearly constant emissivity across the spectral range of the sensor. [9][46]

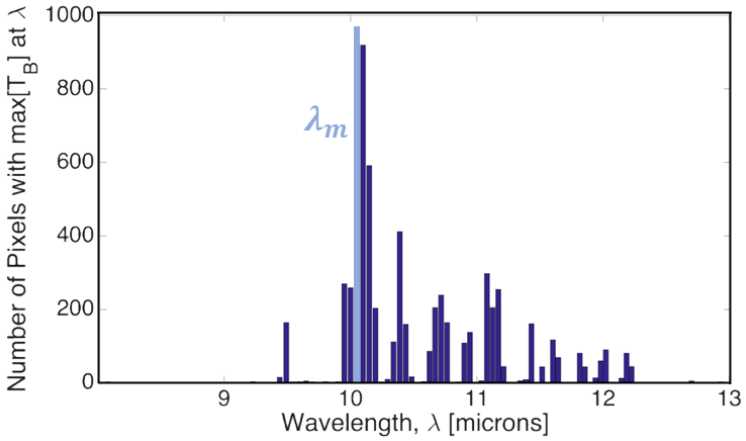

Figure 10. Histogram showing the wavelength channels where pixels had their maximum temperatures. The max hits channel, λ_m is shown in light blue.

Since temperatures for the pixels are unknown and can only be estimated, the resulting transmission and path radiance need to be scaled by estimating atmospheric conditions. One of the scaling techniques discussed in [46] uses the 11.73 micrometer water band feature to estimate the atmospheric state (i.e. water concentration and temperature on the ground, assuming a U.S. Standard 1976 lapse rate). This procedure relies on separating slowly varying continuum effects from quickly varying line effects. Scene estimations of the band's average line contributions of the transmission and path radiance, $\bar{\tau}_\ell$ and $\bar{L}_{p,\ell}$ respectively, are compared with a MODTRAN-generated table of line contributions for various temperatures and water concentrations; the atmosphere which matches these two quantities best is selected. With an atmospheric state selected, the transmission and path radiance estimated earlier in

ISAC are scaled using the transmission and path radiance of the selected atmosphere. The authors refer to this full process with the scaling as the "Full ISAC."

The scaling procedure of the "Full ISAC" was modified slightly to make the process more straight-forward. Rather than use the net radiance depression as [46] had done, their equation C3 was re-expressed using C2 and C6 to yield

$$\bar{L} = \bar{\tau}_\ell \bar{L}_0 + \bar{L}_{p,\ell} \tag{17}$$

where $\bar{L}$ is the band's average radiance and $\bar{L}_0$ is the band's average continuum contribution of the path radiance. Using this expression rather than equation C7 in [46] is simpler, not requiring trapezoidal integration nor additional steps to solve for the variables of interest. To estimate the line contributions to the transmission and path radiance, a scatterplot is created of $\bar{L}$ vs. $\bar{L}_0$ using the blackbody candidates identified earlier. A line is fit to the bottom points, which correspond to the most blackbody-like pixels, and the slope and intercept correspond $\bar{\tau}_\ell$ and $\bar{L}_{p,\ell}$ from Eq. 17.

Autonomous Atmospheric Compensation.

AAC is very similar to the second half of ISAC (i.e. selecting the scaling atmosphere). This technique also relies on use of the 11.73 micrometer water band, but instead of using the selected atmospheric state to scale an original estimate, it simply models the selected atmosphere in MODTRAN and uses MODTRAN's estimates for transmission, path radiance, and downwelling (a process, which may be seen later, that OISAC also uses). Thus, this technique is more model-based as opposed the data-driven nature of ISAC. Benefits and limitations of a model vs. data-driven nature will be discussed in III.

From (7) in [14], AAC hinges on use of a linear regression model, $L_s = Tr \bullet L_W + P_d$. Upon inspection, the form of Eq. 17 is nearly equivalent, where $\bar{L}$ corresponds to the

radiance in the strong absorption channel, L_s, and $\bar{L}_{p,\ell}$ to the radiance in the weak absorption channel, L_W. The main difference between this aspect of ISAC and AAC is that ISAC uses band-averaged quantities rather than measurements at two distinct channels and that ISAC screens out low-emissivity features. These ISAC features are favorable and have led to greater accuracy and stability when testing on synthetic scenes.

FLAASH-IR.

FLAASH-IR is based on the observation that atmospheric spectral features tend to be sharper than material spectral features. These spectral differences between solids and gases arise as a result from differences in lifetimes of excited states. Excited states in solids tend to have shorter lifetimes because the energy can be quickly dissipated to connected molecules, whereas the isolated nature of gases does not allow them to de-excite as quickly [7].

Using this knowledge, FLAASH-IR attempts to minimize the amount of sharp, atmospheric features in its retrieved emissivities and find the smoothest retrieved emissivity. Emissivity is calculated by solving Eqs. 10 and 9 for a plethora of different object temperatures and atmospheric states using a MODTRAN-generated look-up table. Looking at diverse pixels throughout the scene, FLAASH-IR maximizes emissivity spectral smoothness for all these diverse classes by picking the optimal set of atmospheric state and pixel temperatures [1]. The metric used to quantify smoothness will be described in 2.6.

2.4 Oblique Atmospheric Compensation

Oblique Atmospheric Compensation is a relatively new field of study, and as a result, there are relatively few datasets available, a handful of journal articles written

about it, and only minor adjustments to modify existing techniques. Presented here will be a discussion of how techniques have been used in the literature to account for oblique viewing geometries. While the research in this study is most related to the first of the following three areas, these other areas of oblique AC research are included for completeness.

Data-Driven Techniques.

The sole effort in data-only oblique LWIR AC known to the authors is [38]. Here, an oblique Telops Hyper-Cam scene taken from Death Valley, CA was analyzed by applying the partial (i.e. unscaled) ISAC to ten equally-sized horizontal strips. While path range variation for the entire scene was between 20 m and 50 km, this process of image segmentation drastically reduced the range variation within a single sub-image. The authors needed to carefully consider the number of strips to segment the scene into, balancing between having large enough strips with a sufficient number of pixels for ISAC versus having small enough strips such that the atmosphere could be assumed homogeneous within each strip. They noted that this assumption of homogeneity within each strip might not hold well for conditions more humid than this desert scene that they tested; however, even for their relatively dry conditions, they believe the 50 km segment hinted at levels of atmospheric constituents significantly different than at other ranges.

Altogether, their analysis showed success at retrieving quartz emissivity spectra for dry conditions via image segmentation. For future work, they recommended incorporating downwelling radiance for scenes without adequate blackbody populations as well as automating the segmentation approach. They had supervised the precise number of segments to divide the scene into in order to balance the previous two considerations; however, this optimal number of strips is expected to change based

on viewing geometry parameters and atmospheric humidity.

Model-Based Techniques.

One model-based technique which has been adapted to account for multiple viewing geometries is the Airborne Atmospheric and Topographic Correction Model (ATCOR). In order to perform LWIR AC, this technique relies heavily on co-registered bands in the SWIR. ATCOR uses these bands to estimate the water vapor profile and visibility, which are then be used by MODTRAN to model the LWIR. Next, it uses the SWIR to separate ground pixels into one of three different emissivity classes (either asphalt, vegetation, or water/miscellaneous), each of which are assigned a single, non-spectral emissivity. Finally, this technique inverts the Planck blackbody function to get pixel temperatures. The latest version of ATCOR has been updated to take terrain shape from a digital elevation model into account, as well as multiple viewing geometries for the different pixels throughout the scene [33]. While ATCOR has been modified to account for oblique geometries, this technique is of a very different nature. It requires use of SWIR data, ignores the spectral nature of materials' emissivity, and only classifies rather than retrieves these emissivities.

A second study using model-based AC studied the impact of not incorporating the variable path lengths in an oblique scene. Reference [24] studied surface brightness temperature retrieval from oblique, single-channel LWIR imagery in urban environments. Using atmospheric profile data from in-situ meteorological measurements, they simulated atmospheric effects with MODTRAN, incorporating either a single, median line-of-sight geometry or multiple lines-of-sight throughout the scene. They determined that the atmospheric differences across an oblique scene were significant. Not accounting for the path length variations led to errors of up to 3.7 K during the day and 0.5 K during the night, sizable differences for the study of energy ex-

change at the surface-atmosphere interface [40, 43] and temperature variability within urban/natural habitats [20].

Oblique SWIR AC.

Other research has explored oblique AC from different perspectives. [2] studied the impacts of using nadir techniques on oblique data. They employed SWIR AC techniques to analyze EO-1 Hyperion data collected with an off-nadir angle of 63 degrees, showing that very long atmospheric paths would not preclude them from obtaining reasonably accurate reflectance spectra given favorable weather conditions. In a separate study, [6] made modifications to the ELM to compensate for oblique SWIR synthetic imagery, requiring known reflectances in the scene. Since these two studies focus entirely on the SWIR spectrum, neither are truly related to the present work.

2.5 Shortcomings of Current Oblique AC

Current data-only AC techniques are hindered by scenes with oblique geometry, having to balance between violating algorithm assumptions and reduction of usable data. The application of these techniques on oblique scenes has typically involved running standard nadir-derived AC techniques on the either the entire image [2] or independently on segments of the image [38]. If one runs the technique on the entire image, then the assumption that every pixel is experiencing the same atmospheric effects is violated. Alternatively, while image segmentation results in sub-scenes with the near uniform path range characteristic of nadir scenes, cutting the image into parts reduces the usable data for each AC application. Below is a summary of some of the challenges facing current oblique AC.

Challenges of Analyzing Whole Scenes.

As mentioned, nadir-derived AC algorithms currently used to analyze entire oblique scenes without segmentation face numerous challenges. The assumption that every pixel experiences the same atmospheric effects no longer holds. Violation of this assumption biases current techniques and degrades their performance. While one might expect these nadir techniques to effectively compensate for the middle of the image, from empirical observations of both ISAC and FLAASH-IR, these techniques seem to be biased towards compensating for closer ranges. Exploring why this might be the case for ISAC, a synthetic scene of mean temperature 300 ± 5 K blackbodies was generated in a Model 6 atmosphere. While fitting to the top of the L vs. B curve as in Fig. 9, it was noticed that pixels near the bottom of the scene were favored. This is highlighted in Fig. 11. While fitting to the top of the scatterplot ordinarily corresponds to fitting to the most blackbody-like pixels, since blackbodies at closer ranges appear brighter, those pixels with less atmospheric attenuation are favored. Thus, for even this scene made of entirely blackbody pixels, ISAC is biased when analyzing scenes containing oblique geometry.

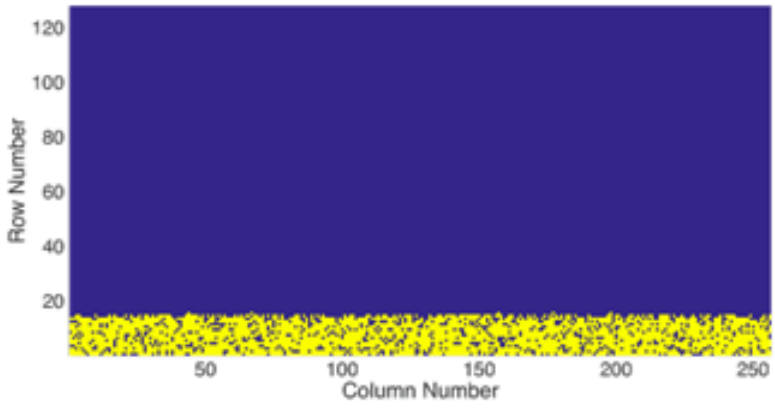

Figure 11. Locations within the image for those pixels selected (yellow) to be near the top of the ISAC scatterplot at 8 micrometers, for a noiseless scene of blackbodies at 300±5 K in a Model 6 atmosphere. Selected pixels dominated the bottom of the image, at low row numbers.

Additionally, since these nadir-derived techniques lack the flexibility to permit transmission and path radiance variation across the scene, these techniques may confuse the variable atmospheric effects with variations in object temperature. Some applications require realistic temperature estimates (e.g. when modeling and predicting climate change), so using temperature to pseudo-compensate for changing atmospheric effects is not ideal [14]. To better understand this impact, two blackbody objects at 300 K were forward-modeled through the same Model 2 atmosphere but at different ranges. Inverting measured radiance into a spectral brightness temperature, one may see in Fig. 12 that the two objects have different apparent spectral temperatures. While these targets are reflecting and emitting the exact same amount of radiation, the closer target will appear hotter. This predicted artifact will be seen later in Fig. 28.

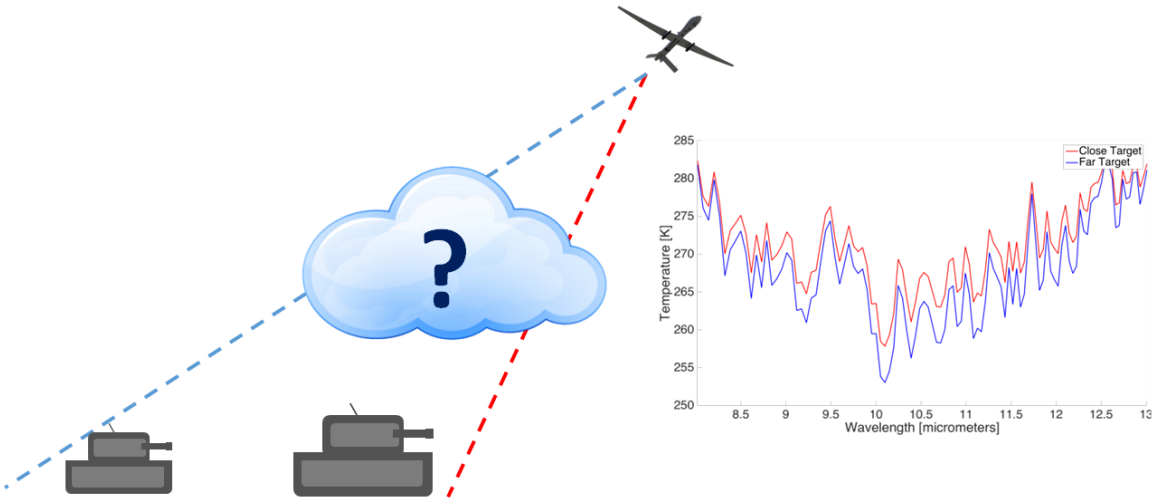

Figure 12. Spectral brightness temperature comparison for two blackbodies in a Model 2 atmosphere. Material properties for both objects are identical (i.e. $\varepsilon = 1$, $T = 300$ K); however, they are located at different ranges from the sensor. The further blackbody at the further range (blue) has a smaller spectral brightness temperature than the blackbody at the closer range (red).

Challenges of Analyzing Segmented Scenes.

By segmenting the scene prior to analyzing, the biases and artifacts from inflexibility in varying the atmospheric state are reduced, but other problems are introduced. First, this process is a more manual/supervised approach. One comment in [38] was the suggestion that future work should aim to automate the segmentation process, carefully selecting the number of segments to balance between having enough data for successful AC but small enough so that there is little atmospheric variation within each segment.

A second concern is that image segmentation introduces its own inconsistencies. Applying the ISAC approach to ten different segments of both synthetic and hyperspectral imagery, it was found that this approach suggested different atmospheric states for the different segments of the image. Characterizing atmospheric states by a ground air temperature and water concentration, (T_0,C_0), Fig. 13 shows the results of segmenting one such scene. One may observe a variation of more than a 10 percent in temperature and 20 percent in water concentration for the different image segments.

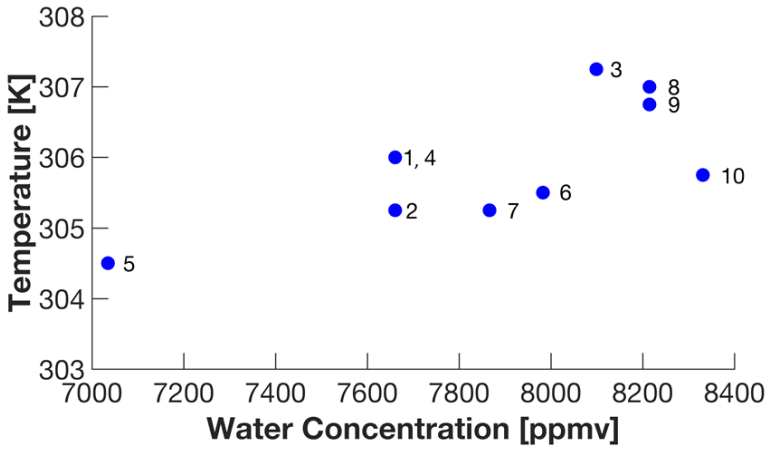

Figure 13. Atmospheric states (T_0,C_0) selected from the Segmented ISAC approach on the Mako scene (described in 3.4) are shown in blue. The corresponding segment numbers are shown to the right of the selected states.

While these ten atmospheric states are somewhat similar, effects of selecting even slightly different atmospheric states may be seen. By performing k-means clustering (described in 2.8) over the same scene used to generate Fig. 13, one may see evident image segmentation artifacts, especially near image segmentation boundaries. This is demonstrated in Fig. 14. The leftmost subimage is a picture of the entire scene, where each color is a distinct pixel class; these 14 different material class are individually identified in yellow to the right. In these individual classes, sharp horizontal lines as well as parts material classes that only span 1/10th of the total number of rows may be seen (the image was divided into ten parts prior to AC). The segment from from about row 1100 to 1300 especially stands out, suggesting that this segment of the total image might have had significantly different AC result. These artifacts are due to image segmentation, demonstrating one of its limitations.

2.6 Temperature-Emissivity Separation

After AC in the LWIR, one may solve for the ground radiance in Eq. 10 to get

$$L_g(\lambda) = \frac{L(\lambda) - L_p(\lambda)}{\tau(\lambda)}, \tag{18}$$

and then solve Eq. 9 for emissivity to get

$$\varepsilon(\lambda, T) = \frac{L_g(\lambda) - L_d(\lambda)}{B(\lambda, T) - L_d(\lambda)}. \tag{19}$$

Even with perfect knowledge of the atmospheric state, the emissivity of an individual pixel cannot be determined without knowing the temperature. With K spectral bands there are K knowns and $K + 1$ unknowns, an underdetermined system that requires a detangling of emissivity and temperature. Solving this system is referred to as Temperature-Emissivity Separation (TES).

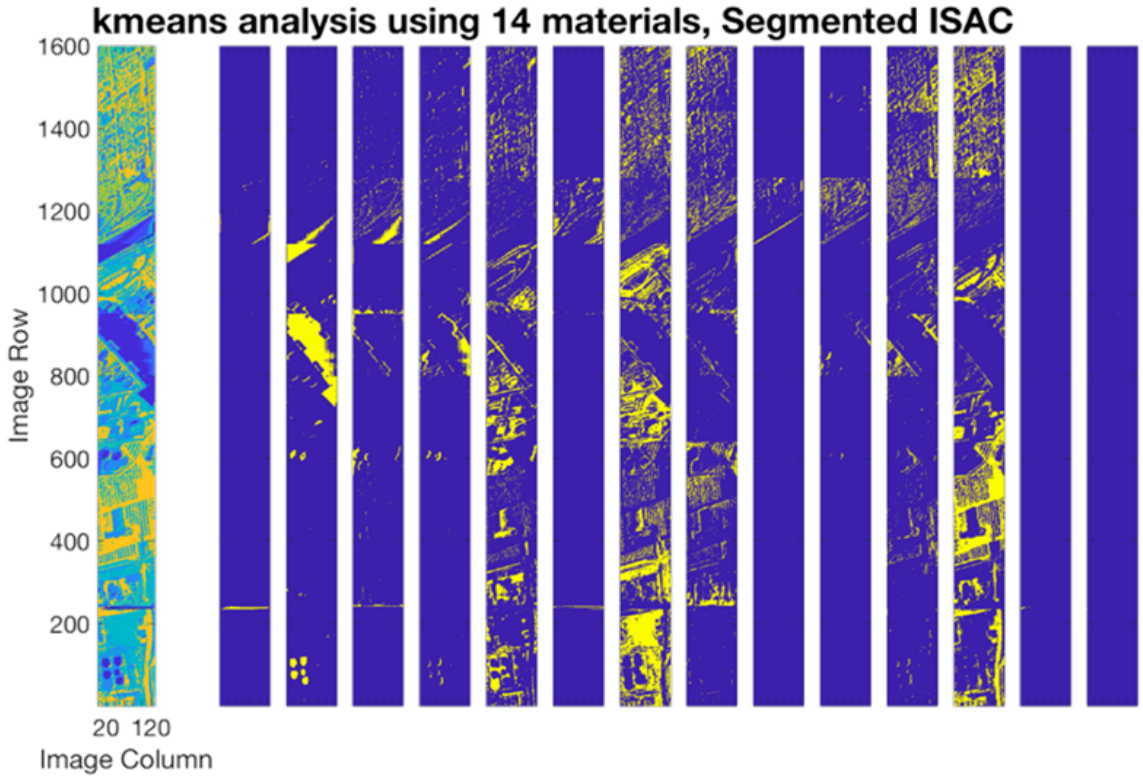

Figure 14. Results of k-means clustering on the retrieved emissivity after performing atmospheric compensation on the Mako scene with the Segmented ISAC approach. The full image is shown left, whereas the 14 different material classes are identified in yellow to the right.

The primary means of performing TES is based on the observation that material emissivities are smoother than atmospheric transmission features, discussed earlier in 2.3. The research presented here incorporates the TES method of FLAASH-IR, i.e. Automatic Retrieval of Temperature and Emissivity using Spectral Smoothness (ARTEMISS) [31].

ARTEMISS performs TES by finding the temperature which minimizes a smoothness metric. One means by which ARTEMISS measures smoothness is via the standard deviation of the difference between the retrieved emissivity from Eq. 19 and its three-point boxcar-average. After calculating the emissivity smoothness for multiple temperatures, the optimal temperature is the one with minimal smoothness [7].

2.7 Retrieved Emissivity

In order to find targets and identify materials, retrieving an emissivity for objects in a scene is especially helpful. This is done by comparing the retrieved emissivity from Eq. 19 with those from a database of different reference target signatures. The nature of this comparison depends on the material of interest and the specific target detection algorithm; however, two metrics form the basis of many signature matched detection algorithms and will be used in this research to gauge performance: spectral correlation and mean root-mean-square (RMS) difference.

The first, the Pearson correlation coefficient, is a metric to estimate how well the spectral shape of the retrieved emissivity and reference emissivity match. The Pearson correlation coefficient may be calculated via

$$r_P = \frac{\sum_{i=1}^{K}(x_i - \bar{x})(y_i - \bar{y})}{(K-1)\sigma_x\sigma_y}, \tag{20}$$

where $\bar{x}$ and $\bar{y}$ are the mean and σ_x and σ_y are the standard deviation of two K-

dimensional vectors. The Pearson correlation coefficient takes on a value between -1 and 1, expressing correlation and anti-correlation respectively. A score of zero would suggest that the retrieved and reference emissivity signatures bear no resemblance to one another. Comparing this metric with a common target detection algorithm, one version of the Spectral Matched Filter follows the form of $r_{SMF} = (\boldsymbol{x}-\hat{\boldsymbol{\mu}})^T\hat{\boldsymbol{\Sigma}}^{-1}(\boldsymbol{y}-\hat{\boldsymbol{\mu}})$, where $\hat{\boldsymbol{\mu}}$ is the background's mean signal and $\hat{\boldsymbol{\Sigma}}$ is the background's covariance matrix. Similar to the Pearson correlation coefficient, this detection algorithm measures similarity of spectral shape between two signals. [9]

Material emissivities without prominent spectral features need to be characterized by a different metric, such as the RMS difference. As a simple example, the spectral emissivity shapes of a blackbody and graybody are identical; however, the two emissivities may have a large contrast in magnitude. This difference is not captured by the Pearson correlation coefficient, and this first metric would identify the blackbody and graybody as the same material. However, this difference in magnitude between the two emissivities may be captured via the RMS difference

$$r_R = \sqrt{\frac{1}{n}\sum_{i=1}^{n}(x_i - y_i)^2}. \tag{21}$$

The closer this RMS difference is to zero, the more similar the two signals are in magnitude.

2.8 K-means Clustering

Another processing technique used extensively in this research is k-means clustering, which separates signals into distinct classes. Class assignment is based on minimizing a distance metric (typically a Euclidean or cosine distance) between the signal and class mean vector, which is taken as the mean of all signals in a class.

This process requires initial class vectors to be chosen (at random or based on *a priori* knowledge) and that the user manually specifies the number of classes. Class assignment is done iteratively until a stopping condition is met. For the purposes of this study, the cosine distance metric was applied because the desire was to match materials based on their spectral shape rather than their RMS difference.

III. Oblique In-Scene Atmospheric Compensation

This chapter was prepared for submission to the journal, IEEE Transactions on Geoscience and Remote Sensing. Daniel O'Keefe was the lead author, while Dr. Nauyoks, Dr. Hawks, Dr. Meola, and Dr. Gross were co-authors and served as reviewers of the article. The prepared article in its complete form is included here, and as a result, minor amounts of repetition are present.

3.1 Introduction

Numerous atmospheric compensation (AC) techniques have been developed to extract the spectral properties of objects within hyperspectral imagery. These algorithms are roughly divided among model-based and data-only techniques. Model-based techniques often use radiative transfer tools (e.g., MODTRAN, [5]) to estimate atmospheric terms for correction of the data. These techniques require knowledge atmospheric properties, such as water content and temperature. Data-only techniques estimate atmospheric properties based entirely on data from within the image, often by assuming the scene contains materials with certain spectral characteristics [9]. Many of the AC techniques discussed here are a blend of both model-based and data-only techniques.

Much of the research in AC has been done for nadir or nearly nadir-viewing geometries. In these scenarios, an overhead sensor captures radiance from a scene and sensor-scene distance for all pixels throughout the scene is nearly the same, assuming no tall structures exist in the imagery (e.g., mountains, skyscrapers, etc.). However, for sensors operating in a whiskbroom configuration sweeping across large angles, these assumptions are generally violated. In oblique scenarios, the sensor-scene distance for the pixels throughout the image can vary greatly, depending on the viewing

angle and altitudes involved. Since atmospheric path radiance and transmission depend heavily on the path length between the sensor and scene, oblique images may have considerable variation of these two atmospheric quantities. Applying nadir AC techniques to oblique images will lead to inaccurate, biased retrievals by ignoring the variability of transmission and path radiance across the image, which can significantly affect target detection.

Oblique AC is a relatively new area of study and limited work has been done to tailor AC algorithms to this new operating scenario. Previous research in oblique AC has mainly been concerned with observing the impact of obliquely collected data on nadir algorithms [2] or segmenting the image before applying nadir techniques [38]. While direct or slightly modified applications of these nadir techniques have shown favorable results for oblique scenarios, only a limited number of atmospheric conditions and ranges have been tested, and the nadir techniques do not capitalize on the additional information present in an obliquely viewed scene.

The aim of this research is to adapt an existing longwave infrared (LWIR) AC technique (i.e. the in-scene atmospheric correction (ISAC) algorithm) to an oblique imaging scenario using a radiative model which accounts for the range dependence. Rather than segmenting the image, which ignores the physics tying together the different parts of the image and reduces the data feeding each run of the nadir algorithm, this oblique adaptation utilizes a range-dependent transmission and path radiance. Directly accounting for the range dependence of these two atmospheric quantities has shown considerable improvement in both atmospheric and emissivity retrieval.

3.2 Background and Theory

Here the theoretical foundations of the LWIR AC technique that is modified in this present work will be introduced. First is an introduction of the model for sensed

radiance in the LWIR. Next, a few LWIR AC techniques for baseline comparison will be introduced, followed by a discussion of current oblique AC. This section concludes with a discussion of the range variation of transmission and path radiance.

LWIR Model for Sensed Radiance.

Techniques presented in this paper will focus on the LWIR region, extending from approximately 8-12 micrometers. Scattering effects are negligible in this region, as contributions are emission-dominated. The sensed radiance from a single ground pixel is modeled as

$$L(\lambda) = \tau(\lambda)L_g(\lambda) + L_p(\lambda) \tag{22}$$

where the ground-leaving radiance is given by

$$L_g(\lambda) = \varepsilon(\lambda)B(\lambda, T) + \big[1 - \varepsilon(\lambda)\big]L_d(\lambda) \tag{23}$$

and the atmospheric quantities are transmission τ, path radiance L_p, and downwelling radiance L_d. LWIR AC aims to estimate these three atmospheric parameters. Properties of the target are given by its emissivity ε and temperature T. All quantities in (22) and (23) are spectral in nature and have a wavelength dependence, λ, including the Planck radiation function

$$B(\lambda, T) = \frac{2hc^2}{\lambda^5}\left[\exp\left(\frac{hc}{\lambda kT}\right) - 1\right]^{-1}. \tag{24}$$

This model assumes materials are ideal diffuse Lambertian reflectors (i.e. negligible specular/volumetric scattering), opaque and at local thermodynamic equilibrium, so that its reflectivity ρ is given by $\rho(\lambda) = 1 - \varepsilon(\lambda)$. Additionally, it is assumed the downwelling radiance represents the total integrated sky radiance and will ignore adjacency effects from nearby objects.

LWIR Atmospheric Compensation.

There are various AC techniques, all of which aim to estimate the atmospheric contributions to the sensed radiance. Since the sensed radiance model is different for different wavelength regimes (e.g. shortwave infrared vs. LWIR), these techniques are different depending on the wavelength of interest. In the LWIR, two common techniques are In-Scene Atmospheric Compensation (ISAC) and Fast Line-of-sight Atmospheric Analysis of Spectral Hypercubes - InfraRed (FLAASH-IR). This paper focuses on adapting ISAC for the oblique scenario; however, FLAASH-IR will be used to compare results since it is another common technique. FLAASH-IR is based on the observation that atmospheric spectral features tend to be sharper than material spectral features [7]. FLAASH-IR identifies the best combination of object temperatures and atmospheric state (from a MODTRAN-generated look-up table) that maximizes emissivity spectral smoothness for diverse pixels in the scene [1].

ISAC, or blackbody normalization, is a technique which relies on the existence of near blackbodies (i.e. $\varepsilon \approx 1$) in a scene [46]. For blackbody pixels, the LWIR model for sensed radiance from (22) is reduced to a linear equation

$$L(\lambda) = \tau(\lambda)B(\lambda, T) + L_p(\lambda). \tag{25}$$

Thus, with an estimation of pixel temperatures (see section 3 in [46] for details), one may create a scatterplot of sensed radiance against Planck blackbody radiance. The more blackbody-like a pixel is, the more it will be towards the top edge of the scatterplot, given the underlying assumption that the effective atmospheric temperature is cooler than the scene temperature. A line is fit to the upper points of the scatterplot (via various techniques discussed in [46]), where the slope and intercept are related to transmission and path radiance respectively by (25). This process is done spectrally.

Since temperatures for the pixels are unknown and can only be estimated, the resulting transmission and path radiance need to be scaled by estimating atmospheric conditions. One of the scaling techniques discussed in [46] utilizes the 11.73 micrometer water band feature to estimate the atmospheric state (i.e. water concentration and temperature on the ground, assuming a U.S. Standard 1976 lapse rate). This procedure relies on separating slowly varying continuum effects from quickly varying line effects. Scene estimations of the band's average line contributions of the transmission and path radiance, $\bar{\tau}_\ell$ and $\bar{L}_{p,\ell}$ respectively, are compared with a MODTRAN-generated table of line contributions for various temperatures and water concentrations; the atmosphere which matches these two quantities best is selected. With an atmospheric state selected, the transmission and path radiance estimated earlier in ISAC are scaled using the transmission and path radiance of the selected atmosphere. The authors refer to this full process with the scaling as the "Full ISAC." Additional details may be found in [46].

The scaling procedure of the "Full ISAC" was slightly modified, to make the process more straight-forward. Rather than utilize the net radiance depression as [46] had done, their equation C3 was re-expressed using C2 and C6 to yield

$$\bar{L} = \bar{\tau}_\ell \bar{L}_0 + \bar{L}_{p,\ell}, \tag{26}$$

where $\bar{L}$ is the band's average radiance and $\bar{L}_0$ is the band's average continuum contribution of the path radiance. This formula may be alternatively derived by considering that the radiance from the continuum, $\bar{L}_0$, is decreased by a factor of $\bar{\tau}_\ell$ due to the water band; the water then also emits an amount $\bar{L}_{p,\ell}$ back into the path, which is then added to $\bar{\tau}_\ell \bar{L}_0$ and immediately results in (26). As in the original derivation, it is assumed that these functions vary slowly enough with λ so that the mean values may be used. Using (26) rather than equation C7 in [46] is simpler,

not requiring trapezoidal integration nor additional steps to solve for the variables of interest. When using this alternate form, the most blackbody-like pixels will instead be at the bottom of the scatterplot.

Upon inspection, the form of (26) is nearly equivalent to the one used in Autonomous Atmospheric Compensation (AAC). Recognizing that $\bar{L}$ corresponds to the radiance in the strong absorption channel and $\bar{L}_{p,\ell}$ to the radiance in the weak absorption channel, one may see a striking similarity with (7) in [14]. The main difference between this aspect of ISAC and AAC is that ISAC uses band-averaged quantities rather than measurements at two distinct channels and that ISAC screens out low-emissivity features. These ISAC features are favorable and have led to greater accuracy and stability when testing on synthetic scenes.

Current Research in Oblique AC.

Current data-only AC techniques are hindered by scenes with oblique geometry, having to balance between violating algorithm assumptions and reduction of usable data. The application of these techniques on oblique scenes has typically involved running standard nadir-derived AC techniques on the either the entire image [2] or independently on segments of the image [38]. If one runs the technique on the entire image, then the assumption that every pixel is experiencing the same atmospheric effects is violated. Alternatively, while image segmentation results in sub-scenes with the near uniform path range characteristic of nadir scenes, cutting the image into parts reduces the usable data for each AC application. Both approaches ignore the additional information given by relations between the different rows of the image.

The technique presented here is different, in that it leverages the scene's range dependence to aid in the AC rather than being hindered by it. Instead of allowing the oblique geometry to corrupt the algorithms such that a change in geometry is

mistaken for a change in atmospheric state, the technique developed here leverages the changing geometry to better determine the atmospheric state.

The sole effort in data-only oblique LWIR AC known to the authors is [38]. In [38] an oblique Telops Hyper-Cam scene taken from Death Valley, CA was analyzed by applying the partial (i.e., unscaled) ISAC to ten equally-sized horizontal strips. While path range variation for the entire scene was between 20 m and 50 km, this process of image segmentation drastically reduced the range variation within a single sub-image. The authors needed to carefully consider the number of strips to segment the scene into, balancing between having large enough strips with a sufficient number of pixels for ISAC versus having small enough strips such that the atmosphere could be assumed homogeneous within each strip. They noted that this assumption of homogeneity within each strip might not hold well for conditions more humid than this desert scene that they tested; however, even for their relatively dry conditions, they believe the 50 km segment hinted at levels of atmospheric constituents significantly different than at other ranges. Altogether, their analysis showed success at retrieving quartz emissivity spectra for dry conditions via image segmentation. For future work, they recommended incorporating downwelling radiance for scenes without adequate blackbody populations as well as automating the segmentation approach. They had supervised the precise number of segments to divide the scene into in order to balance the previous two considerations; however, this optimal number of strips is expected to change based on viewing geometry parameters and atmospheric humidity.

Other research has explored oblique AC from different perspectives using short-wave infrared (SWIR). Reference [2] employed nadir-derived SWIR AC techniques to analyze EO-1 Hyperion data collected with an off-nadir angle of 63 degrees. Reference [6] made modifications to the empirical line method to compensate for SWIR synthetic imagery, requiring known reflectances in the scene. Reference [33] focused

on model-based AC, estimating the state of the atmosphere using SWIR data and then using this estimate together with MODTRAN to model the LWIR. They incorporated variable path lengths, arising from both multiple sensor look angles and elevation changes. Finally, [24] studied surface brightness temperature retrieval from oblique, single-channel LWIR imagery in urban environments. Using atmospheric profile data from in-situ meteorological measurements, they simulated atmospheric effects with MODTRAN, incorporating either a single, median line-of-sight geometry or multiple lines-of-sight throughout the scene. They determined that the atmospheric differences across an oblique scene were significant.

Range Variation of Atmospheric Parameters.

Two of the atmospheric quantities, transmission and path radiance, are dependent upon both sensor-scene distance and atmospheric characteristics (e.g. water concentration and temperature). While this distance is relatively fixed for nadir-viewing geometries, this is not the case for oblique geometries. AC algorithms which ignore the impact of range may confuse its influence with that of atmospheric characteristics. Transmission and path radiance change with range in a monotonic fashion, i.e. as range increases, transmission decreases and path radiance increases. If the rows of the image corresponded to different distances for an oblique scene (a convention used throughout this paper), where the bottom and top of the image represent the closest and furthest distances respectively, then as one were to move up the image (i.e. to a larger row number), a smaller transmission and greater path radiance would be expected.

After exploring a variety of atmospheric states and imaging conditions, it was found that the range dependence for the transmission and path radiance was sufficiently captured using low-order polynomials with respect to row number. Observa-

tion geometries with larger range variation and more humidity tended to have larger deviations from a straight-line fit, and path radiance tended to show a larger non-linearity than transmission. An example of this range-dependence is demonstrated in Fig. 15 for two built-in standard MODTRAN atmospheres, specifically Model 2 (Mid-Latitude Summer) and Model 6 (U.S. Standard 1976). These atmospheres were chosen because they correspond to higher and lower humidity atmospheres respectively.

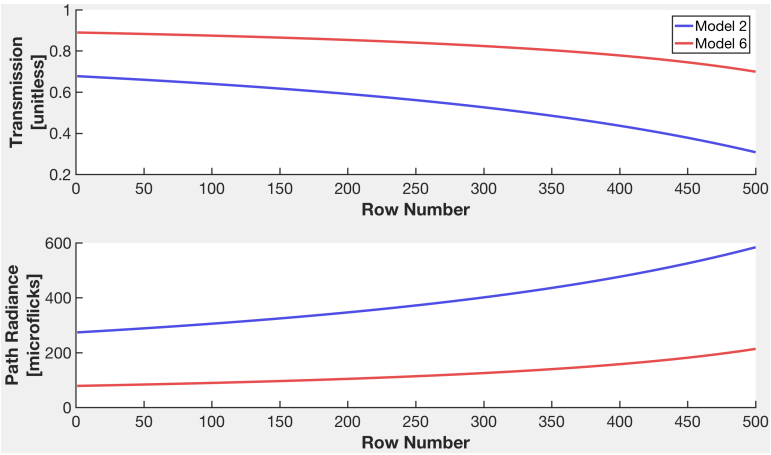

Figure 15. Transmission and path radiance of the 10 μm band for Model 2 and Model 6 MODTRAN atmospheres with respect to pixel row number for an observation geometry described in 3.4. Transmission and path radiance variation for this observation geometry may be modeled by low-order polynomials with respect to row number; the more moist atmosphere (Model 2 in blue) shows more curvature than the dryer atmosphere.

For the scenarios in this study, a quadratic fit for transmission and a quartic fit for path radiance were used. The precise order for the polynomials was determined by ensuring fit residuals had no clear structure and were on the order of the noise level, though the order may need to be increased for different viewing conditions than those studied here. By incorporating this range dependence into the model, one can ensure the AC algorithm does not suggest a change in atmospheric state across the image when the true differences are caused by variable viewing geometry.

3.3 Oblique ISAC

At its core, Oblique ISAC (OISAC) is an adaptation of the Full ISAC technique. In the Full ISAC technique, an unscaled transmission and path radiance is first calculated. Then, the 11.73 micrometer water band feature is analyzed to pick an atmospheric state to properly scale the earlier calculations. However, through the analysis of simulated data, performing this second step alone seemed to be sufficient and led to more accurate retrievals than scaling the original estimates. Thus, the OISAC technique described will only include an adaptation to the second half of the Full ISAC technique. This has the added benefit that one only needs to assume near-blackbody like pixels over the 11.73 μm feature rather than over the entire spectrum of interest; it is also faster and simpler to implement. This approach assumes that contributions from CO_2, O_3, and aerosols have low variability and may be modeled with standard atmospheric profiles. This assumption holds reasonably well for low altitude observations (i.e. below 10 km) in high visibility weather conditions [14].

In this alternate form which just uses the second half of the Full ISAC, OISAC is similar to AAC in that it is more of a model-based technique, driven solely by hyperspectral data around the 11.73 μm water band. As described in [14], these model-based approaches have the downside in being susceptible to uncertainties in radiative-transfer models (i.e. MODTRAN) and more vulnerable to spectral calibration errors, leading to less smooth emissivity and brightness temperature spectra as compared with ISAC. However, OISAC and AAC are not vulnerable to errors caused by spectral variability of assumed blackbody features, as they only require materials of smooth and high emissivity near the 11.73 μm water band, a condition satisfied by most natural land surfaces.[14] A thorough analysis detailing why it may be sufficient to pick an atmospheric state using only this narrow atmospheric feature is presented in [14].

Other assumptions that go into OISAC include those common to ISAC, e.g. the atmospheric state does not change over the scene, there are no significant changes in elevation, ground surface temperatures are hotter than the atmosphere, etc. For the synthetic scenes tested here, these first two assumptions will hold; however, in realistic scenes, particularly for those spanning larger areas, this may not always be the case. AC techniques would need further modification for scenes with a truly varying atmospheric state or with variable elevations (e.g. utilizing a digital elevation map).

In summary, OISAC simply estimates line contributions for the transmission and path radiance, $\bar{\tau}_\ell$ and $\bar{L}_{p,\ell}$, from the scene and then matches it to an atmospheric state using a pre-generated table. This match gives enough information to run MODTRAN for the geometries of interest, resulting in an estimate for the downwelling radiation as well as a row-dependent estimation of the transmission and path radiance.

The three basic steps of OISAC are as follows:

1. Generate look-up table of $\bar{\tau}_\ell$ and $\bar{L}_{p,\ell}$ for various atmospheric states
2. Estimate $\bar{\tau}_\ell$ and $\bar{L}_{p,\ell}$ from the scene
3. Find and model the best atmospheric match

Look-up Table Generation.

The goal of this first step is to generate a look-up table for the sensor and geometry of interest. With an estimate of $\bar{\tau}_\ell$ and $\bar{L}_{p,\ell}$ in the scene (Step 2), this table will be used to identify a specific atmospheric state characterized by a ground temperature, T_0, and a ground water vapor concentration, C_0.

To create the line contribution look-up table, a database of atmospheric states needs to be generated. Similar to what had been done in Appendix C of [46], a

variety of ground temperatures and ground water vapor concentrations were chosen and used to characterize temperature/water altitude profiles that had continuous parametric variability about the U.S. Standard 1976 atmosphere. These temperature/water profiles were fed into MODTRAN along with the U.S. Standard 1976 pressure profile to calculate a resulting transmission, path radiance, and downwelling contribution. Ground temperatures were varied from 260-320 K in increments of 5 K, while ground water concentrations varied from about 200-40,000 ppmv in twenty geometric steps (i.e. 200, 200×1.3, 200×1.3^2, ..., 200×1.3^{20}). Even though there is sizable spacing between increments for both, this technique eventually interpolates between increments. For the scene geometries explored here, the resolution was adequate; differences between similar atmospheric states would be more apparent for further observation distances and may require higher sampling rates. The lapse rate for temperature and water concentration followed the form of C10 and C11 in [46], resembling that of the U.S. Standard 1976 atmosphere.

Since the range and observation angle can change significantly throughout the image, MODTRAN needs to be run for multiple geometries for each ground temperature and water concentration. The scene was split into equally-sized strips, generating a MODTRAN database for the center of all strips as well as for the first and last rows. As alluded to before, the number of strips needed depends on atmospheric/geometrical factors and should be tailored for different scenarios. The transmission and path radiance from each of these runs were then interpolated to get their range-dependence across the entire scene for a given (T_0,C_0).

Rather than run MODTRAN in both radiance mode and transmission mode as in [46], an alternate method was developed to cut the use of MODTRAN in half and reduce a potential systematic bias in the line contribution estimates. The line contributions were found by first forward-modeling an oblique scene of blackbodies

at various temperatures (300 ± 5 K) through a given atmospheric state via (22), such that the blackbody scene matched the geometrical characteristics of the scene to be analyzed. Next, this blackbody scene was analyzed in the same method as the main scene (Step 2) with the exception that no points were eliminated in the fitting procedure since all points were blackbodies. Note that unlike the table in [46], since previous transmission and path radiance estimates are not scaled here, the total transmission and path radiance at each table entry need not be recorded.

Both the atmospheric database and table described above may be pre-generated, as they will not change for a given sensor and observation geometry.

Scene Estimation of $\bar{\tau}_\ell$ and $\bar{L}_{p,\ell}$.

The goal of this second step is to estimate the values of $\bar{\tau}_\ell$ and $\bar{L}_{p,\ell}$ for the scene of interest. In Step 3, these scene estimates will be compared with the table of values from Step 1.

To get a valid estimate for the line contributions, one needs to fit the most blackbody-like pixels in the scene. The first step in doing this is to create a list of pixels which are blackbody candidates. Borrowing from ISAC, this is done by determining which pixels have the highest spectral temperature in the most hits band (see [46] for details). It is necessary to use only these pixels in generating the scatterplot or else the resulting fit will be distorted by the non-blackbody pixels.

Using only these blackbody candidate pixels, the scatterplot is created to which a fit will then be generated. Since transmission and path radiance now vary as a function of row number, r, to get a proper estimate of $\bar{\tau}_\ell$ and $\bar{L}_{p,\ell}$, one must include this range-dependence in the fit. By observing the residuals between the 3-D scatterplot and various surface fits, it was found that a quadratic range-dependence for $\bar{\tau}_\ell$ and quartic range-dependence for $\bar{L}_{p,\ell}$ sufficiently captured the range variation for the observation

geometries considered. Thus, the surface given by

$$\bar{L}(\bar{L}_0, r) = \bar{\tau}_\ell(r)\bar{L}_0 + \bar{L}_{p,\ell}(r), \tag{27}$$

was fit to the blackbody candidates where $\bar{\tau}_\ell(r) = \sum_{i=0}^{2} c_{\tau,i} r^i$ and $\bar{L}_{p,\ell}(r) = \sum_{i=0}^{4} c_{L,i} r^i$. Since blackbody pixels lie at the bottom of this surface, an iterative approach was taken to eliminate the least blackbody-like pixels.

Unlike in ISAC where $\bar{\tau}_\ell$ and $\bar{L}_{p,\ell}$ were captured by two numbers, range-dependent functions for these quantities are now available. However, after propagating of uncertainty error in the fit coefficients, it was found that the middle row tended to have the smallest relative uncertainty. The larger uncertainties at the ends of the fit are as expected for polynomial fitting of uniformly distributed data points with constant, normally distributed data errors. The mathematical theory behind this non-intuitive fitting characteristic is developed by [32], who explains "the error in the value of the fitted function, however, always depends on x, even when the standard deviations of the data errors, σ_i, are all the same, independent of x." This difference in uncertainty between the center and ends of the fit was verified using Monte Carlo analysis over a variety of atmospheric conditions and noise levels. It was further confirmed after propagating fit uncertainties for $\bar{\tau}_\ell$ and $\bar{L}_{p,\ell}$; an example fit with its corresponding uncertainty for the Model 6 scene, described later in 3.4, is shown in Fig.16, where one may observe larger uncertainties towards the closer and further ranges of the fits. Since the center row often had the lowest uncertainty, estimates for $\bar{\tau}_\ell$ and $\bar{L}_{p,\ell}$ were evaluated for the center row of the image.

Additionally, using the uncertainties in the fit coefficients above, it was found that the percent uncertainty in the path radiance was often 4-8 times larger than the transmission for the scenarios considered. This relative uncertainty is expected, as uncertainty analysis of (27) for even the noiseless (i.e. $\delta\bar{L} = \delta\bar{L}_0 = 0$) blackbody scene

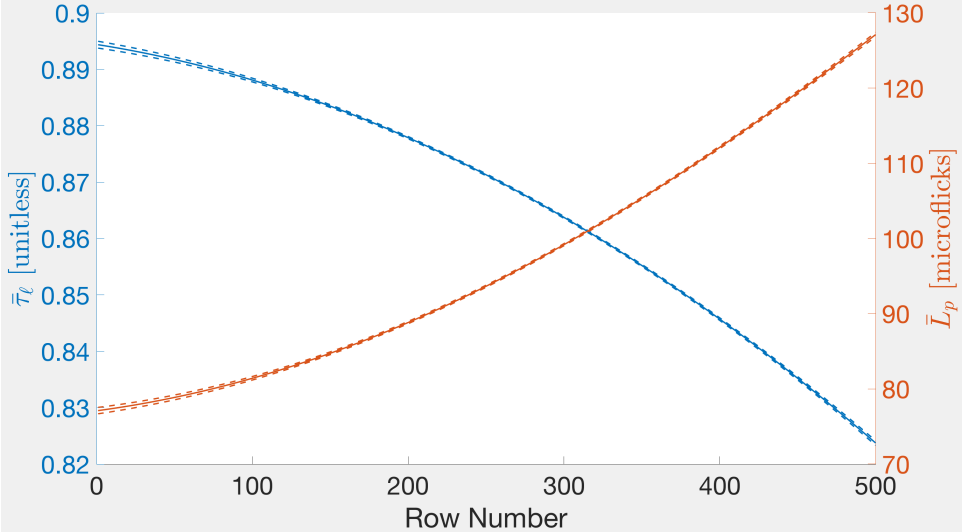

Figure 16. Best fit line transmission (blue) and line path radiance (red) for the Model 6 scene described in 3.4 are shown as solid lines. Dashed lines represent propagated uncertainty from analysis of the fit uncertainties, showing larger uncertainty towards the closer and further ranges of the scene.

used to calculate line contribution look-up table gives $\delta \bar{L}_{p,\ell} \approx \bar{L}_0 \delta \bar{\tau}_\ell$. Multiplying and dividing both sides by the line transmission and path radiance respectively gives

$$\frac{\delta \bar{L}_{p,\ell} / \bar{L}_{p,\ell}}{\delta \bar{\tau}_\ell / \bar{\tau}_\ell} \approx \frac{\bar{\tau}_\ell \bar{L}_0}{\bar{L}_{p,\ell}}. \tag{28}$$

Using typical values for the scenarios considered (i.e. $\bar{\tau}_\ell = 0.9$, $\bar{L}_0 = 600$, $\bar{L}_{p,\ell} = 150$), this expression yields $\frac{\delta \bar{L}_{p,\ell} / \bar{L}_{p,\ell}}{\delta \bar{\tau}_\ell / \bar{\tau}_\ell} \approx 3.6$. From this analysis, it was helpful to record the relative uncertainty between $\bar{\tau}_\ell$ and $\bar{L}_{p,\ell}$ at this step (calculated using the uncertainties in the fit parameters), to serve as a relative weighting in Step 3 when finding the best match.

Model the Best Atmospheric Match.

By comparing the scene estimate of $\bar{\tau}_\ell$ and $\bar{L}_{p,\ell}$ from Step 2 with the table generated for various atmospheric states in Step 1, one can find the best atmospheric match identified by (T_0,C_0). Since the relative uncertainty in $\bar{L}_{p,\ell}$ will be larger than

$\bar{\tau}_\ell$, it was necessary to weight the terms differently when finding the best match in the table. This weighting was calculated previously in Step 2.

Finally, with this estimate of (T_0,C_0), an atmospheric profile may be generated and fed directly into MODTRAN. Coupling this atmospheric profile with a changing geometry meant to span the observation characteristics of the original scene, one has an estimation for the downwelling radiation as well as row-dependent transmission and path radiance.

3.4 Results

Here there will be a detailed comparison between four different AC techniques, specifically between Segmented ISAC, where ISAC has been applied independently to ten horizontal segments of the scene (as had been done in [38], but scaling is done here), OISAC applied to the image as a whole, and FLAASH-IR applied with and without image segmentation. Segmentation for FLAASH-IR was done in the same manner as for ISAC. One metric used to compare these AC algorithms is the Pearson correlation coefficient given by

$$r = \frac{\sum_{i=1}^{n}(x_i - \bar{x})(y_i - \bar{y})}{(n-1)\sigma_x\sigma_y}, \tag{29}$$

where $\bar{x}$ and $\bar{y}$ are the mean and σ_x and σ_y are the standard deviation of two n-dimensional vectors. These techniques are compared using both synthetic and measured hyperspectral images.

Synthetic Scene Results.

Synthetic scenes were generated by forward modeling random materials at random temperatures through standard MODTRAN atmospheres. Each pixel from a 500×128 scene was assigned a random temperature (300 ± 5 K) and material. Randomly

assigned materials and corresponding emissivities came from a group of 23 different materials selected from the ASTER spectral library [4], ranging from blackbody to reflective. It is assumed that the sensor has enough spatial resolution such that each pixel is of one material and is at a single temperature, and any temperature/emissivity correlation will be ignored, assuming they are independent.

These pixels were forward-modeled via (22) where the atmospheric parameters were calculated via MODTRAN for sensor geometries which depend on the row number of the pixel. The atmospheric states chosen were the MODTRAN Model 2 and Model 6 standard atmospheres. Sensor and scene elevations were 1 km and 0 km respectively, and the declination angle of the sensor was chosen based on the sensor-scene range of the pixel row. Each row of 128 pixels was equidistant from the sensor. The 250th row, at the middle of the scene, was chosen to have a declination angle of 15 degrees. The spectral resolution was selected to be 50 nm and iFOV was set to 550 μ-radians. From the number of pixels, declination angle, and iFOV, the range of the atmospheric path varied from 2.6-8.1 km. After the at-sensor spectral radiance was generated, Gaussian-distributed zero-mean noise was added with a standard deviation of $1 \cdot 10^{-6} \frac{\mathrm{W}}{\mathrm{cm}^2 \cdot \mathrm{sr} \cdot \mu\mathrm{m}}$, i.e. 1 μ-flick.

The variation in the transmission and path radiance for the two atmospheres in shown in Fig. 17. The larger transmission and smaller path radiance corresponds to the first row of the image (which is at the closest distance). Only the first and final rows are shown, but there is a continuous variation in transmission and path radiance throughout the scenes. These plots show that these atmospheric quantities can sometimes vary by a factor of two for this geometry.

Upon application of the three atmospheric compensation algorithms on the scene with the Model 6 atmosphere, the retrieved transmission and path radiance for the first and last rows of the image are shown in Fig. 18. The performance in comparison

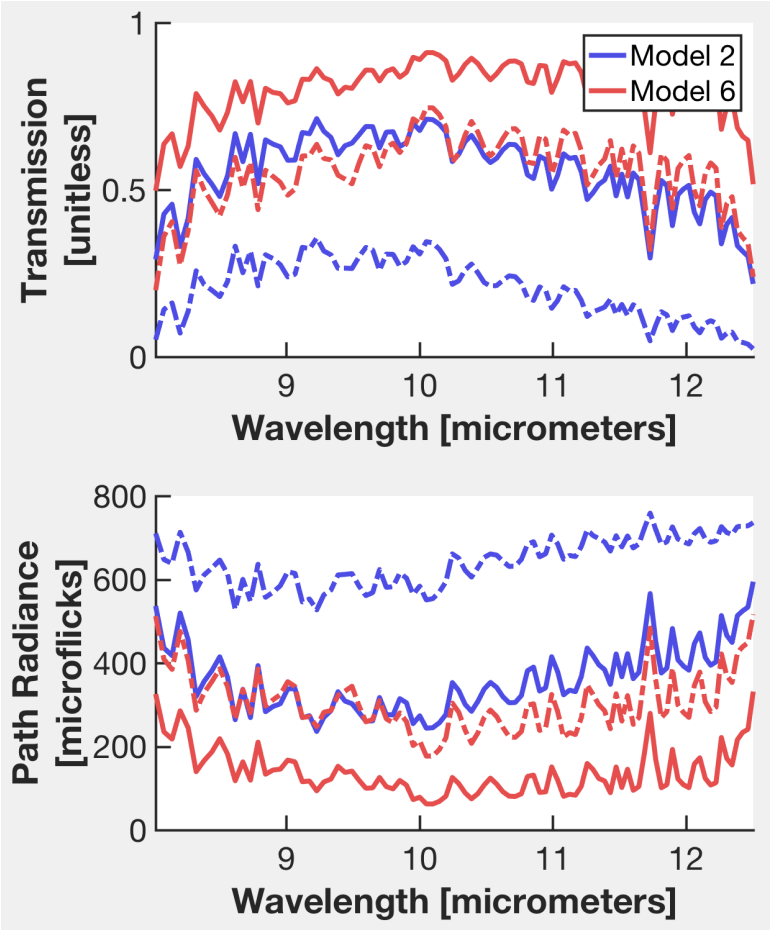

Figure 17. Transmission and path radiance of the first (solid) and last row (dashed) of the synthetic scene for the two MODTRAN model atmospheres.

with truth is shown in Fig. 19. Here the spectral RMS difference with respect to truth is plotted as a function of row number. One may see that the transmission and path radiance estimated with OISAC had virtually no range-dependent RMS error and that the path radiance error is on the order of the noise level; because the continuous range variation is built into the model, the RMS error is nearly flat. Alternatively, FLAASH-IR had the smallest error towards the middle of the image, and because it had not been modified to account for variations in range, the error increased towards the edges of the scene. Segmented FLAASH-IR had a mixed performance. For half the rows in the scene, it had superior path radiance estimates than the standard FLAASH-IR; however, three of the segments (rows 251-300, 301-350, 451-500) had extremely poor estimates (e.g. unrealistic path radiances as high as $10^3 1$ microflicks). This performance degradation is most likely due to the reduction in scene data from segmentation. As adapting FLAASH-IR was not the focus of the study, the optimal number of image segments was not explored, and because of the poor transmission and path radiance estimates, Segmented FLAASH-IR results will not be shown. From these figures, one may see the importance of adapting the application of AC techniques to the varying scene geometries.

To get an estimate of how target detection would be impacted by the different AC algorithms, retrieved and true emissivities were compared. Retrieved emissivities were calculated by using the true temperature map and the atmospheric estimates. A comparison of true and retrieved emissivity for one of the materials (roof slate) at both the first and last rows of the image is shown at the top of Fig. 20. The bottom left of the same figure shows the mean RMS difference between retrieved and true emissivities as a function of row number. RMS difference, a metric used more for comparing spectrally flat materials, was smallest for OISAC. On the bottom right of Fig. 20, the mean correlation is shown as a function of row number. Results from

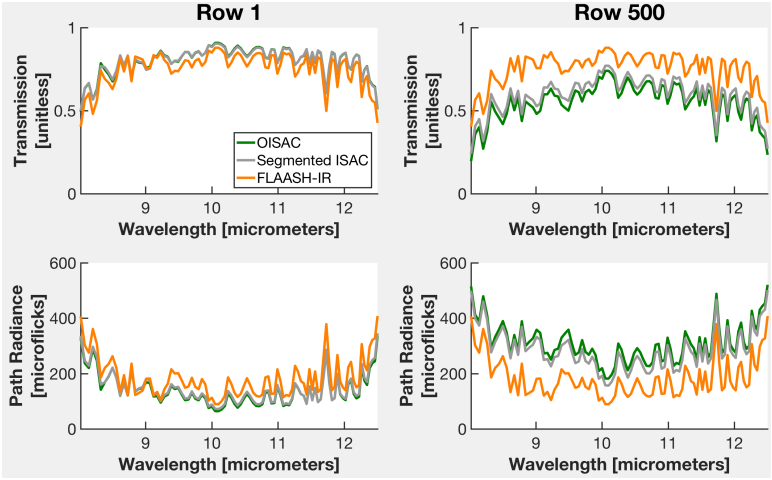

Figure 18. Transmission and path radiance for the three AC techniques for the first and last rows the Model 6 synthetic scene.

OISAC had the highest spectral correlation, suggesting that emissivity retrievals using this technique will perform better in target detection algorithms. Plots for the other 22 materials show similar results. These results suggest that use of OISAC may lead to more accurate emissivity retrieval, particularly for pixels at further ranges. For both plots, FLAASH-IR shows degraded performance with respect to range because it had not been adjusted to account for range variation.

As a final analysis of the AC results from the synthetic dataset, the correlation between retrieved emissivities and the atmospheric transmission was explored. First, a Temperature-Emissivity Separation algorithm from [7] was executed for each pixel in the scene using each AC result. Then the correlation between the retrieved emissivity and atmospheric transmission was calculated. The correlation maps for the three AC techniques are shown in Fig. 21. One may see that the retrieved emissivities using OISAC have lower correlation with the atmospheric transmission than the other techniques, suggesting fewer atmospheric residuals in the retrieved emissivities. For FLAASH-IR, one may see that retrieved emissivities at further ranges are more correlated with atmospheric transmission, suggesting that these retrieved emissivities

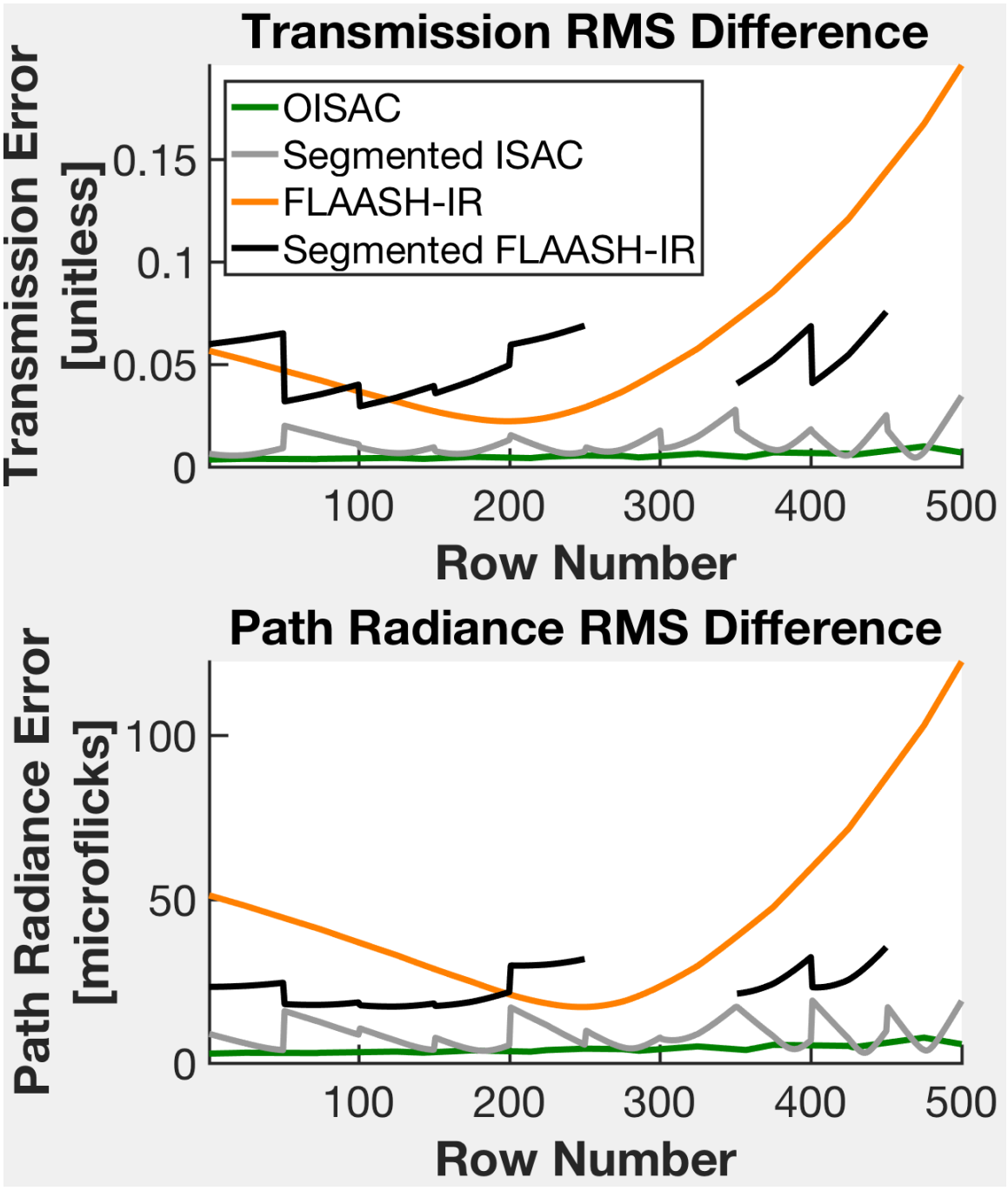

Figure 19. Plots of the RMS difference between truth and the result from AC for the Model 6 synthetic scene, averaged spectrally.

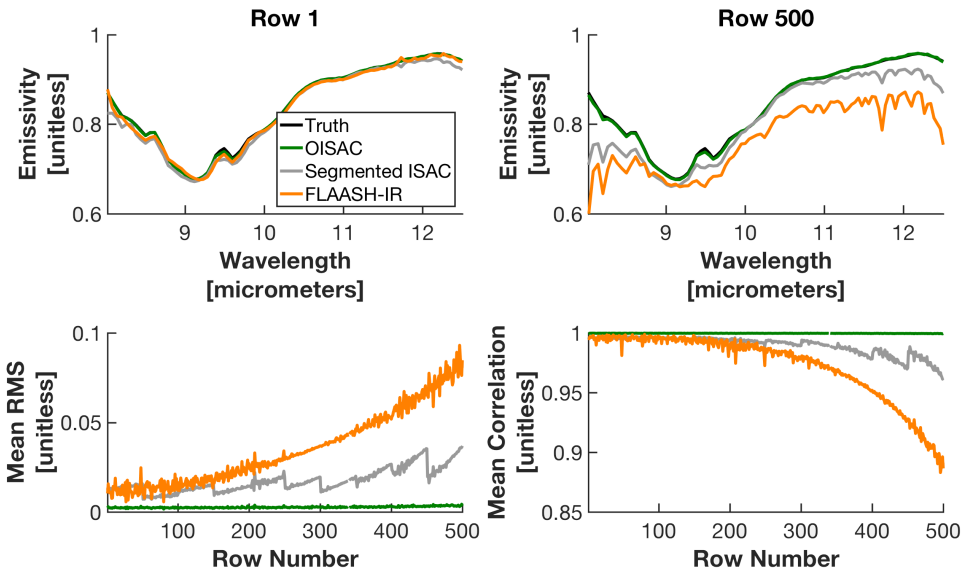

Figure 20. Comparison of retrieved emissivity vs. truth for roof slate material in the Model 6 synthetic scene. Top: average retrieved emissivity for Row 1 (left) and Row 500 (right). Bottom: average RMS difference (left) and correlation (right) between retrieved and true emissivity with respect to row number.

have more residual atmospheric features.

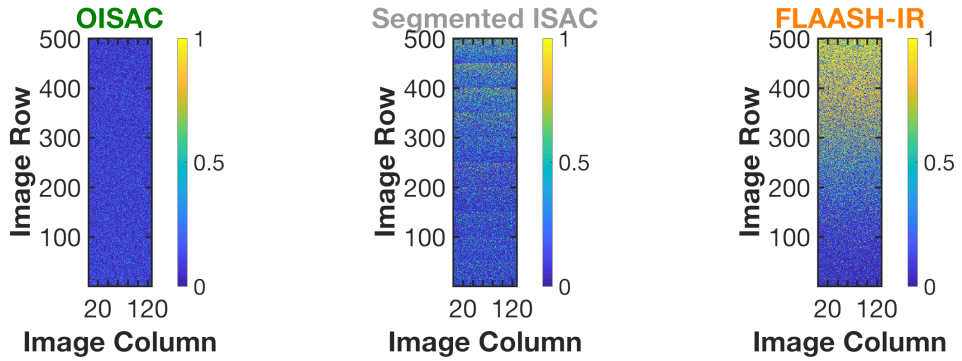

Figure 21. Colormaps of the squared correlation between retrieved emissivities and the atmospheric transmission for the Model 6 synthetic scene.

To summarize the results from the synthetic scene analysis, it may be seen that attention to the range variation of atmospheric transmission and path radiance is important for the observation geometry considered. Results were similar for the other model atmosphere tested (Model 2) and for the other ASTER database ma-

terials. Because image segmentation was not performed for FLAASH-IR, it had a degraded performance. Additionally, as FLAASH-IR had been developed for more realistic scenes, the lack of robustness in this simplistic synthetic dataset may degrade FLAASH-IR (e.g. correlation between material and temperature were ignored and treated them independently). Finally, when comparing the results of image segmentation using the nadir-developed ISAC technique with the oblique-developed OISAC technique, one may see that OISAC did better at retrieving the true atmospheric state.

Mako Scene Results.

The Mako dataset that was analyzed was captured by the Aerospace Corporation's Mako airborne sensor, described in [17]. The camera has a spectral sampling of 44 nm and an iFOV of 547 microradians. As part of the New Dawn Collect, this scene was taken on 15 August 2016 at 17:05 local time over Long Beach, CA from a Twin Otter at 12,210 ft. The 1600×128 images extended from nadir (row 1) to about 50 degrees from nadir (row 1600). The scene-sensor range of the atmospheric path extended from 3.7-5.8 km. Since four frames were co-added for the collect, the Noise Equivalent Spectral Radiance is estimated to be less than 0.6 μF in each spectral channel.

Upon application of OISAC, Segmented ISAC, and FLAASH-IR on the Mako Scene, the retrieved transmission and path radiance for the first and last rows of the image are shown in Fig. 22. Segmented FLAASH-IR results were similar to FLAASH-IR; it was found that for these larger scene segments, Segmented FLAASH-IR did not show the problems it had when analyzing the smaller synthetic scene segments. The segmented version of FLAASH-IR had mean spectral differences of transmission and path radiance of 0.02 and 25 microflicks respectively when compared with

the standard FLAASH-IR. Because of these small differences (e.g. OISAC had differences nearly 2-3 times larger), transmission and path radiance results from Segmented FLAASH-IR are not shown.

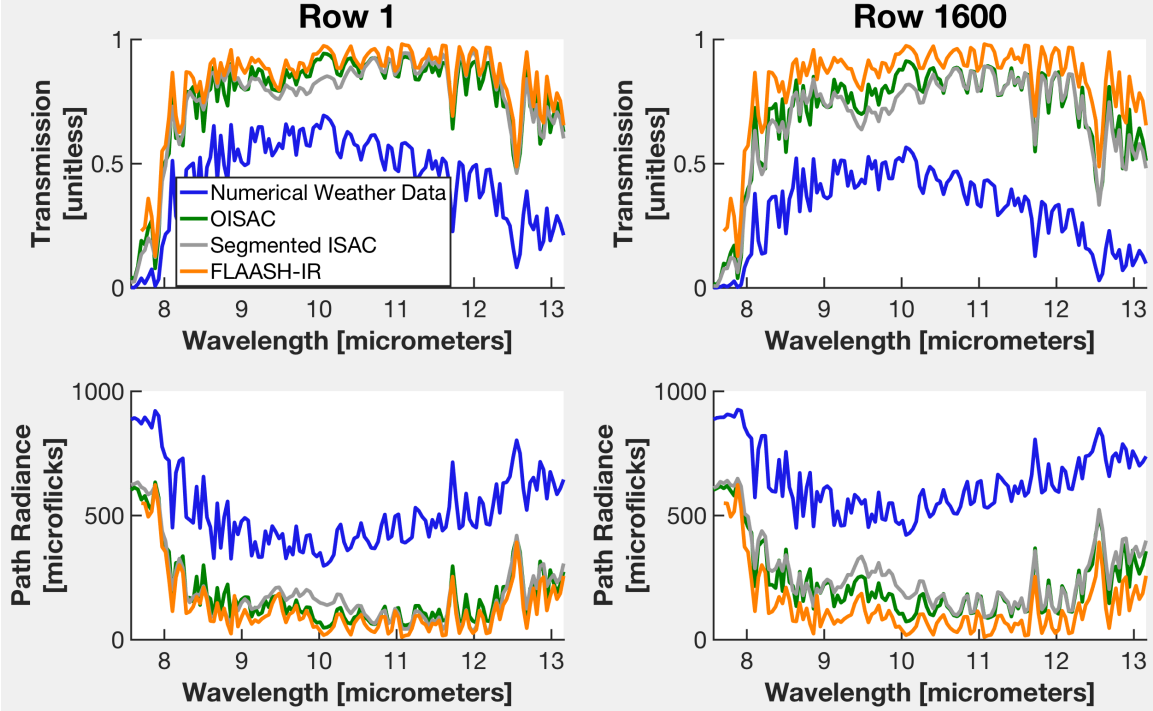

Figure 22. Transmission and path radiance for the three AC techniques for the first and last rows of the Mako scene. Results from the numerical weather data are also shown.

Comparing the first and last row estimates in Fig. 22, OISAC and Segmented ISAC show the expected range-dependent trends, with transmission decreasing and path radiance increasing with range. Comparing this variation with the synthetic scenes in Fig. 18, one may notice a smaller range variation in the atmospheric parameters. Because of this, one may expect the performance benefits of the nadir techniques to be more comparable with the oblique algorithm. The entire range-dependence is captured in Fig. 23, which shows spectrally averaged transmission and path radiance with respect to range for the different AC algorithms. Here, we can

note the differences between nadir techniques, techniques employing segmentation techniques, and oblique techniques. Of these, both the constant and stair-step pattern of the former techniques are nonphysical, as opposed to the smoothly varying oblique AC estimate. Additionally, one may observe that the range-dependent trends between adjacent segments may sometimes be nonphysical, incorrectly suggesting that transmission and path radiance temporarily trend opposite to the overall trend; Segmented ISAC demonstrates this feature in segment covering rows 161-320 and Segmented FLAASH-IR in rows 801-960.

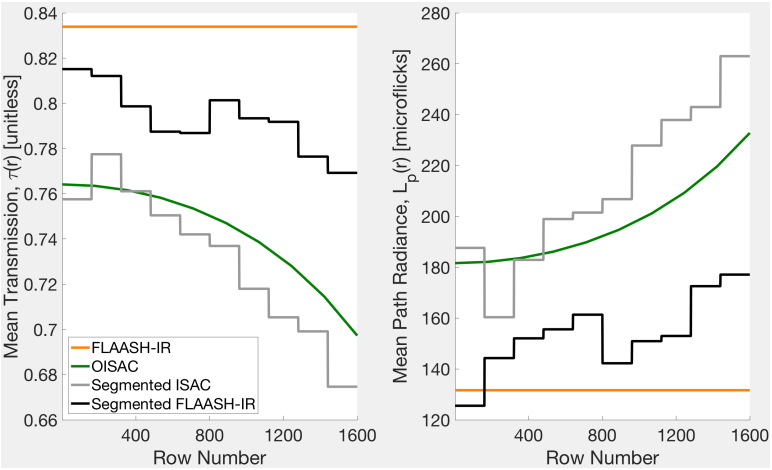

Figure 23. Plots of the spectrally averaged transmission (left) and path radiance (right) with respect to range for the different atmospheric estimates.

Results from MODTRAN simulations based on numerical weather data for the date/location of the collect are also shown in Fig. 22. This numerical weather data was obtained from the National Oceanic and Atmospheric Administration (NOAA) National Operational Model Archive and Distribution System (NOMADS) [34]. Atmospheric estimates from the numerical weather data differ significantly from the AC results, suggesting a much higher water concentration. To understand the impact of these different atmospheric estimates and in an effort to determine which estimates are closer to physical truth, which is unknown for this hyperspectral dataset, observed

spectra were compared with forward-modeled spectra using atmospheric estimates from both the numerical weather data and OISAC. From the mean LWIR image of the scene, road pixels were identified both at near and far ranges of the scene. The observed spectra for these two roads are shown in Fig. 24, where each road spectra was taken as an average over approximately 50 nearby pixels. Forward-modeled radiances are also shown and were calculated using (22) and (23), where the emissivity estimate for asphalt from the ASTER database was used and temperature was chosen to minimize the RMS difference between the observed and forward-modeled signals. The weather data suggested a relatively large and likely unrealistic temperature difference between the two roads; the far road had a temperature of 340.8 K and the close road was given a temperature of 333.2 K. OISAC used 326.4 K and 324.9 K for the far and close roads, respectively. Additionally, OISAC had relatively small RMS errors between the observed and forward-modeled signal of 23.9 and 19.3 microflicks for the far and close roads, while the numerical weather estimates had RMS differences of 72.0 and 61.7 microflicks. The spectral differences are particularly noticeable below 8 micrometers, where the numerical weather results significantly differed from the observed radiance. This and subsequent analysis of the weather data suggests that it is less accurate than AC results, both demonstrating the need for proper AC (i.e. as opposed to relying entirely on weather data) as well as highlighting the difficulty of obtaining an accurate estimation of truth for this real-world dataset.

As had been done with the synthetic scene, Temperature-Emissivity Separation was applied across the entire image to see how correlated the retrieved emissivities were with the transmission. The first dozen spectral channels, extending from 7.57-8.11 μm, were excluded in the analysis; high transmissions losses in this spectral region negatively impacted all retrieval algorithms. The correlation between retrieved emissivity and transmission are shown in Fig. 25. Just as had been observed with the

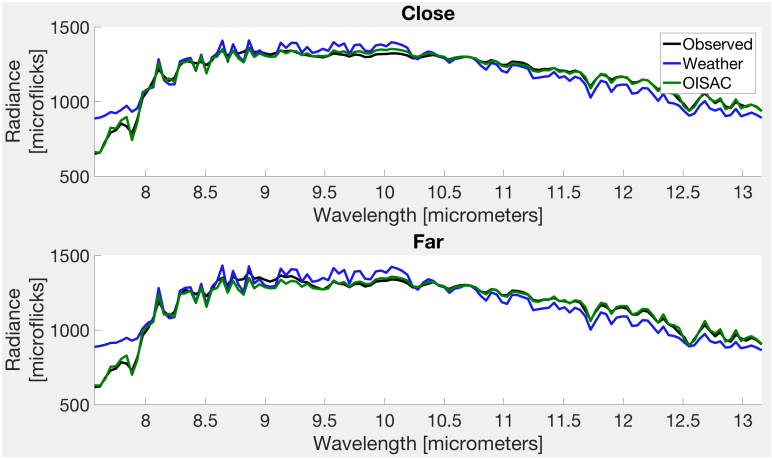

Figure 24. Observed radiance of road pixels at close and far ranges (black) with forward-modeled radiances using transmission, path radiance, and downwelling estimates from OISAC (green) and numerical weather data (blue).

synthetic scenes, retrieved emissivity spectra from FLAASH-IR tended to be more correlated with atmospheric transmission with respect to row number, suggesting that more atmospheric features were present at further ranges. Emissivities retrieved via OISAC also show more correlation with the atmospheric transmission than in the synthetic scenes; however, the correlation did not show range-dependence and was the lowest among all methods. The segmented techniques tended to have stronger correlations across the image.

Continuing the qualitative analysis, k-means clustering based on cosine distance metric was performed on the retrieved emissivities. When dividing the scene into, e.g. ten classes, OISAC showed far fewer artifacts in the clustering process. Both the numerical weather data and FLAASH-IR showed range-dependent artifacts, evident in Fig. 26. One may observe from the mean LWIR image (left-most subimage), that while road-like materials are present throughout the scene, use of these two atmospheric estimates leads to emissivities with spectral differences more dependent on range rather than actual material differences. Unlike these two atmospheric estimates, emissivities retrieved via OISAC may be more realistically clustered due to spectral

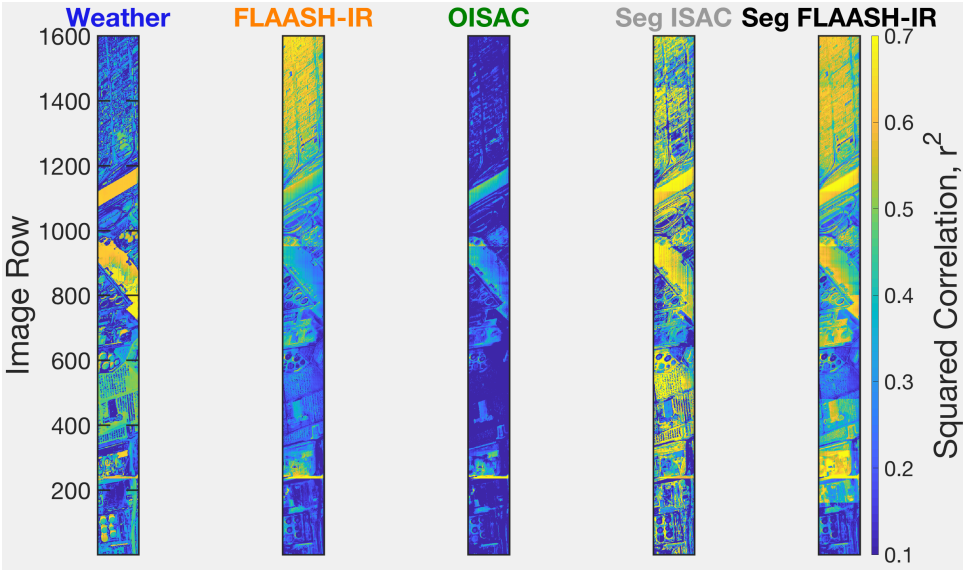

Figure 25. Colormaps for the Mako scene of the squared correlation between atmospheric transmission and retrieved emissivities from the different atmospheric estimates.

shape; this is demonstrated in Fig. 26, as road pixels at very different ranges were successfully assigned the same class. The final two techniques based on segmented AC had their own inconsistencies. Artifacts from image segmentation were significant as evident by the sharp, unnatural lines dividing portions of the image. Because each segment was compensated independently, each segment of the image had the freedom to retrieve a completely different atmospheric state that was inconsistent with the rest of the scene.

Next, retrieved emissivities of objects both near nadir and off-nadir were compared. Using context imagery, cylindrical objects and roads throughout the scene were identified. In the visible, there were white cylinders (which appear gray in the mean LWIR image shown at top in Fig. 26) and shiny/metallic-looking cylinders (which appear black in the mean LWIR image). While truth data was not available, it was possible to check for residual atmospheric features in retrieved emissivities and to compare emissivities for similar-looking materials at different ranges throughout

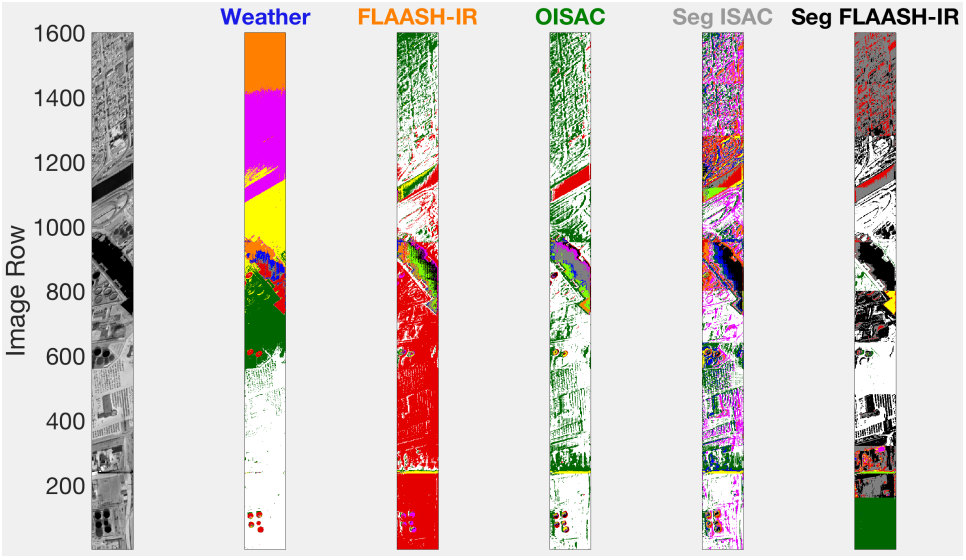

Figure 26. The leftmost subimage is the mean LWIR image of the Mako scene. The other subimages show the results of k-means clustering the retrieved emissivity from the different atmospheric estimates.

the scene. The retrieved emissivities are shown in Fig. 27, where the solid lines are for the objects near nadir and the dashed lines were for the off-nadir objects. Each emissivity was an average over 40-80 pixels. The white cylinders were taken from approximately rows 590 and 980, shiny cylinders from rows 60 and 845, and the roads from rows 50 and 1520. In general, while FLAASH-IR tended to have the smoothest retrieved spectra, all of them had residual atmospheric structure. This is highlighted in their non-zero correlation with atmospheric transmission, shown in the last column of Table 2. While the OISAC-retrieved spectra have evident atmospheric features, the correlation of these spectra with transmission were among the lowest for the three techniques. OISAC also had the highest correlation between emissivities of the same material at the two different ranges (second column of Table 2). FLAASH-IR performed very well for the shiny cylinders (high correlation for near/far objects with a low atmospheric correlation). FLAASH-IR is expected to have a better retrieved downwelling radiance compared with ISAC-based techniques that do not directly esti-

mate downwelling, and this downwelling contribution is more significant for reflective materials. On the other hand, FLAASH-IR had the most difficulty with the roads, as could have been predicted from the k-means analysis. This difficulty is especially highlighted because the road pixels had the largest range variation, as spectra could be compared between both extremes of the image.

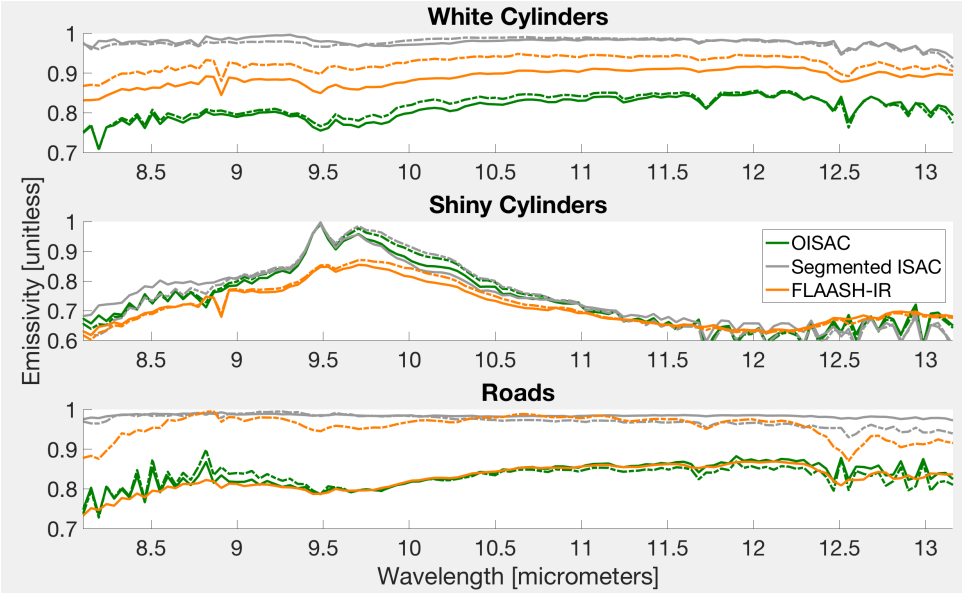

Figure 27. Retrieved emissivities of objects (truth unknown) at different ranges throughout the image. Dashed lines refer to objects further from nadir. From top to bottom: white cylinders, shiny cylinders, roads. Residual atmospheric effects are present in the retrieved spectra.

Since the ground surface temperatures were unknown for the scene, these were retrieved as part of the Temperature-Emissivity Separation. These temperature estimates are shown in Fig. 28. Results suggest surface temperatures around 315-325 K (≈107-125°F), reasonable temperatures for a summer afternoon in California. Of interest in the FLAASH-IR results is the suggestion that ground surface temperature decreases with range. This is most likely an artifact of FLAASH-IR's lack of built-in atmospheric range-dependence and suggests that when FLAASH-IR is maximizing smoothness of further pixels, it is using temperature as its free parameter to

MAKO EMISSIVITY CORRELATION

AC Method	with near nadir	with transmission	
OISAC	0.960	0.589	(a)
Segmented ISAC	0.758	0.719	
FLAASH-IR	0.890	0.653	
OISAC	0.997	0.277	(b)
Segmented ISAC	0.969	0.343	
FLAASH-IR	0.995	0.251	
OISAC	0.898	0.327	(c)
Segmented ISAC	0.798	0.530	
FLAASH-IR	0.472	0.810	

Table 2. Correlation of off-nadir retrieved emissivity with both near nadir retrieved emissivity and with atmospheric transmission for white cylinders (a), shiny cylinders (b), and roads (c). OISAC shows the highest spectral correlation with similar targets at two different locations (second column) and low correlation with the atmospheric transmission.

pseudo-compensate for varying range. While this artifact resulting from FLAASH-IR's inflexibility is non-physical, it may still lead to adequate emissivity retrieval.

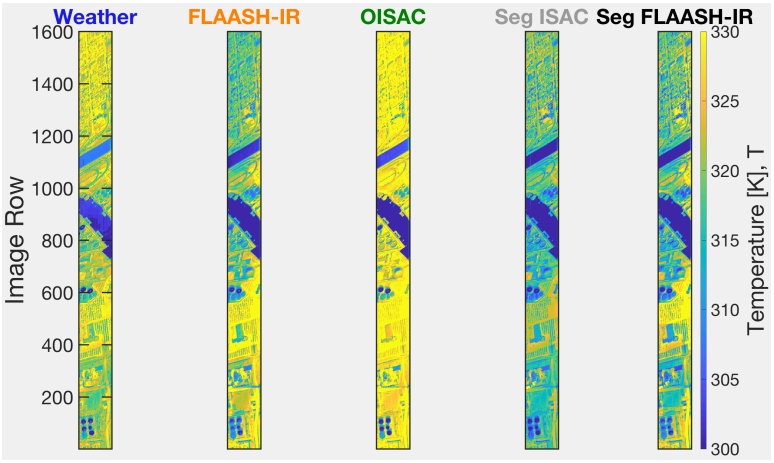

Figure 28. Colormap of retrieved temperatures for the Mako scene for the different atmospheric estimates.

The emissivity spectra for the materials in the scene were unknown; however, further analysis was done for the two large bodies of water (a channel in the Inner Harbor of the Port of Long Beach located around row 800, and the Los Angeles River

around row 1100). Using atmospheric estimates from the three AC techniques, the observed radiance (averaged over 1500 water pixels for each body of water), and the emissivity of water from the ASTER database, the spectral temperature was calculated. The mean spectral temperature with one standard deviation for each of the two rivers is captured in Table 3. One may see that the river closer to nadir (i.e. near Row 800) is most likely at a cooler temperature with a smaller uncertainty. Additionally, the mean spectral temperatures for all three techniques agree within one standard deviation. Last, OISAC produced the most spectrally flat temperature estimate, as it had the smallest spectral standard deviation.

MAKO RIVER ANALYSIS – RETRIEVED TEMPERATURE

AC Method	Row 800 River	Row 1100 River
OISAC	296.00±0.29 K	299.61±0.38 K
Segmented ISAC	295.75±0.29 K	298.82±0.75 K
FLAASH-IR	295.66±0.45 K	298.86±0.52 K

Table 3. Assuming that both bodies of water had an emissivity of water (from the ASTER database), a spectral temperature was calculated for each method at each wavelength. Shown are the mean spectral temperature with one standard deviation. With the least uncertainty, OISAC had the least variation in the retrieved temperature for multiple spectral channels.

Using these mean spectral temperatures, the emissivity was then calculated for each of the AC methods and compared it against the known emissivity of water. Just as in the temperatures, these emissivities were an average of 1500 pixels per river. From these results, the retrieved emissivity using OISAC had the lowest RMS difference with the emissivity of water, shown in Table 4.

In Fig. 29, the spectral temperatures and emissivities for each of the methods are shown. It is important to note that while the RMS difference is relatively low (<1%), there are still many AC artifacts in the retrieved emissivity for all methods (which was suggested earlier when the correlation across the scene between retrieved emissivity and atmospheric transmission was explored).

MAKO RIVER ANALYSIS – RMS DIFFERENCE IN RETRIEVED EMISSIVITY

AC Method	RMS Difference
OISAC	0.0054
Segmented ISAC	0.0084
FLAASH-IR	0.0067

Table 4. Using the mean spectral temperature for both rivers (previously calculated assuming an emissivity of water), the emissivity was computed for the rivers and compared against the true emissivity of water. The RMS difference between these two is shown above.

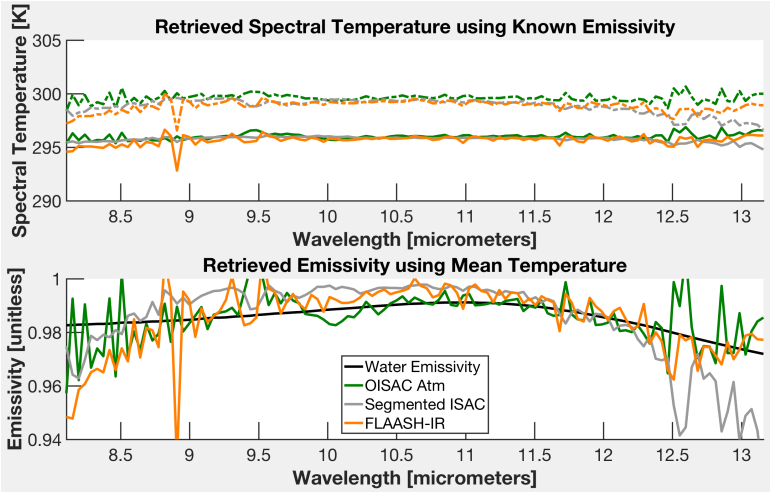

Figure 29. Top: using the known emissivity of water, the spectral temperature is shown for the two rivers. The cooler river (row 800) is the solid line; the warmer river (row 1100) is the warmer river. Bottom: using the mean spectral temperature for each river, the average retrieved emissivity is shown.

3.5 Discussions and Conclusions

While not conclusive, early analysis has shown that the proposed OISAC technique, which hinges on incorporating range-dependence in atmospheric transmission and path radiance, is comparable to other AC techniques. OISAC's ultimate usefulness heavily depends on observation characteristics (particularly, total range variation in the scene and/or ground sample distance). For more extreme slant paths that have a larger range variation, OISAC would be more useful (as long as the atmospheric state is still constant over the entire scene). However, it is expected to be comparable to image segmentation techniques for scenes with small ground sample distances. The advantage of OISAC comes from its ability to use more of the data in the scene, but as sensors improve, segmented AC techniques may have enough data for decent statistics. One additional benefit of OISAC is that it is able to process a scene faster than segmented techniques, as it is able to analyze the entire scene at once.

Regarding future work, OISAC requires additional testing using real-world hyperspectral data, especially where ground truth is known. Oblique LWIR hyperspectral datasets are not as ubiquitous as nadir datasets, particularly ones with large range-variation between the first and last row. Increasingly robust synthetic scenes where truth is known could also be beneficial. In particular, synthetic scenes generated using more realistic atmospheric profiles. The standard atmospheric models in MODTRAN have smooth and continuous temperature and water profiles, which is uncharacteristic of real weather.

It would also be useful to explore limitations of OISAC. Specifically, OISAC had assumed a near constant elevation as well as a uniform atmospheric state across the scene. However, since oblique scenes typically span larger areas than nadir ones, these assumptions will not always hold. Understanding the limits of these two assumptions would inform the user of the scenarios when image segmentation would be

more appropriate. Impact from BRDF (bidirectional reflectance distribution function) effects, which are more evident when targets are viewed at an angle, might also need to be considered in these oblique viewing geometries. Additionally, since OISAC bears a strong resemblance to AAC in that it uses only the 11.73 micrometer water band to determine the entire spectral characteristics of the atmosphere, it has similar limitations (in addition to the requirement of near blackbody-like materials over the 11.73 μm band). The assumption that aerosols and O_3 can be modeled with standard atmospheric profiles requires low altitude measurements (<10km) in high visibility weather conditions.

Altogether, this research demonstrates how one might adapt a nadir-based AC technique for oblique sensing environments. This technique uses a physics-based modeling approach to tie together different parts of the image to improve the statistical uncertainty and accuracy of atmospheric compensation. This research also highlights the performance impacts of not adapting current AC algorithms for scenarios with range variation.

IV. Radiance Detrending

Here, the second novel oblique AC technique developed in this research, Radiance Detrending, will be covered. This technique exploits the fact that the ground-leaving radiance, which is not expected to have a range-dependence, is given a range-dependent modification to it based on the atmospheric state. If the correct atmospheric state is found, then this trend may be corrected.

An explanation of this technique begins with a discussion of the theory behind the RD technique. First, a visualization of this range-dependent trend for a variety of atmospheric states as well as the ground-leaving radiance after it has been detrended will be shown. Next, an initial metric to quantify how well the radiance is detrended and then explore factors which may cause difficulty in estimating this metric for a simplified scene will be introduced. After illustrating this technique for a basic scene, further complications into the synthetic model that are more representative of realistic scenes will be added. The theory section will end with a robust metric for gauging an atmospheric state's ability to detrend the scene radiance.

After discussing the theory behind RD, details how it this technique was implemented will be presented. Finally, the results of applying this technique to a variety of synthetic and real datasets will be discussed. The end of the results section will compare RD and OISAC for reflective scenes and variable downwelling contributions.

4.1 RD Theory

This section explains the theory behind RD. The discussion includes the motivation behind the technique, the metric used to identify the correct atmospheric state, factors which lead to uncertainty in picking the correct atmospheric state, and ways to minimize this uncertainty to improve compensation of the atmosphere.

Detrending Observed Radiance.

Compared to nadir scenes, one key difference in oblique scenes is that the viewing geometry gives a distinct range-dependence to the observed radiance. From radiative transfer theory (2.2), it's evident that this range dependence is based on viewing geometry, atmospheric state, and object properties (i.e. temperature and emissivity). To understand how the observed radiance might change as a function of range, $T = 300 \pm 5$ K blackbody scenes were forward-modeled for three different MODTRAN standard atmospheres using the same geometry and viewing conditions described in 3.4. Fig. 30 shows the observed radiance for these scenes, where the only difference is atmospheric state. One may note that the observed radiance has a different curvature for the different atmospheric states. The RD technique is ultimately based on finding the best atmosphere which detrends this observed radiance and is based on the assumption that the range-dependence in the observed radiance is only due to geometrical factors. That is, it is assumed that the atmospheric state is uniform and material properties are nearly homogeneous, for at least a subset of pixels in the scene.

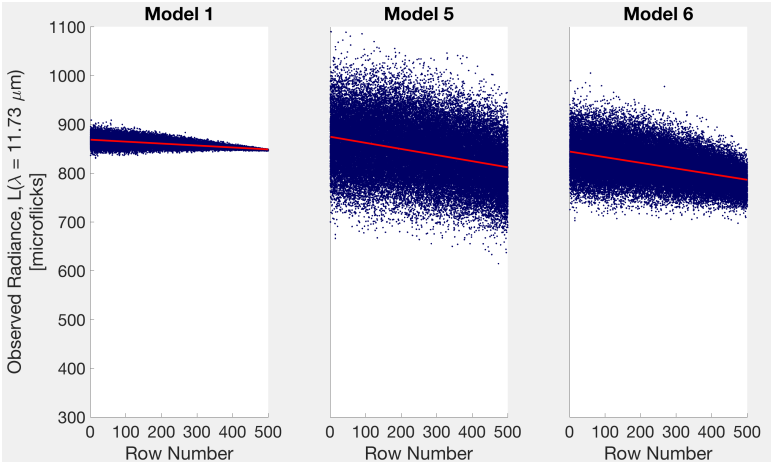

Figure 30. Observed radiance at 11.73 μm as a function of row number for three different MODTRAN model atmospheres. All scenes contain blackbodies at 300±5 K with zero noise.

For increasing path lengths and a fixed atmospheric state, transmission and path radiance will monotonically decrease and increase, respectively. Incorporating this explicit range-dependence into Eq. 10, results in

$$L(r, \lambda) = \tau(r, \lambda) L_g(\lambda) + L_p(r, \lambda). \tag{30}$$

Solving for the ground-leaving radiance by bringing all range-dependent quantities to the same side of the equation, gives

$$L_g(\lambda) = \frac{L(r, \lambda) - L_p(r, \lambda)}{\tau(r, \lambda)}. \tag{31}$$

This procedure provides a way to detrend the observed radiance. Fig. 31 shows one of the previous scenes both before and after detrending. One may see that the range-dependence of the observed radiance is removed when it is detrended with the correct atmospheric state; however, a means of quantifying an atmospheric state's ability to detrend the radiance is still needed. Without one, an identification of the atmospheric state which detrends the radiance best cannot be distinguished.

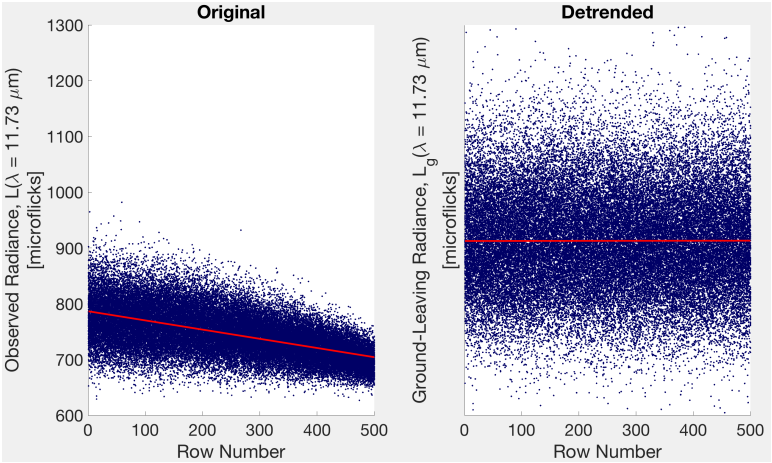

Figure 31. Shown for a Model 6 atmosphere at 11.73 μm, when the correct range-dependent transmission and path radiance are used on the observed radiance (left), the data is completely detrended (right).

Slope as Metric.

The observed radiance may have high order, non-linear curvature, depending on geometrical, atmospheric, and material factors. Regardless of its precise form, if this range-dependence only arises from changing geometrical factors and this geometry is known, then when the correct atmospheric state is modeled and applied, the detrended radiance will exhibit no slope or curvature; it will be completely removed.

The metric chosen to determine whether the atmosphere has been properly selected was the absolute value of the slope of the detrended radiance; the atmosphere which minimizes this quantity is best. The slope was chosen as the metric because it is able to quantify range-dependence of the detrended radiance and, more importantly, because the uncertainty in calculating this term is small enough such that the correct atmospheric state may be properly selected. To explore this choice further, results from using a linear fit with a quadratic one are contrasted.

A scene is generated with an observation geometry matching synthetic scenes described in 3.4, forward-modeling 500 rows and 200 columns of graybodies ($\varepsilon = 0.5$) at 300 ± 5 K with an atmospheric state defined by a ground air temperature of 288 K and water concentration of 7800 ppmv and then adding one microflick of noise. Focusing on the 8.20μm spectral channel and using a variety of atmospheric states, the scene is detrended via Eq. 31 and then fit either a linear or quadratic polynomial. The top of Fig. 32 shows values of the slope for the linear fit of the detrended scene, while the bottom two subfigures show the values of the linear and quadratic terms for the quadratic fit. The correct atmospheric state is identified by a white square, while a red dot labels the atmospheric state which minimized the given fit term. For this scenario, it may be seen that the minimization of the linear fit correctly identifies the atmospheric state, while both quadratic terms suggest a different atmospheric state.

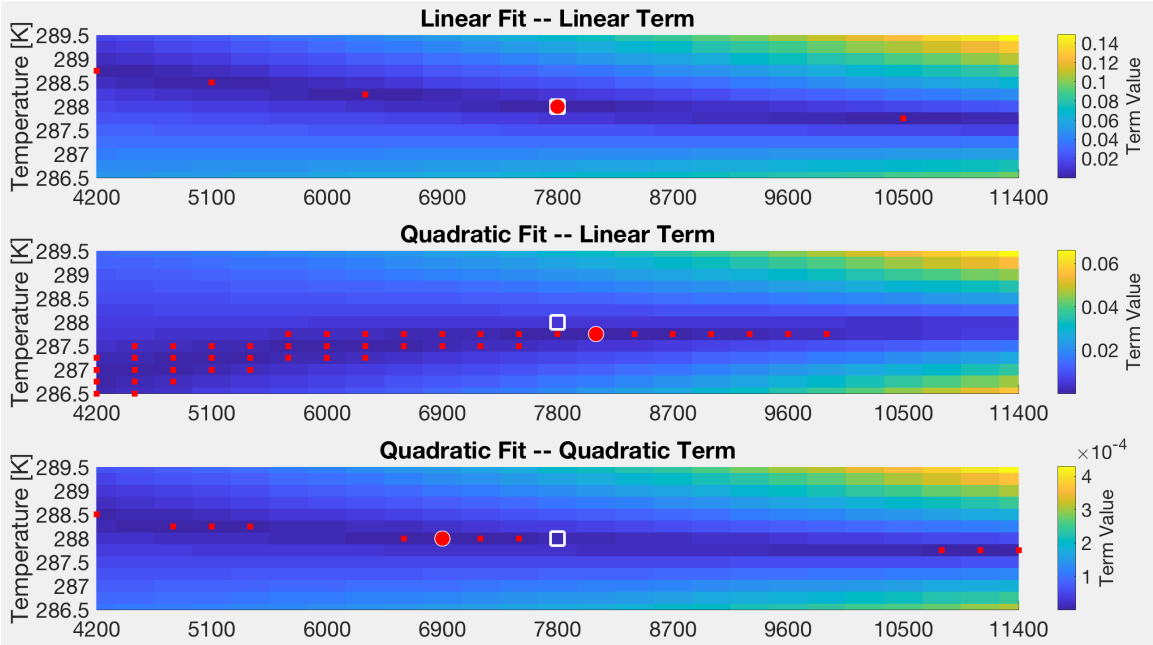

Figure 32. Radiance detrending results for Model 6 scene at 8.20 μm using various fit parameters. From top to bottom, fit terms include slope from linear fit, linear term from quadratic fit, quadratic term from quadratic fit. The white square represents the true modeled atmosphere, while the atmospheric state which minimized the given fit term is identified by a red circle. Red squares identify atmospheric states within the fit uncertainty of the best matched atmosphere (i.e. the red circle).

To identify one cause for the failure of the quadratic fit, the uncertainty in the fit terms with their values may be compared. The small red squares in Fig. 32 identify atmospheric states within the fit uncertainty of the best matched atmosphere (i.e. the red circle). One may see that the uncertainty in the linear fit, relative to the smallest fit values, is small; there were four atmospheric states (i.e. red squares) that were identified as having slopes smaller than the uncertainty in the slope. On the other hand, both quadratic fit terms had a larger relative uncertainty, and many different atmospheric states fell within the uncertainty.

This initial analysis suggest that adding subsequent fitting terms leads to higher uncertainty in selection of atmospheric state and reduced performance. As higher order terms are added, the fitting algorithm has more choices to consider when determining which fit parameters best characterize the observed trend in the data, leading to larger relative uncertainty for each term. Because of the factors explored here, only the slope from a linear fit is utilized. This analysis also suggests that to precisely identify the correct atmospheric state, this slope needs to be known with sufficient certainty. Factors which influence this uncertainty are explored next.

Slope Uncertainty as Limitation.

Understanding and reducing the uncertainty in the slope, the metric used to identify the correct atmospheric state, is necessary for proper atmospheric compensation. To understand the factors which drive uncertainty in the slope, the sources of variance in the ground-leaving radiance after it has been propagated through the atmosphere will be explored using the tools of uncertainty analysis. After doing so, methods of reducing this variance may be devised in order that the correct atmospheric state may be identified.

One motivation behind exploring factors influencing uncertainty in the slope was

the analysis of scenes with multiple material types. The complexity of the previous scenes from Fig. 30 was increased by adding a mixture of $\varepsilon = 0.5$ graybodies along with the blackbodies. From Fig. 33 it may be seen that the slope is not only affected by the known geometry and unknown atmosphere, but that scene composition also affects the slope of the observed radiance. If the scene has a non-uniform distribution of materials (i.e. any real-world scene), this impact is especially important and will be discussed in 4.1. A second effect of variable scene composition is on the uncertainty of the slope. For the center subfigure in Fig. 33, the fit of both the blackbodies and graybodies (i.e. the red line) has a slope and uncertainty of -0.072±0.006, while the blackbodies by themselves have a fit of -0.129±0.003 and the graybodies have a fit of -0.019±0.001. One may observe that the uncertainty in the fit for a single material class is smaller than for the combined group of materials. Variable materials are just one factor influencing uncertainty in the slope; this factor and others were explored by analyzing the model for ground-leaving radiance.

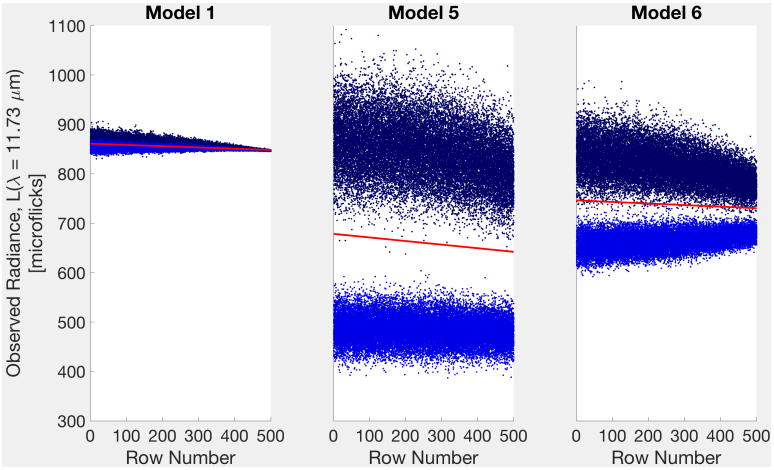

Figure 33. Observed radiance at 11.73 μm as a function of row number for three different MODTRAN model atmospheres. All scenes contain a mixture of $\varepsilon = 0.5$ graybodies (light blue) and blackbodies (dark blue) at 300±5 K with zero noise.

Uncertainty propagation of the ground-leaving radiance from Eq. 9 provides the clearest insight into factors leading to uncertainty in the slope fitting procedure. From

standard uncertainty analysis, the variance in ground-leaving radiance follows

$$\delta L_g(\lambda) = \sqrt{[(B - L_d)\delta\varepsilon]^2 + [(1-\varepsilon)\delta L_d]^2 + [\varepsilon\delta B]^2}, \tag{32}$$

where

$$\begin{aligned} \delta B &= \sqrt{\left[\frac{\partial B}{\partial T}\delta T\right]^2} \\ &= \frac{|\frac{2h^2c^3}{\lambda^6 k}\exp\frac{hc}{\lambda kT}|}{[T(\exp\frac{hc}{\lambda kT}-1)]^2}\delta T. \end{aligned} \tag{33}$$

The three components of Eq. 32 highlight the impact from variations in materials, reflections, and emissions respectively. It is important to note that all terms have an implicit wavelength dependence which should be considered.

The first component predicts that variance in ground-leaving radiance is partially caused by variations in material emissivity. This observation inspired classification of pixels into different material classes for analysis as discussed below in 4.1. One may see that this first term is scaled by the difference between atmospheric downwelling and blackbody radiation from the objects in the scene. Thus, the importance of dividing a scene into different emissivity classes becomes more significant if the objects are at significantly different temperatures than the atmosphere, highlighted especially at shorter wavelengths.

The second component shows that variations in downwelling radiance need to be small, especially for more reflective materials whose signals may be mostly due to reflected downwelling. As an additional consideration, reflective materials tend to behave more specularly. This specular behavior violates the original model assumptions of Lambertian targets and would tend to increase variation in downwelling radiation, particularly if the reflective materials have surface normals oriented towards different regions of the sky. The impact from reflective materials and variable downwelling will

be a final consideration, explored further in 4.3 and 4.3.

This third component depends on blackbody emissions and is more significant for more blackbody-like materials. This final term suggests difficulty in determining the correct atmosphere even for a scene composed of a single material, as temperature differences throughout even a single material class are expected to exist and may be potentially large. As absorption and emission of radiation are correlated, if a high emissivity material also has high emissivity in the visible and SWIR spectral regions, the material could have both large solar loading and large temperature variability from possible shadows and obstruction in the scene. The impacts of larger temperatures are shown in Fig. 34 where the Planck term from Eq. 33 is explicitly shown for various temperatures and wavelengths. The least variation occurs for the longest wavelengths and coolest temperatures (bottom left corner of the figure). Although the wavelength dependence appears sizable, the wavelength dependence of material emissivities may offset this effect. Natural materials tend to have higher emissivities at longer wavelengths [14], which may reduce this effect.

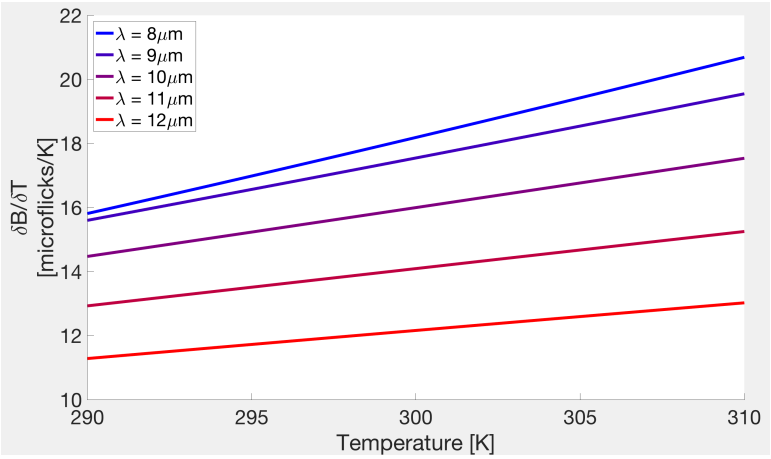

Figure 34. Uncertainty spread from the Planck blackbody term in Eq. 33. We notice smaller uncertainties at longer wavelengths (bottom) and cooler temperatures (left).

The impact of all of these considerations will now be explored using a synthetic

dataset similar to the ones in 3.4 except that the declination angle from the horizon has been increased to 23 degrees, the observation altitude has been decreased to 0.25 km, the iFOV has been decreased to 390 microradians, and number of row pixels has been increased to 2000. The total range coverage extends from about 0.3-175 km. These specific viewing conditions were chosen to explore the full range variation of the ground-leaving radiance, so that the entire signal from the ground would be absorbed by the atmospheric path at the furthest range. The transmission and path radiance for a Model 2 atmosphere with this viewing geometry for both a short wavelength spectral channel at 10.1 μm (blue) and a long wavelength spectral channel at 12.1 μm (red) are shown in Fig. 35. One may see that for this geometry, the transmission reaches zero and path radiance reaches a maximum at final row. The less transmissive 12.1 μm band also tends to have a larger path radiance, except for at the furthest range. At this last row, the path radiance for the 10.1 μm spectral channel is larger.

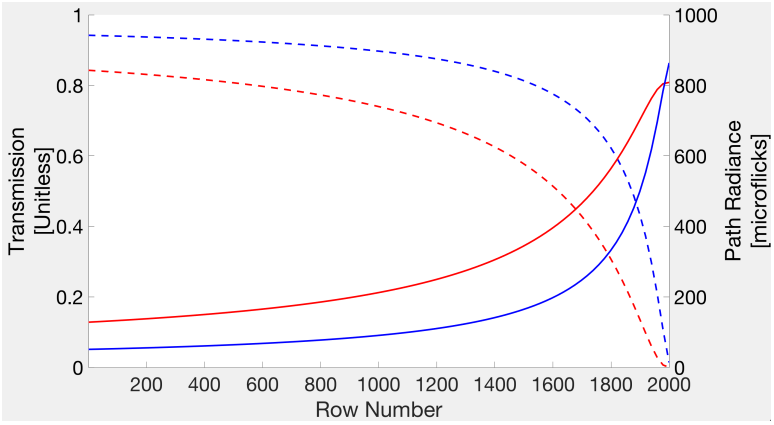

Figure 35. Transmission (dashed) and path radiance (solid) for a Model 2 atmosphere at various ranges. A longer (red, 12.1 μm) and shorter (blue, 10.1 μm) wavelength channel are considered.

Using these transmissions and path radiances, the radiances of blackbody and graybody ($\varepsilon = 0.2$) objects at 300$\pm$2 K were forward-modeled at the two wavelengths. The left side of Fig. 36 displays the expected trends and behavior, showing

the observed radiance before correction. Looking at the overall trend of observed radiance for the two materials, the radiance from the blackbody decreases down towards path radiance since the blackbody radiance is larger than the path radiance. The radiance from the graybody increases up towards the path radiance because the downwelling radiance term is less than the path radiance. Referring back to the discussion in 2.2, the integrated downwelling radiance is a combination of atmospheric contributions from short line-of-sight paths at nadir and long line-of-sight paths towards the horizon. These longer atmospheric paths will have more sizable emissions. Since the path radiance is due to emissions from this longer atmospheric path alone, it will be larger than the downwelling radiance. At the further ranges, it is expected that transmission will tend towards zero and that the only radiance observed for both graybodies and blackbodies is that from the atmospheric path via Eq. 30. The path radiances from the furthest distance were converted to brightness temperatures via Eq. 16.

In the center of the Fig. 36, blackbody curves for these brightness temperatures are shown, where the dots mark the spectral channels. The vertical separation of these two dots is equal to the separation between the two path radiances on the left plot. These two wavelengths were chosen to show that this separation is largely due to spectral location on the blackbody curves, as the effective blackbody temperatures are nearly the same. In this center plot, the downwelling radiation as well as radiance from a 300 K blackbody are shown; the difference between these two in a given spectral channel determines the variation in radiance between different materials in the left figure (e.g. the blue points are more separated than the red ones because there is a larger radiance difference between a 300 K blackbody and the downwelling in that particular spectral channel). Using the correct atmospheric state, the observed radiance from the left was detrended into the ground-leaving radiance shown right.

Note that regardless of the material or wavelength band, all groups were successfully detrended.

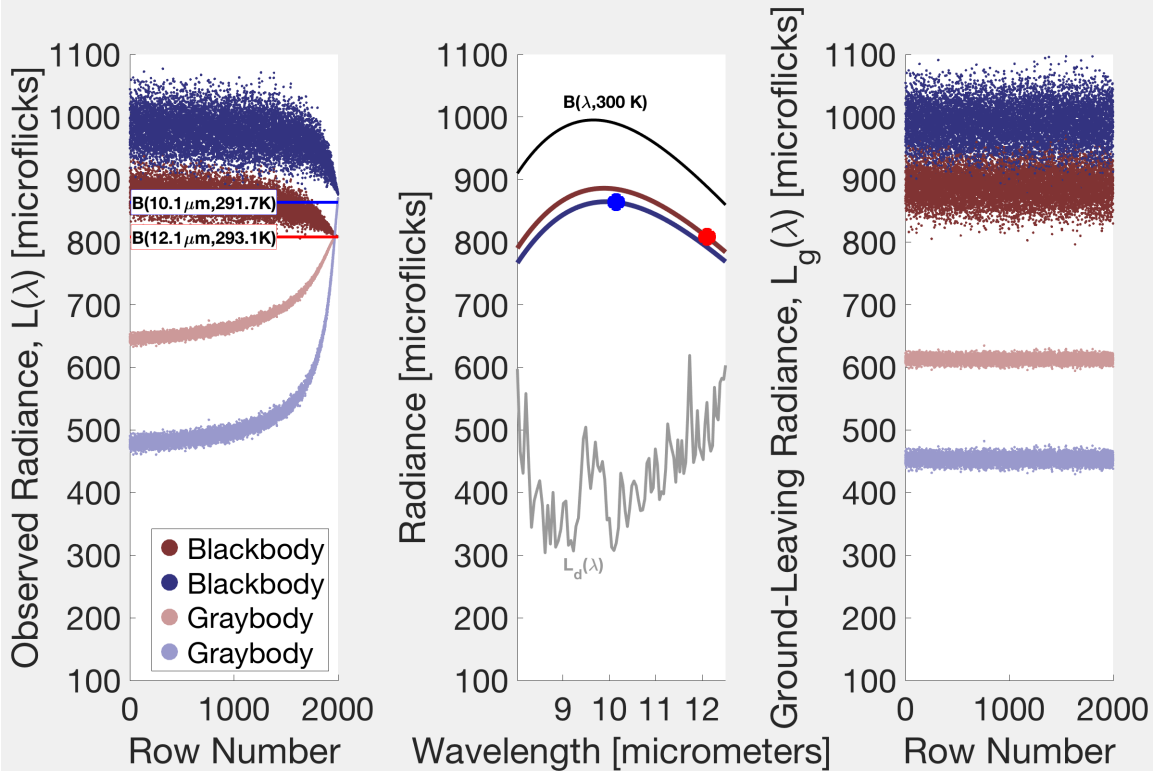

Figure 36. Left: Observed radiances with respect to range for 300 K blackbody (dark) and $\varepsilon = 0.2$ graybody at short wavelength (blue) and long wavelength (red). Center: From top to bottom, 300 K blackbody curve, blackbody curves for path radiance brightness temperature at two different wavelengths, downwelling radiance. Right: Detrended radiances.

These observations and others will now be related back to the mathematical theory. Focusing on the two groups of red points, the two different materials are distinctly separated because of the very different emissivities; however, had $(B - L_d)$ the been reduced, e.g. by considering lower object temperatures, then this difference due to emissivity variations would not be as evident, according to the first component of Eq. 32. The ground-radiance for a lower temperature (260 K) case is shown in Fig. 37, and it may be seen that the different materials are closer together when the blackbody

and downwelling radiances are more similar. Comparing Fig. 36 and Fig. 37 with each other, one can also see that lower temperatures have smaller variances within individual groups. Additionally, longer wavelength bands (the red pixels) have smaller variances than their blue counterparts. These were both predicted via Eq. 33 and the corresponding Fig. 34. The temperature variance throughout the scene, δT, was not explored as its impact is more intuitive (i.e. a larger variation of temperatures will have a larger variance of radiances, particularly for blackbodies). From Eq. 32, the third component also predicted that lower emissivity materials has smaller variances, which is evident in Fig. 36. Though the second component of Eq. 32 has not been considered here, as the starting assumption for both OISAC and RD had been for cases where $\delta L_d = 0$, impacts from variable downwelling will be explored at the end in 4.3. Last, though the impact of Gaussian-distributed sensor noise has not been included, one may observe in the preceding figures that 1 microflick of noise is relatively small compared to variations from differing temperatures or materials, which can impact the observed radiances by hundreds of microflicks.

The entire discussion here highlights sources of uncertainty in determining whether one atmosphere or another better detrends the observed radiance. Significant variation in ground-leaving radiance has been observed, most notably from different emissivities throughout a scene. Since scenes are not expected to have a uniform distribution of materials, this presents a problem that needs to be addressed if one hopes to perform atmospheric compensation with any degree of certainty. This observation leads to separating a scene into various classes before detrending.

Additionally, it has been noticed that dissimilar material properties lead to larger and smaller amounts of δL_g. For this case where $\delta L_d = 0$, highly reflective materials have lower ε and may have smaller T and δT, all of which influence the third component of Eq. 32 and result in smaller δL_g. Thus, for these cases, it is actually preferable

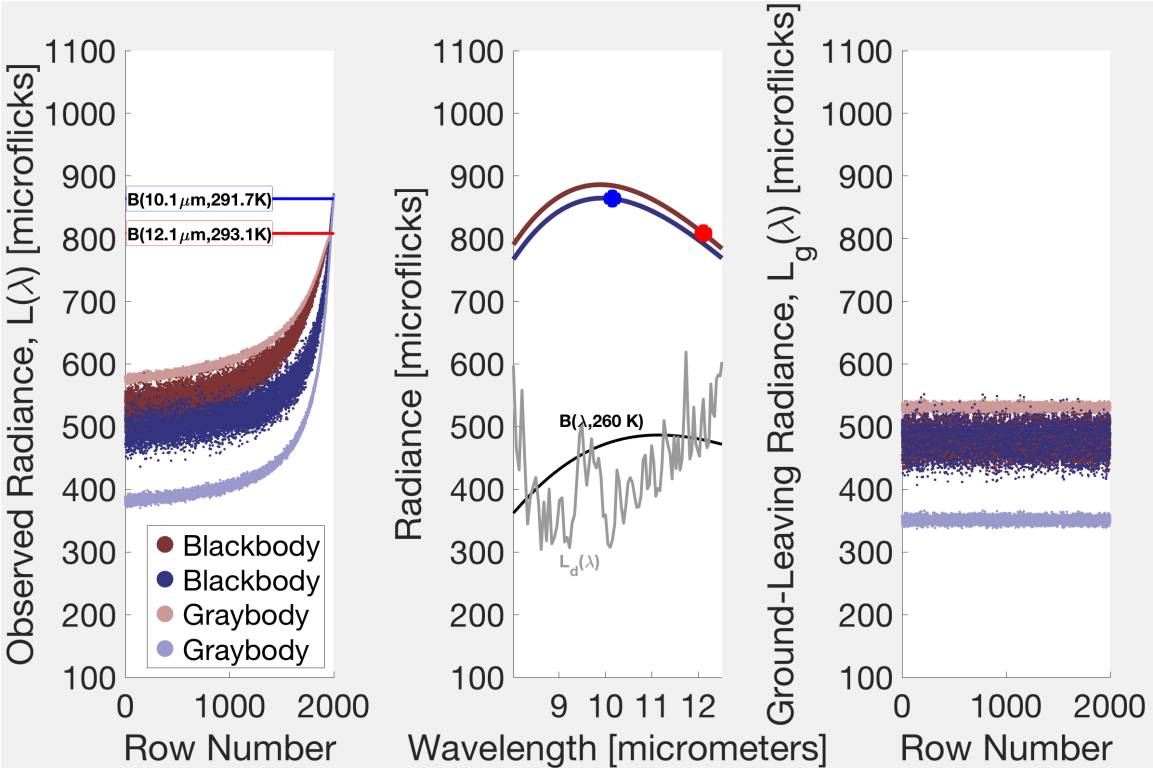

Figure 37. Left: Observed radiances with respect to range for 260 K blackbody (dark) and $\varepsilon = 0.2$ graybody at short wavelength (blue) and long wavelength (red). Center: From top to bottom, 260 K blackbody curve, blackbody curves for path radiance brightness temperature at two different wavelengths, downwelling radiance. Right: Detrended radiances.

to use highly reflective materials for the compensation, all else being equal. However, for more general cases, because different classes of materials perform differently, this observation leads us to weighting results of the different material classes as discussed in 4.1. Likewise, different wavelength bands have also demonstrated distinct variances in L_g; because of this, the class weighting will be performed spectrally.

This first adjustment that will enable us to improve the radiance detrending process, class separation, is be discussed next. Then, its application to a more complex scene will be observed before finally introducing the RD error metric which will incorporate weighting of the different material classes and wavelengths.

K-means for Material Classification.

From the above discussion, the need to separate the scene into different classes to improve the ability to determine whether the scene has been properly detrended is apparent. K-means clustering is a common technique that provides a way to separate a scene into different classes, where the radiance detrending process may be performed for each class. Clustering reduces the variability in the emissivity signature. This leads to a reduction in the variability of the scene radiance and, in turn, a smaller uncertainty in the slope of the detrended radiance. This is a necessary first step of the RD technique, and it will be seen that this will ultimately lead to an iterative scheme for RD, whereby previous RD iterations will improve material classification, leading to better atmospheric estimates.

There are difficulties which arise when using k-means to identify different material classes in an oblique scene. Unfortunately, performing k-means clustering on an oblique scene may not properly separate materials as effectively as in a nadir scene, since transmission and path radiance differences throughout the scene distort ground-leaving radiances by varying amounts. Without modification to the pixel signals fed

into k-means, this clustering process will less effectively separate materials into their true classes.

One modification that was explored to overcome this clustering challenge involved an initial estimate of the scene's transmission. This transmission could be approximated using an unscaled ISAC approach or previous RD iteration. By performing k-means of the observed radiance using only the most transmissive bands rather than all wavelengths, more effective class separation can be achieved. Since low atmospheric transmission can conceal material properties, using only those spectral channels which allowed for larger signals can lead to improved classification.

A second modification may be made if one has a reliable estimate of the range-dependent atmospheric transmission and path radiance. For the RD technique, this estimate came from the first RD iteration, though OISAC may also provide this estimate. Using this estimated transmission and path radiance, the ground-leaving radiance for each pixel may be approximated via Eq. 31. By using accurate estimates of the ground-leaving radiance rather than observed radiance in the clustering process, the spectral distortion from the variable atmospheric path may be reduced. Reducing the impact due to varying geometry results in improved material classification for later iterations of RD. The ability to reduce this impact depends on the atmospheric state used to compensate and solve for this ground-leaving radiance, and if a poor choice is made, extra range dependence could instead be imparted to the scene from over-compensation. RD has shown its best performance when performed in an iterative process, whereby earlier estimates of the atmosphere are used to improve material classification, leading to better atmospheric estimates.

The application of k-means clustering to a synthetic scene of five materials (water, brown loam, anhydrite, roof slate, and limestone) that had been segmented into five 500 pixel-long by 20 pixel-wide segments was performed. Materials in the scene

had temperatures of 300 ± 5 K, and the scene geometry and atmospheric conditions were identical to the Model 2 scene described in 3.4, including 1 microflick of at-sensor noise. The results are shown in Fig. 38. The first subfigure shows the true material classes throughout the image. The second subfigure shows results of k-means application to the observed radiance; k-means was applied using the cosine distance metric, five clusters, and 50 replicates to avoid local clustering minima. One may see that the range variation throughout the scene has caused some material classes to be grouped into segments based on range rather than material. This leads to two problems. Not only does this separate pixels into classes of dissimilar emissivities, but if one were to perform RD on an individual class, then the number of rows used has been greatly reduced. Since the differences between rows ultimately contains the geometrical variation used to identify the correct atmospheric state, if a material class is not present throughout a significant number of rows in the scene, it would have a larger uncertainty. The third subimage shows the impact of using only the most transmissive bands of the observed radiance. While it still shows significant segmentation based on range, it has improved performance in correctly separating the different material classes. Since it has materials with good clustering throughout most of the range of the scene, this will lead to an improved first iteration of RD. The final subimage shows k-means application on the most transmissive bands of the ground-leaving radiance, where the atmospheric state used to solve for L_g was chosen as the atmosphere from the first iteration of RD for the Model 2 atmosphere shown in Table 5). These results highlight that material classification is more difficult for an oblique scene and that there are also methods to improve classification; these techniques ultimately give RD the ability to properly compensate for the atmosphere.

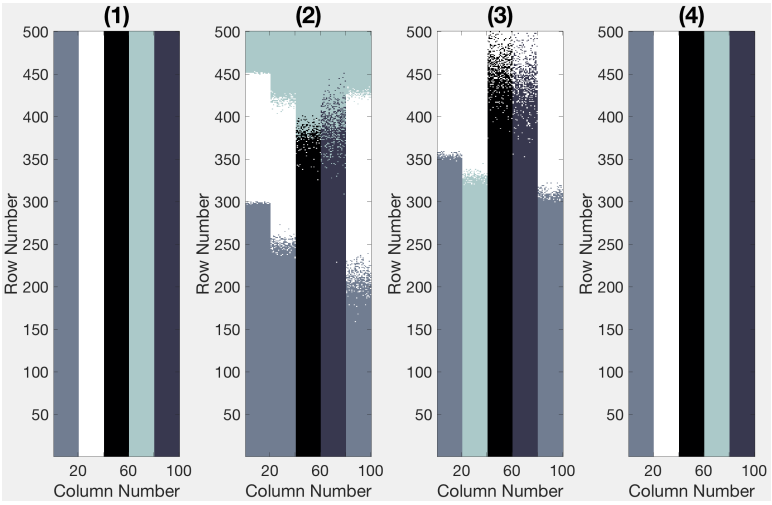

Figure 38. Example of k-means clustering on a synthetic scene of five different materials that had an identical observation geometry and atmospheric state as the Model 2 scene in 3.4. Truth is shown on the left (1), while the rest demonstrate clustering using observed radiance (2), using the most transmissive bands of observed radiance (3), and using the most transmissive bands of ground radiance using the atmospheric state determined by the first iteration of RD on the Model 2 scene (introduced later in Table 5). From these middle two subfigures, we see that k-means may mistakenly classify pixels based on range rather than material properties; we also see that there are methods to reduce this classification error.

Structured Scenes.

Up until now, the focus has been entirely on scenes composed of materials uniformly mixed throughout. Such scenes are unrealistic and also theoretically easier for RD to handle, as they provide data for every row of the scene which decreases uncertainty in the radiance's trend. Realistic scenes on the other hand tend to have a more structured distribution of materials. Like materials, temperatures also tend to be distributed non-uniformly throughout a scene. Since a material's ability to absorb radiation depends on its emissivity, the temperature distribution throughout a scene will most likely depend on the distribution of the scene's materials. To more thoroughly test the RD algorithm, two new synthetic scenes were generated which more accurately represent real-world imagery. These synthetic scenes were based on the Mako geometry and estimations of material and temperature distributions within the Mako dataset.

Structured Scene Generation.

First, the Mako scene was broken into eight material classes by using k-means clustering of the ground-radiance from Eq. 31 and OISAC's transmission and path radiance estimates. With the scene divided into classes, a unique emissivity is then assigned to each class. The emissivities, materials, and pixel locations are shown in Fig. 39. When assigning the emissivities, the materials were attempted to be realistically matched, e.g. concrete and asphalt were assigned to more widely distributed classes while aluminum was not. For the scene temperatures, the estimated pixel temperatures from OISAC's TES results were used to assign a mean temperature and standard deviation for each material class and then normally distributed those temperatures throughout each class individually. OISAC TES temperatures were chosen because Segmented ISAC and FLAASH-IR had evident non-physical range

variations of temperature. The mean temperature and standard deviation for each material class are shown above the pixel locations in Fig. 39.

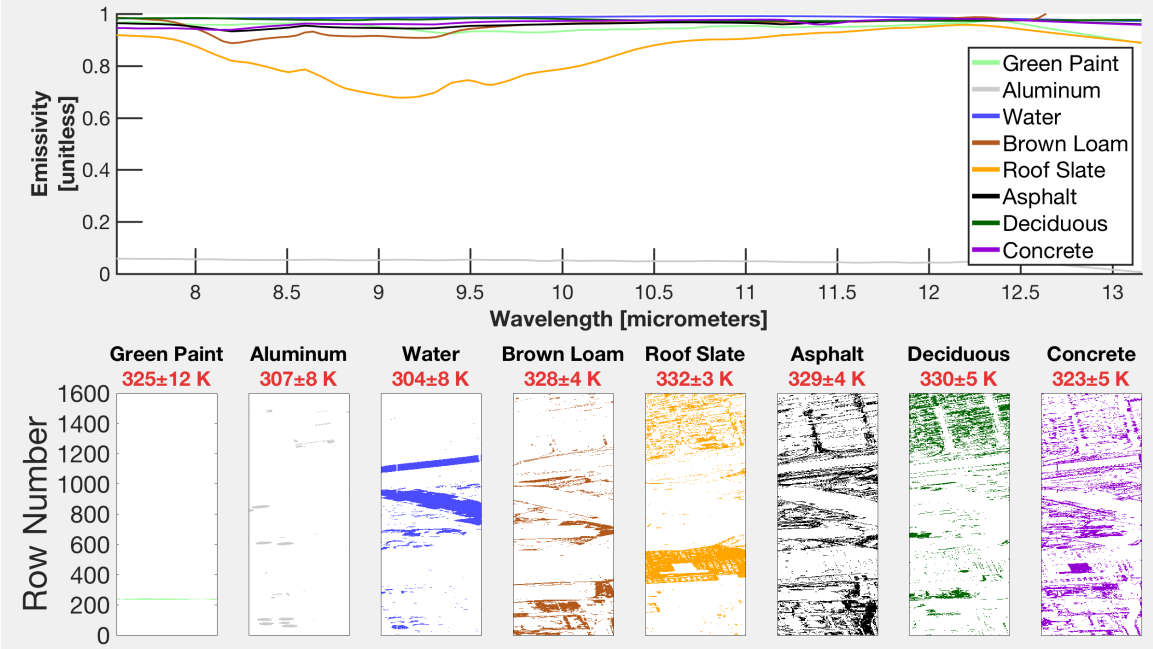

Figure 39. Emissivities of the materials used in the non-uniform synthetic scenes are shown above. Their locations within the scenes and temperatures are shown below.

Finally, a ground air temperature and water concentration were used to characterize the atmospheric state, just as had been used throughout this research. The temperature was chosen to be 310 K, slightly cooler than the average temperature of materials in the scene. Two different water concentrations were chosen, 7800 ppmv to represent an atmospheric state similar to the Model 6 atmosphere and 18300 ppmv to represent the Model 2 atmosphere. These atmospheric states were propagated through the Mako observation geometry (see 3.4) using MODTRAN, and after forward-modeling the observed radiance via Eq. 10, one microflick of Gaussian distributed noise was added to the resulting radiance. These scenes will subsequently be referred to as Structured 2 and Structured 6, since their atmospheric states are based on a variation of the Model 2 and Model 6 atmospheric states.

Detrending the Structured Scenes.

From the Structured 2 scene, an example of the detrending process on a material with non-uniform distribution throughout the scene is captured in Fig. 40. The bottom of the figure shows pixel locations for the material class of interest. The top of the figure shows radiances across the scene using density-weighted scatter plots, where the colors represents the number of points at a particular radiance and row number. Because of the sheer number of pixels in the scene, this provides a means of visualizing how the trend-line was fit to the data. On the top left, one may see that the observed radiance has an apparent negative slope to it. The top middle shows the ground-leaving radiance after an improper atmosphere has been used to detrend. Finally, the top right image shows the result when the correct atmosphere has been used.

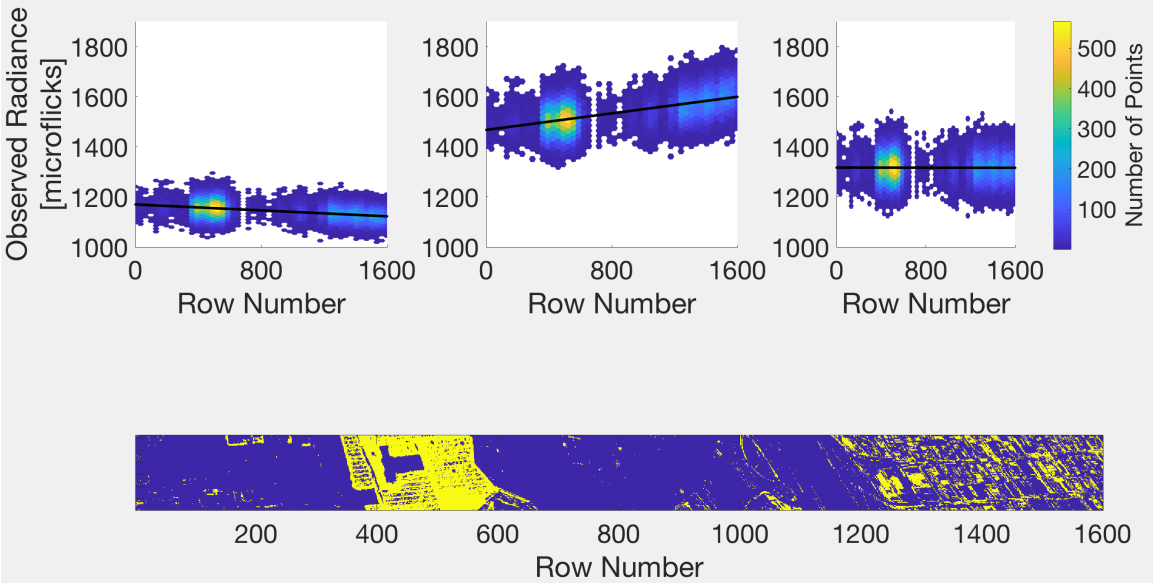

Figure 40. Example of the radiance detrending process on the non-uniform scene. Top: left shows the observed radiance at 11.73 micrometers, middle shows the ground-leaving radiance when an improper atmosphere is used to detrend, right shows the ground-leaving radiance when the correct atmosphere is used. Bottom: shows pixel locations for the current material class.

One may see that this process is almost identical to that for the randomly uniform distribution; the key is in proper classification of image pixels. The additional challenge for these new scenes is that pixels will most likely no longer be present at each row of the image. This is expected to increase the uncertainty in the slope of the detrended scene radiance, thereby increasing the uncertainty in identifying the correct atmosphere.

In an effort to demonstrate the difficulty in accurate atmospheric identification for these realistically structured scenes, the detrending process was applied to the Structured 6 scene solely using the 11.73 μm water band and without using k-means clustering. The Structured 6 scene was generated using a ground air temperature of 310 K and water concentration of 7800 ppmv; however, after detrending with a numerous atmospheric states of varying temperatures and water concentrations, the atmospheric state which best detrended the Structured 6 scene had a temperature of 309.5 K and a water concentration of only 3600 ppmv, suggesting less than half the actual water concentration. As demonstrated later in 4.3, this scene may be accurately compensated if one incorporates data from additional spectral bands and utilizes material clustering.

RD Metric.

With the scene now divided among distinct classes, the observed radiance for each class and for each spectral band may be detrended. Due to the inherent uncertainty in the detrending process, from sources such as sensor noise and large variances in ground-leaving radiance, the atmospheric state which detrends the scene radiance best will likely be different for the different wavelengths and materials. The performance of any given atmospheric state (T_0,C_0) is characterized by its ability to detrend the observed radiance for all material classes, k, and all wavelength bands, K, of interest.

For any given material class and wavelength, the slope of the detrended radiance, m, weighted by its uncertainty, δm, is summed together with the results from the other material classes and wavelengths. Thus, a surface defined by

$$z(T_0, C_0) = \sum_{k,K} \frac{|m(T_0, C_0)|}{\delta m(T_0, C_0)}. \tag{34}$$

By weighting the resulting slopes by their uncertainty, those combinations of spectral bands and material classes with the lowest variance of ground-leaving radiances will be weighted more significantly; those with greater uncertainty will not be weighted as heavily. The $\frac{|m|}{\delta m}$ term could have been raised to higher order power, e.g. $(\frac{m}{\delta m})^2$; however, the expression used is expected to be more robust and less sensitive to outliers which may exist in the data. Initial testing has shown the first metric to be slightly better but both have yielded similar results.

Application of this metric across *all* wavelength bands was sufficient for some of the synthetic scenes used in this study; however, using all wavelength bands did not always lead to correct atmospheric identification for all of the synthetic scenes unless the precise material classes were also provided. If the materials had not been clustered into their proper classes, an realistic expectation for most scenarios, then the radiance detrending process was prone to difficulties, suggesting that the metric needed to be revised.

It was found that one method of improving the metric's robustness is to utilize only the least transmissive spectral bands. Earlier during the k-means clustering, a classification of materials was desired; the emissions and reflections from the materials on the ground were the signals while the atmosphere interfered as noise. Classification was improved by using the most transmissive bands of the ground-corrected radiance, as both modifications reduced atmospheric impact. In the current situation where the goal is now to determine which atmospheric state detrends the scene best, the

atmosphere is the signal, and the variability in ground-leaving radiance described in Eq. 32 represents the noise. Focusing on the least transmissive spectral bands suppresses noise from variability in ground-leaving radiance and boosts the atmospheric signal. This modification not only improves algorithm performance but also greatly reduces its computational cost.

Fig. 41 contrasts the detrending process for low and high transmissive bands of the Structured 2 scene for the same material class shown in Fig. 40. The center of Fig. 41 shows the two spectral bands used, 7.66 μm in blue and 10.06 μm in red. Radiance images of the low transmissive and high transmissive bands are shown on the left and right of the figure, respectively. For the low transmission band, there is an evident radiance gradient across the image. This drop in radiance across the scene is not due to vastly different temperatures or scene materials at the further range but is entirely due to variable path lengths. Alternatively, the radiance image for the high transmission band shows very little variation due to changing geometry. Contrasting these two, the scene with larger variability has a stronger atmospheric signal that can be used in the detrending process. In the top and bottom of the same figure, an example of an incorrect atmosphere being used to detrend one of the material classes is shown. Since the atmospheric state used did not have sufficient humidity, the bottom plot shows that the radiance gradient is still evident for the low transmission scene. For the higher transmission band at the top of the figure, the radiance gradient is more difficult to discern. Graphically, this top case appears worse than it truly is because the radiance takes on a larger range of values; however, a numerical comparison of the resulting slopes confirms that the bottom case has more than twice the slope of the top. For the reasons discussed here, the RD algorithm will only utilize these less transmissive bands when detrending.

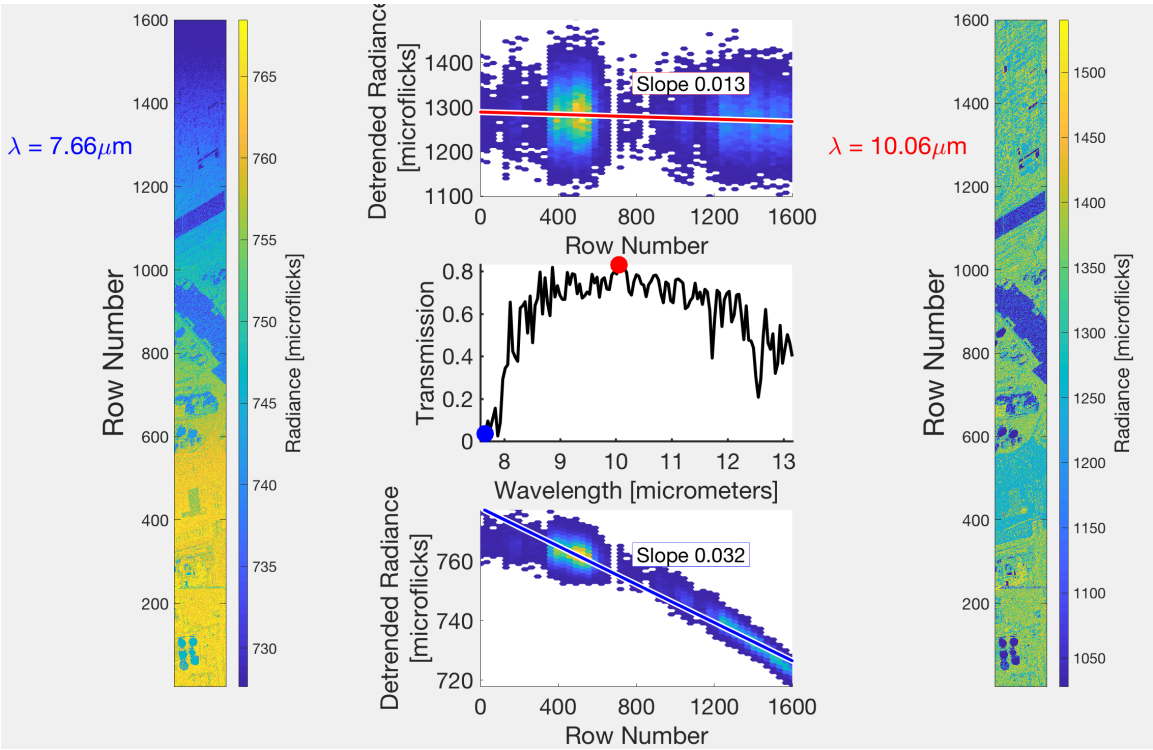

Figure 41. Contrast of the detrending process for low and high transmissive bands of the Structured 2 scene. Radiance images for the two spectral channels are shown on the left and right. Top and bottom demonstrate the resulting slope when detrending with an incorrect atmosphere. This analysis demonstrates that the larger atmospheric signal in lower transmission bands aid the detrending process.

4.2 RD Implementation

Implementation of the RD algorithm may be broken down into two main processes, done iteratively.

1. **Clustering** Separate scene pixels into different groups using k-means clustering of the most transmissive wavelength bands.

2. **Detrending** Determine which atmospheric state best minimizes the error metric using different material classes and the least transmissive wavelength bands.

The flowchart for the RD algorithm is summarized in Fig. 42. Next, the two processes are described, highlighting how they were performed and the inputs/outputs for each one.

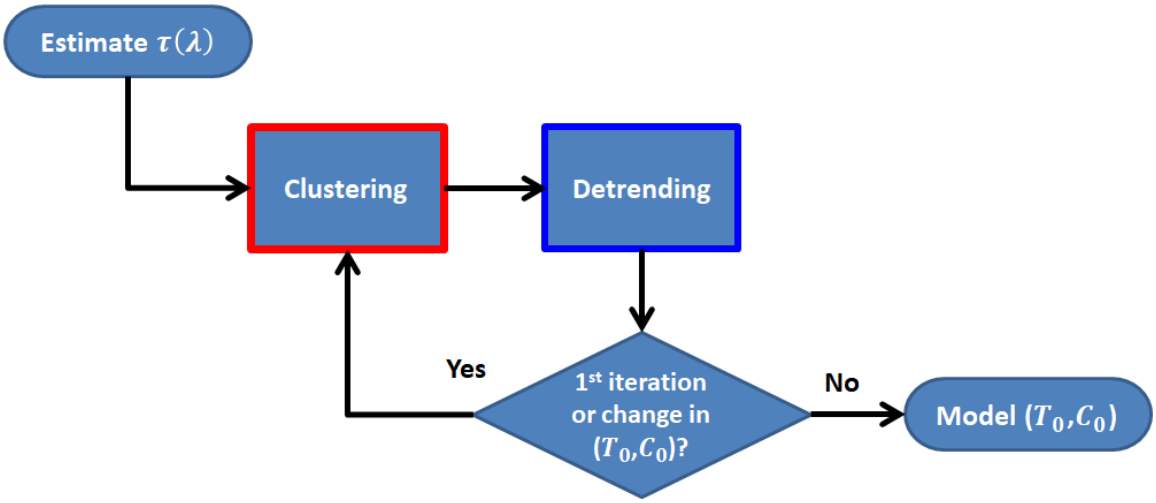

Figure 42. Flowchart showing the RD process.

Clustering.

The first process is clustering. Before the observed radiance can be detrended, the scene needs to be clustered into different material classes. This involves performing

k-means clustering on the most transmissive bands of the ground-leaving radiance. For the first iteration of the algorithm, the transmission spectrum needs to be estimated to determine the most and least transmissive spectral bands. Since only the relations between the various spectral transmission values are important, the standard, unscaled ISAC algorithm was chosen to provide this estimate. Additionally, without range-varying transmission and path radiance estimates for this first iteration, k-means clustering is instead performed on the observed scene radiance rather than the ground-leaving radiance. Subsequent iterations use RD's best-detrending atmosphere to estimate ground-leaving radiance for superior class separation.

Regarding the k-means application itself, the scene was divided into ten different material classes. The k-means clustering process was applied using the cosine distance metric and with 50 replicates. Ten classes were chosen as a balance between separating the scene into enough classes to account for material variability while also having large enough classes such that most of the scene's range was spanned by the pixels in the individual classes. If too many material classes are chosen, then it's possible to mistakenly subdivide a single-material class into various subclasses that are instead based on range rather than composition.

The Structured 6 scene, which contained eight different material classes, was analyzed using varying numbers of k-means clusters. Analysis using anywhere from two to 20 k-means clusters showed no change in the identified atmospheric state at the final RD iteration, suggesting some degree of tolerance in the number of specified clusters. Clustering into any of these numbers of groups led to correct identification of the atmospheric state, though additional clusters led to increased processing time for both clustering and detrending as well as slower convergence to a final atmospheric state, requiring further iterations. The effectiveness of utilizing only two k-means clusters was initially surprising;, however, upon exploring this case further, several reasons

for its effectiveness were found. Clustering the scene into two materials effectively separated roof slate (which made up 19% of the scene) from the other seven materials. Of the seven materials, two of the most spectrally diverse materials (aluminum and green paint) only made up 2% of the total scene, while four of the materials (water, asphalt, deciduous, concrete) made up 67% of the scene and had very low spectral diversity, with an average spectral standard deviation of 0.013 ± 0.08 over the least transmissive bands. Because both clusters had a low variation in emissivity and both spanned much of the total range in the scene, the detrending process correctly identified (310 K, 7800 ppmv) as the atmospheric state. In the same study, application of k-means clustering using a single material (i.e. turning off clustering) resulted in identification of the (309.75 K, 6000 ppmv) state during the detrending process. This incorrect identification demonstrates the need for clustering to improve accuracy, as even two clusters were sufficient. Further testing and analysis is recommended to explore the relation between scene composition and ideal number of k-means classes.

To improve the accuracy of material classification, the k-means clustering was done using the most transmissive bands. From an unscaled ISAC estimation of the atmospheric transmission, the top quarter most transmissive wavelength bands were used, e.g. the 23 most transmissive out of the 94 wavelength bands for the synthetic scene. When selecting the most transmissive bands, the least transmissive bands are also selected for use in the detrending process. An example of the unscaled ISAC transmission as well as selected bands for the Mako scene is shown in Fig. 43. The most transmissive bands are marked in red, while least transmissive bands are marked in blue.

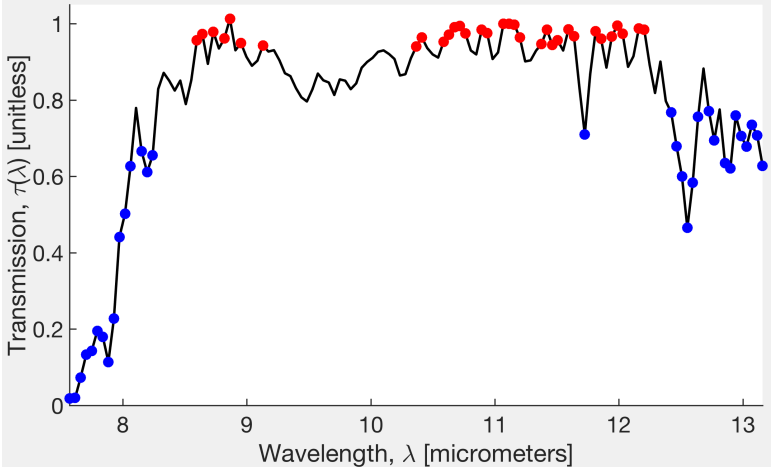

Figure 43. Results from standard, unscaled ISAC on the Mako scene, showing the most (red) and least (blue) transmissive bands used for the clustering and detrending steps, respectively.

Minimize RD metric.

Now that the scene has been broken down into different classes of materials, the second step is to find the atmospheric state which detrends each material class best using the least transmissive wavelengths. This corresponds to finding the minimum of the error surface described by the metric in Eq. 34. Only the bottom quarter least transmissive wavelength bands were used, e.g. the 23 least transmissive out of the 94 wavelength bands for the synthetic scene. The material classes used were also limited; only those classes which had data in at least half of the rows of the scene were used, e.g. material classes which were located in at least 250 different rows for the 500 row synthetic scene. Excluding material classes which had the least range-dependent information improved both performance and processing time.

Finding this minimum was done in an exhaustive manner, applying the detrending process to atmospheric states ranging from 270-315 K and from 300 to 30000 ppmv, with step sizes of 0.25 K and 300 ppmv to achieve a similar resolution as used in OISAC. This was done to explore both the behavior of the resulting sur-

face and whether local minima tended to exist; however, this manner of finding the minimum is not recommended for operational use as it is more time-consuming than necessary. Future minimization efforts could possibly further limit wavelength bands, atmospheric states, or materials to speed up the detrending process; however, the impact of these modifications are not the focus of the present study.

After the optimal atmospheric state has been selected, the atmospheric transmission, path radiance, and downwelling are immediately known since this atmosphere was already modeled in order to detrend the observed radiance in the first place. With this estimate of the atmospheric state, a subsequent iteration of RD is performed, beginning with a better estimate of the ground-leaving radiance to improve clustering.

This process is iterated until the resulting atmosphere begins to repeat. For all seven scenes analyzed in this study, the RD algorithm stabilized on an atmospheric state within 1-3 iterations. Convergence properties of RD were not explored, but they are recommended for future studies.

4.3 RD Results

Here the results of analyzing multiple scenes are explored and discussed. Not only are there the synthetic and Mako datasets discussed in 3.4 and the non-uniform scenes described in 4.1, but there are two new synthetic datasets meant to challenge OISAC and RD. These new scenes both lack blackbody pixels and one of them incorporates variable downwelling contributions. These new scenes will be discussed more in their respective sections.

In lieu of presenting transmission and path radiances for the first and last row for all seven scenes and material correlation and RMS results for dozens of materials across each scene, the focus will be on a few illustrative cases. To further summarize

the results and draw comparisons between RD and OISAC, Table 5 highlights the atmospheric state picked by the two techniques. As discussed in both the development of OISAC and now of RD, both techniques produce final transmission and path radiance spectra directly from a MODTRAN simulation. The input for this simulation is a temperature, water, and pressure profile, and following the lead of [46], the entire atmospheric state has been characterized with a single ground air temperature and water concentration, (T_0,C_0). Table 5 shows these two quantities as they were determined by OISAC and RD. The ground air temperature is in red; the ground water concentration is in blue. This details in this table will be discussed in the following sections.

	Truth	RD				OISAC
		*i*1	*i*2	*i*3	*i*4	
Model 2	≈ 295.25 18300	295.5 18000	295.5 18300	295.5 18300	--	295.25 18304
Model 6	≈ 288 7800	287.5 7500	288 7800	288 7800	--	288.25 7866
Structured 2	310 18300	310 18300	310 18300	--	--	309.75 17793
Structured 6	310 7800	310 7800	310 7800	--	--	309.75 7392
Mako	N/A	304.25 9000	304.25 9300	304.25 9300	--	304 7866
Reflective 6	≈ 288 7800	288.25 8100	288.5 7800	288 7800	288 7800	291.5 28775
Reflective 6, $\delta L_d \neq 0$	≈ 288 7800	286.75 6000	288 7500	288 7800	288 7800	290 28775

Table 5. True atmospheric state along with those atmospheric states identifed by RD (up to four iterations) and OISAC for all scenes analyzed. Ground temperature, T_0 (K), is in red, while ground water concentration, C_0 (ppmv), is in blue.

Original Model 2 and Model 6 Scenes.

Like OISAC, RD sufficiently compensated the original MODTRAN Model 2 and Model 6 synthetic scenes, showing superior performance to Segmented ISAC and FLAASH-IR. From Table 5, it may be seen that very similar atmospheric states were identified between OISAC and RD. The slight differences in temperature and water

concentration are hardly noticeable when viewing the transmission and path radiance plots.

In an effort to guide future RD global minimization searches, the error surface defined by Eq. 34 was computed for a few of the scenes in this study. The surface for the Model 2 synthetic scene is shown in Fig. 44. From both this surface and the one from the Model 6 scene, the error surfaces appear to behave in a somewhat smooth and continuous manner; both surface minima occurred within locally confined regions of the surfaces. These surface characteristics are certainly favorable for minimization techniques, and this knowledge could aid future algorithm optimization.

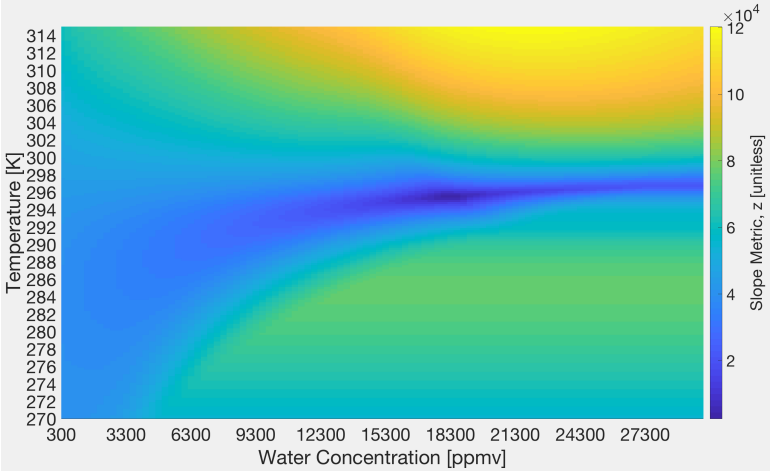

Figure 44. RD error surface for Model 2 dataset.

Structured Model 2 and Model 6 Scenes.

The next set of scenes, the ones given an emissivity and temperature structure derived from the Mako scene, add an additional level of complexity. Since RD uses range-dependent data from throughout the image to find the atmospheric state which detrends best, the chief purpose for testing these scenes was to add more realistic scene material and temperature distributions which would challenge RD. The atmospheric state for these scenes are similar, but not identical to the Model 2 and Model 6

atmospheres. They have ground water concentrations of 18300 ppmv and 7800 ppmv and both have ground air temperatures of 310 K. Comparing rows of Model 2 and 6 with Structured 2 and 6 in Table 5, the water concentrations for these new scenes resemble those used in the previous scenes.

Overall, only OISAC show slightly degraded performance for these new synthetic scenes, identifying slightly cooler and drier atmospheres for each. RD perfectly identified both atmospheric states. Transmission and path radiance differences with respect to truth for OISAC minimal. For the Structured 2 scene, OISAC had mean spectral errors on the order of 0.0015%, and for the Structured 6 scene, OISAC had a mean spectral error in transmission and path radiance on the order of 0.002%.

Despite the performance of both AC algorithms, the impact on the target detection statistics (i.e. correlation and mean spectral RMS, see 2.7) was more evident, mostly due to the added sensor noise. Identical to the process outlined in 3.4, the true temperature map was used to retrieve emissivities for every pixel in the scene for given estimates of the atmospheric transmission, path radiance, and downwelling radiance. An average emissivity for each class was then calculated using the known material distribution. TES results from the first dozen spectral bands, corresponding to $7.57 - 8.11 \mu m$, were excluded; significant transmission losses in this region significantly degraded performance for both scenes/algorithms. Target detection algorithms would most likely exclude other low transmission spectral bands; however, the rest of the bands will be included in the current analysis. Table 6 and Table 7 shows the correlation and mean RMS error between the truth and average retrieved emissivity for each class for the Structured 2 and Structured 6 scenes respectively. In these, one may see that because RD perfectly identified the atmospheric state, it has a mean correlation very close to one and a mean RMS error near zero for all of the materials in the Structured 6 scene and for but aluminum and water in the Structured 2

scene. Since the atmosphere was identified correctly and temperature emissivity was performed perfectly (i.e. the true temperatures were used to solve for the emissivity), the only impact which could have degraded performance was sensor noise. One would expect that low transmission spectral channels would have the worse performance, since the signal to noise ratios in these channels are worst; additionally, since the Structured 2 scene has a larger water concentration, leading to lower atmospheric transmission, Structured 2 is expected to have larger errors in retrieved emissivities. Plotting the retrieved emissivities for aluminum and water for the Structured 2 scene in Fig. 45, the maximum spectral errors in retrieved emissivity may be matched with the minima in the transmission spectra (shown in the center of Fig. 41. The spectrally flat nature of aluminum and water magnified this impact from noise on the spectral correlation. Finally, in Fig. 46 emissivity results for aluminum and deciduous are shown for the Structured 6 scene. OISAC had the worse performance for these materials. Aluminum had relatively high error due to its low emissivity; since the strongest signal in the LWIR is typically from the emissive component, shown earlier in Fig. 2, aluminum's low emissivity would result in a smaller signal to noise ratio. These results highlight that there will nearly always be performance degradation due to noise, even for a perfectly compensated scene and temperature truth data.

When compared with the previous synthetic scenes, there are many differences which may have impacted performance, particularly for OISAC. Much hotter material temperatures ($\sim$320 K) and larger temperature variances ($\sim$7 K) were present in these structured scenes. Additionally, the material composition of the scene was very different. There were nearly half as many different scene materials, no true blackbody materials, and a small amount of reflective pixels. The scene geometry was also completely different, showing far less range variability than the previous scenes. Since both OISAC and RD rely on the changing geometry to improve at-

Structured 2 Emissivity Results				
	Correlation		Mean RMS Error	
	RD	OISAC	RD	OISAC
Green Paint	1.000	0.997	0.000	0.002
Aluminum	0.309	0.008	0.002	0.048
Water	0.103	0.035	0.002	0.009
Brown Loam	1.000	1.000	0.000	0.008
Roof Slate	1.000	0.999	0.000	0.004
Asphalt	1.000	0.936	0.000	0.005
Deciduous	1.000	0.628	0.000	0.006
Concrete	1.000	0.948	0.000	0.004

Table 6. Emissivity results from the Structured 6 scene. Correlation and mean RMS error were between the mean retrieved emissivity and truth.

Structured 6 Emissivity Results				
	Correlation		Mean RMS Error	
	RD	OISAC	RD	OISAC
Green Paint	1.000	0.996	0.000	0.001
Aluminum	1.000	0.154	0.000	0.020
Water	1.000	0.971	0.000	0.004
Brown Loam	1.000	1.000	0.000	0.002
Roof Slate	1.000	1.000	0.000	0.002
Asphalt	1.000	0.975	0.000	0.002
Deciduous	1.000	0.707	0.000	0.003
Concrete	1.000	0.978	0.000	0.002

Table 7. Emissivity results from the Structured 6 scene. Correlation and mean RMS error were between the mean retrieved emissivity and truth.

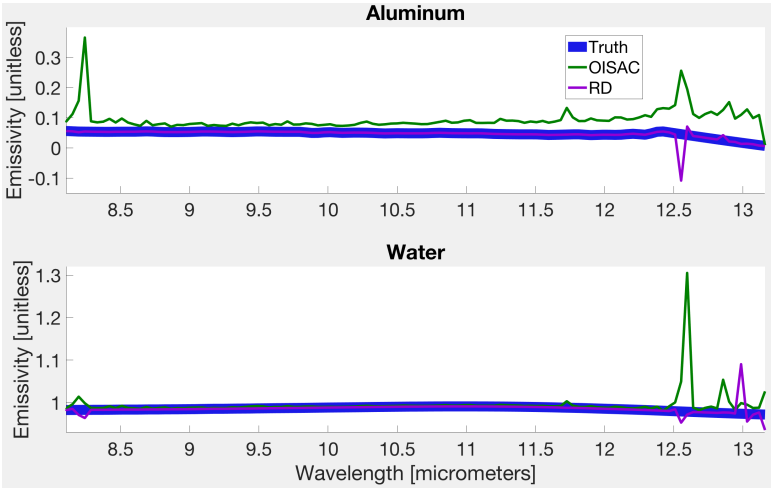

Figure 45. Emissivity retrieval results for aluminum and water for the Structured 2 scene. Regions of larger error are due to low transmission channels where noise played a dominant factor.

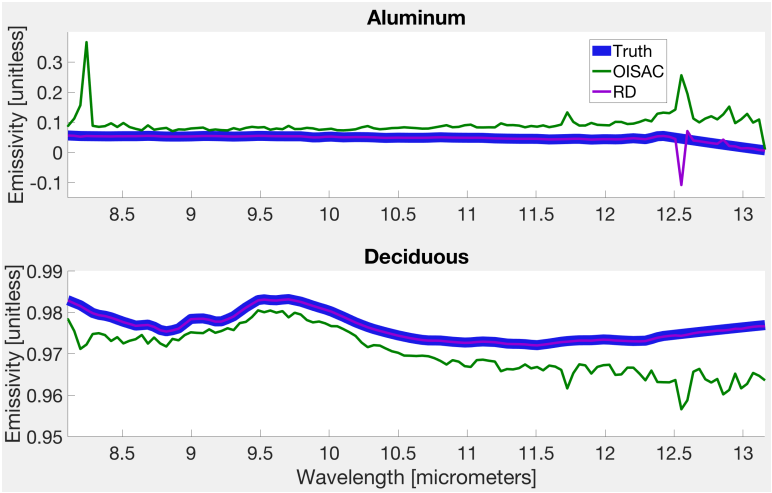

Figure 46. Emissivity retrieval results for aluminum and deciduous for the Structured 6 scene. Regions of larger error are due to low transmission channels where noise played a dominant factor.

mospheric estimates, this reduction in range-dependence information is expected to degrade performance. The number of pixels in each row and the range variation between subsequent rows was also different between the two scenes, which could further impact results. Additional analysis would be needed to identify the leading causes for performance degradation.

Mako Scene.

The application of the RD technique to the Mako scene is an crucial one. Up until now, RD had solely been applied to synthetic scenes. Unlike OISAC, which has roots in a technique that has been used throughout the scientific community for nearly two decades, RD had never been applied to real-world hyperspectral imagery. From Table 5, one may see that RD and OISAC identify similar atmospheric states. Transmission and path radiance results are shown in Fig. 47. Very little spectral differences between spectra from OISAC and RD may be seen, with RD showing slightly smaller transmission and greater path radiance due to its slightly higher estimate of water concentration. It is interesting to note that these two completely different techniques yielded nearly the same results. While both techniques chose to model the atmosphere in a similar manner (i.e. ignoring effects of ozone and characterizing an atmospheric state with a ground air temperature and water concentration), they approach atmospheric compensation from very different perspectives and yet are seemingly consistent.

Since truth data is unknown for the Mako dataset, one is left with similar analysis tools as employed in 3.4. First, the colormap of the squared correlation between retrieved emissivities and the atmospheric transmission for the Mako scene is shown (as before, the first dozen spectral bands were excluded because of transmission losses). This is shown in Fig. 48. Retrieved emissivities via RD show a reduced correlation

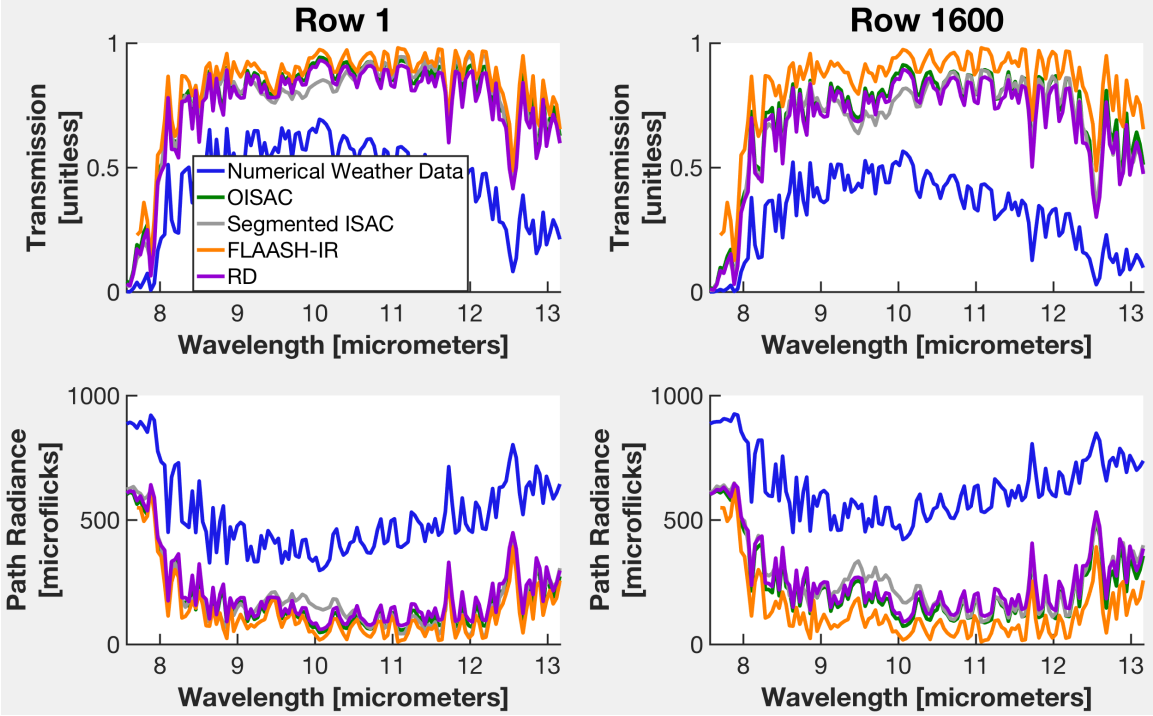

Figure 47. Transmission and path radiance results for the first and last rows of the Mako scene. Results from the numerical weather data are also shown.

with atmospheric transmission, though they are close as detailed in Fig. 49. Next, the same river emissivity analysis was performed as before, where the emissivity of water was used to retrieve a spectral temperature and then used the mean spectral temperature to compute an emissivity. The mean spectral temperature from RD gave the close river a temperature of 295.9 ± 0.3 K and the far river a temperature of 299.6 ± 0.4 K. Both of these are comparable to OISAC which, to significant figures, had the nearly the same predicted temperature and uncertainty; OISAC showed slightly less temperature uncertainty. Comparing the mean spectral RMS difference between the retrieved emissivity and known emissivity of water, OISAC had an mean RMS of 0.0054 while RD had a mean RMS of 0.0065. OISAC still shows the lowest error, but RD has less than the next closest (FLAASH-IR at 0.0067). Altogether, these results suggest that RD is able to perform AC on real-world hyperspectral imagery comparable to the other techniques.

In Fig. 50 the RD error surface for the Mako scene is shown. Just as in Fig. 44, the surface appears to have a smooth and continuous behavior with locally confined minima. This suggests that determining the optimum atmospheric state for even real-world hyperspectral imagery may be a well-conditioned problem.

Reflective Scene.

One advantage of RD over AC techniques similar to ISAC or OISAC is that it does not require blackbody pixels. To test this assertion, a new synthetic scene was generated using the exact same conditions for the Model 6 synthetic scene, except that the materials were specifically chosen to have low emissivities in the 11.7 μm water band. The highest material emissivity for that particular spectral region, which OISAC relies on exclusively to compensate, was about 0.9. The new selection of materials from the ASTER database and their emissivities are shown in Fig. 51.

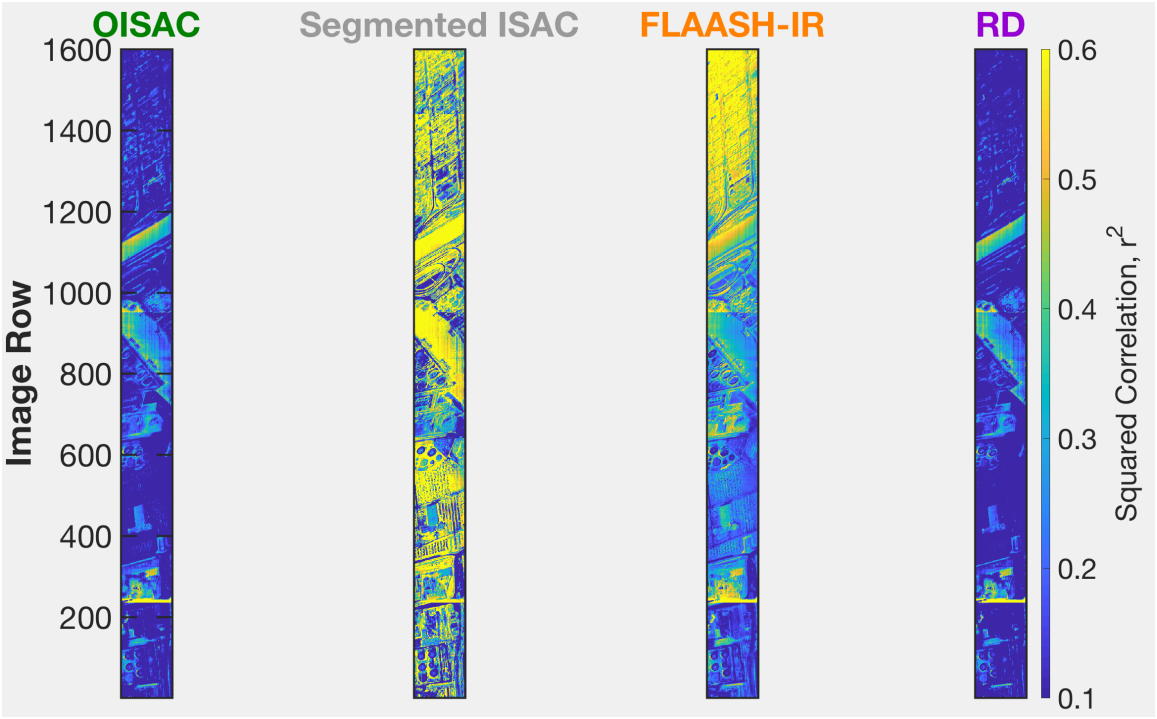

Figure 48. Colormap of the squared correlation between retrieved emissivities and the atmospheric transmission for the Mako scene. RD does not exhibit range-dependent correlation between retrieved emissivity and transmission and shows least correlation overall.

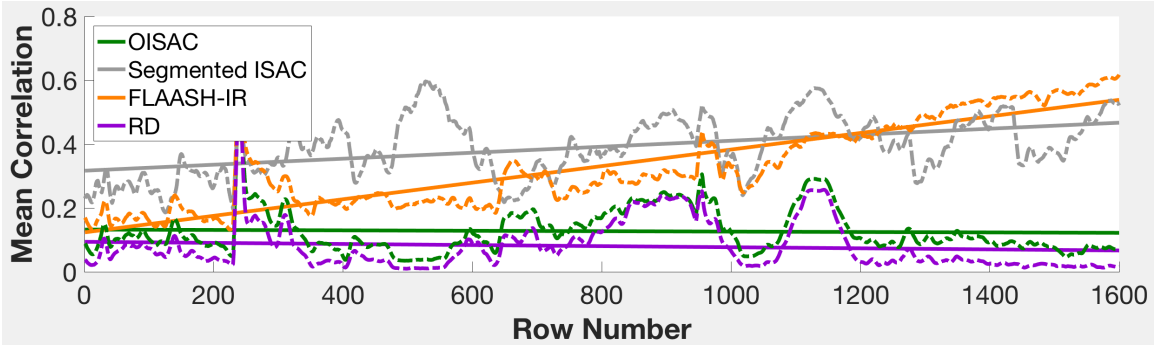

Figure 49. Plot of the squared correlation between retrieved emissivities and the atmospheric transmission for the Mako scene. RD does not exhibit range-dependent correlation between retrieved emissivity and transmission and shows least correlation overall.

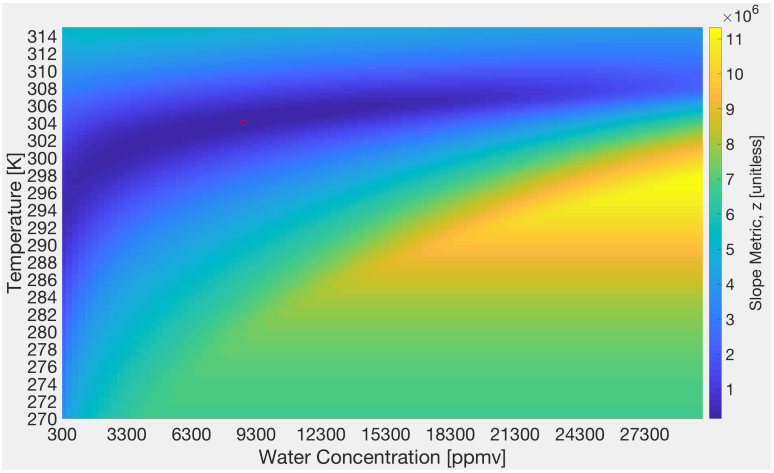

Figure 50. RD error surface for the Mako dataset.

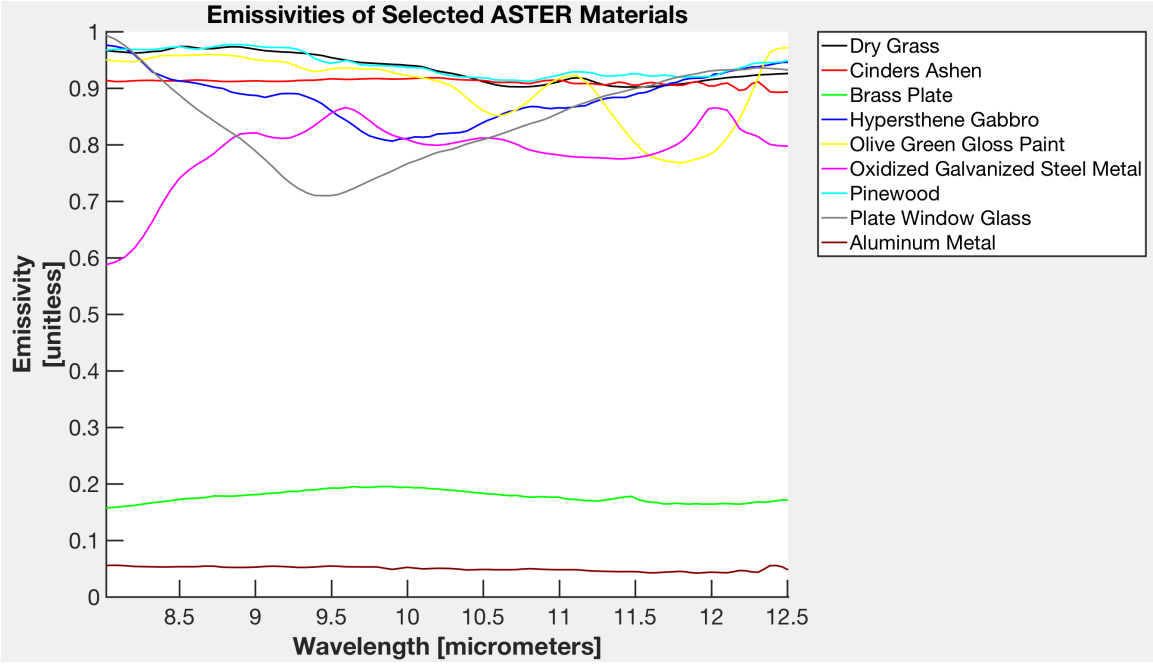

Figure 51. Emissivities of reflective materials.

Transmission and path radiance results for the first and last row using OISAC, RD, Segmented ISAC, and FLAASH-IR are shown in Fig. 52. As expected, since OISAC assumes the existence of at least some materials with an emissivity near unity in the 11.7 μm water band, the fact that they did not exist in the scene limited OISAC's ability to identify the correct atmosphere. ISAC does especially poorly, vastly under and over estimating the transmission and path radiance respectively. FLAASH-IR, which does not require true blackbody pixels, is relatively good at compensating for the first row of the image, but because it does not incorporate range-dependence, it incorrectly compensates for the last row of the scene. Unlike these other AC techniques, RD is almost entirely unaffected and only required additional iterations.

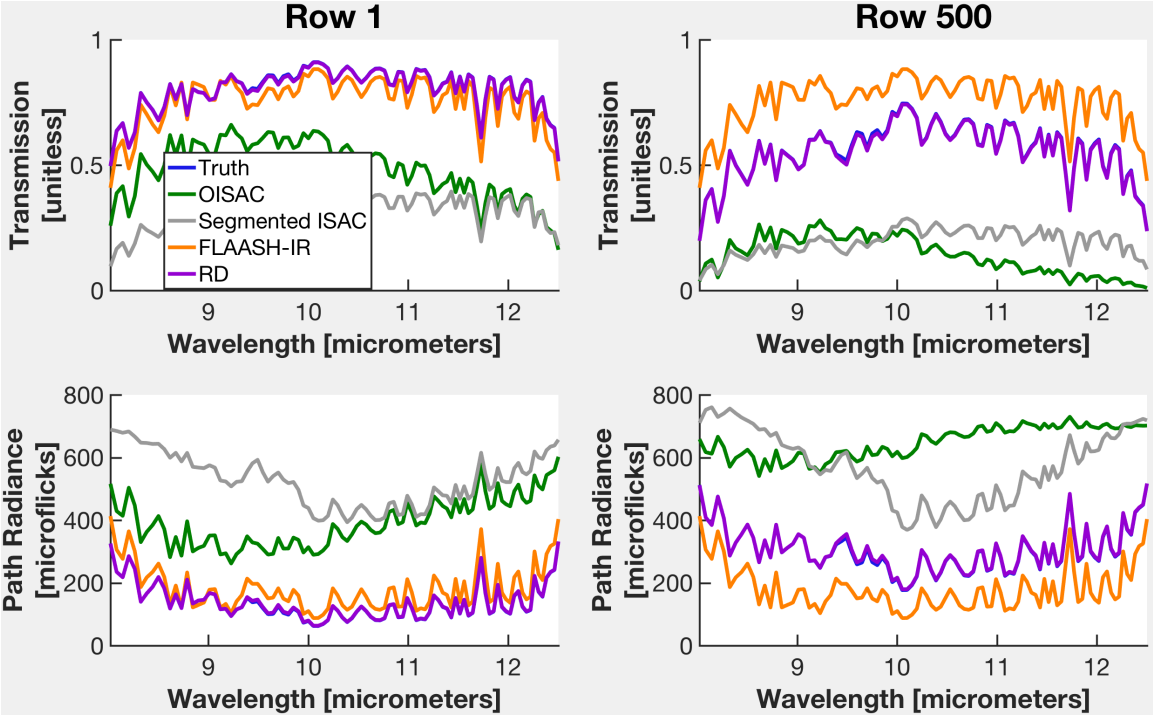

Figure 52. Atmospheric compensation results for the reflective scene. OISAC and ISAC, which rely on blackbody-like pixels, had difficulty compensating this scene. RD results closely matched truth spectra.

This case example highlighted a strength of the RD technique; however, there may be additional complications with highly reflective scenes that have not been considered. Real-world hyperspectral imagery under these conditions is necessary before any firm conclusions can be made. This imagery would help provide additional insight into the limitations of RD.

Variable Downwelling Scenes.

Here the impact of variable downwelling radiance, i.e. $\delta L_d \neq 0$ in Eq. 32, is investigated. Variable downwelling radiance could occur if objects had surface normals oriented in directions different than each other or if the material's reflective properties acted more specular than Lambertian. The first case is likely for any scene and is even more pronounced if the second case is also true. Since reflective materials in general tend to exhibit more specular features and since the second component of the ground-radiance uncertainty in Eq. 32 is increased for reflective materials (since emissive materials will have a small reflective component), the variable downwelling was introduced to the reflective scene described in 4.3.

To begin the analysis, the variability of the downwelling radiance for five different viewing angles was explored. This result is shown in Fig. 53. As expected from the discussion in 2.2, downwelling radiance is a minimum when coming from directly overhead (0 degrees) and a maximum towards the horizon (80 degrees). Downwelling from the horizon is larger because the atmospheric path is longer, particularly through the first couple kilometers of the atmosphere where the water concentration is greatest.

Next, every pixel in the reflective scene were assigned a random angle, corresponding to its orientation and thus the downwelling contribution it would experience. After generating the scene with the variable downwelling contributions, it was processed

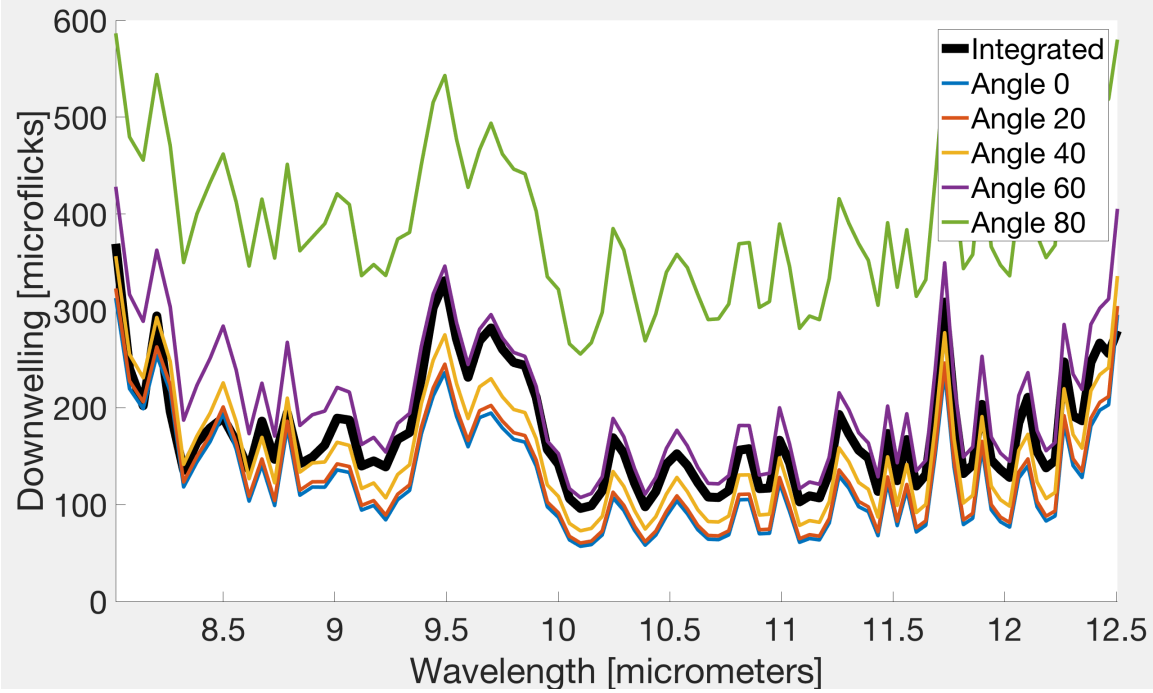

Figure 53. Variation of downwelling radiation. Zero degree corresponds to directly overhead; 80 degrees is towards the horizon.

with the full suite of AC algorithms used thus far. The transmission and path radiance results are shown in Fig. 54. As expected, this scene is slightly more challenging for RD; however, within three iterations RD still outperforms the other algorithms and successfully settles on the best-match atmospheric state.

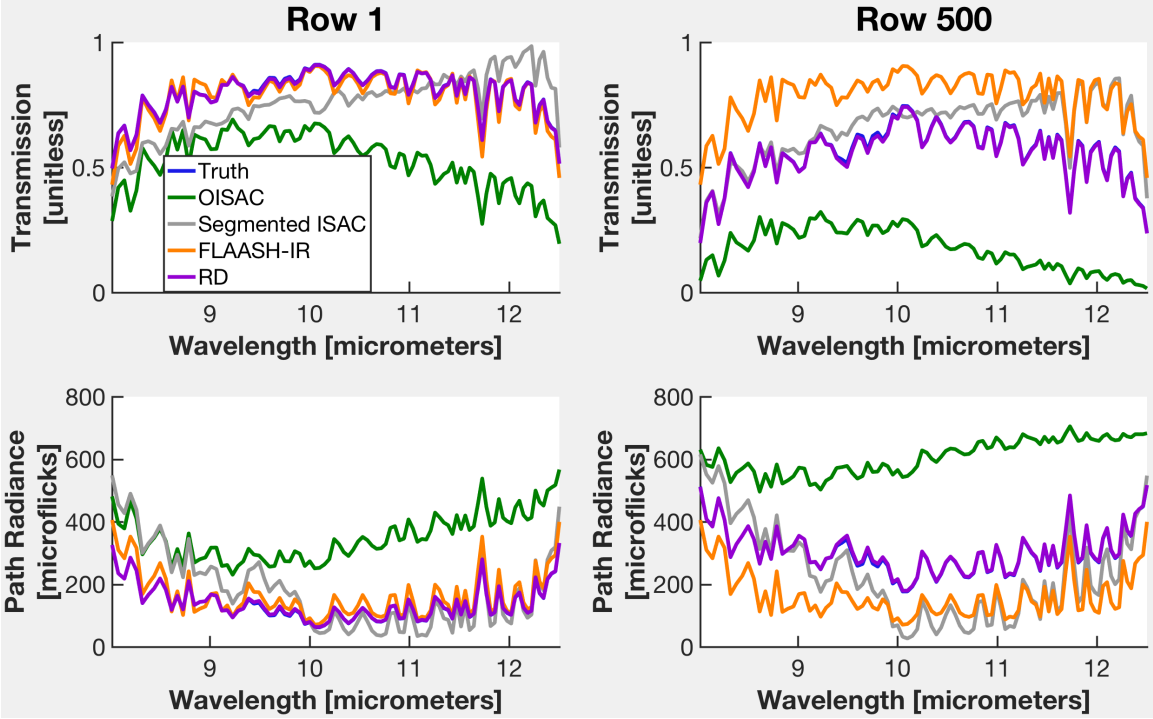

Figure 54. Atmospheric compensation results for the reflective scene that also had variable downwelling radiance contributions. OISAC and ISAC, which rely on blackbody-like pixels, had difficulty compensating this scene.

4.4 RD Conclusions

RD is a brand-new AC technique that uses the oblique geometry to identify the atmospheric state. It has shown comparable performance to the OISAC technique for the standard scenes tested and superior performance for scenes lacking the blackbody materials OISAC critically relies upon.

Because it is a new technique, there are many areas in which RD needs to be

refined and tested. Specifically, RD could possibly be improved with better separation of scene pixels into their appropriate classes. Alternatively, it may be possible to develop an entirely new method which still aims to detrend the observed radiance but using different means/metrics. The underlying theory presented here would still be valuable in developing this alternative method. Finally, testing RD with additional synthetic and real-world oblique hyperspectral imagery where truth is known for a variety of atmospheric conditions and scene materials would provide further insights as to its limitations.

V. Conclusions

This work presents novel contributions to the field of LWIR oblique atmospheric compensation. Utilizing physics-based radiative transfer models, two new techniques were developed to compensate oblique hyperspectral imagery and compared with standard LWIR atmospheric compensation techniques. These advancements are expected to improve the capability of successfully interpreting LWIR hyperspectral imagery in oblique environments, and the analysis and development of the oblique physics-based models presented here may help guide future research in oblique atmospheric compensation.

To conclude, a summary and discussion of the key contributions from this study will be presented along with possible extensions of this research.

5.1 Summary of Key Contributions

Various contributions were made as a result of this research. Direct contributions include the creation of two oblique AC algorithms. Indirect contributions include impacts which may affect other AC algorithms; these contributions were by-products of this research.

Direct Contributions.

Two distinct algorithms were developed to improve atmospheric compensation of oblique hyperspectral imagery.

1. **Oblique In-Scene Atmospheric Compensation (OISAC).** OISAC, based on an adaptation of the scaling procedure of ISAC, fits a polynomial-based surface to obtain more accurate estimates of the transmission and path radiance line contributions. By incorporating the range dependence of these atmospheric

features, these parameters are more accurately estimated for use in identification of the atmospheric state. Additionally, by weighting the relative uncertainty in estimates of these two parameters, improvements were made in matching these estimates to the correct atmospheric state, an improvement that could be incorporated into the standard (i.e. non-oblique) ISAC technique.

2. **Radiance Detrending (RD).** RD is a novel technique, developed by analyzing the geometrical impact on the observed radiance. The observed radiance has a noticeable trend due to range-dependent transmission and path radiance, and this technique identifies the correct atmospheric state by testing various atmospheres and determining which one best detrends the observed radiance. This technique was refined by separating the scene into distinct classes via k-means clustering and shows promise in compensating hyperspectral imagery without blackbodies, a key disadvantage of ISAC and OISAC.

Performance of both techniques were analyzed and compared with standard LWIR atmospheric techniques using a combination of synthetic and measured hyperspectral imagery. In simulated hyperspectral data where truth was known, both OISAC and RD outperformed the standard toolbox of techniques. They compared similarly with each other in the simple synthetic scenes, closely matching truth spectra; however, for the scene without blackbody-like pixels, OISAC's performance was significantly degraded. RD had no difficulty handling this reflective scene, including the scene where randomized downwelling contributions were added. For the real-world hyperspectral imagery, because truth data was unknown, conclusions were more elusive. RD and OISAC identified similar atmospheric states for the measured imagery and exhibited fewer range artifacts compared to the other techniques, but the accuracy and limitations of all the techniques was difficult to ascertain.

Indirect Contributions.

During the development of the two oblique AC algorithms, several indirect contributions were also made.

1. **Analysis of range-dependent transmission and path radiance** There is no other study known by the authors which specifically explores and models the range-dependence of transmission and path radiance across an oblique scene. While modeling and analyzing this was straight-forward, finding multiple means of incorporating these models into the AC algorithms was not. In this research, techniques to use this information rather than be hindered by it were discovered.

2. **ISAC improvements** When building OISAC, several improvements were made to the standard ISAC procedure, particularly for the "Full ISAC". These include two new methods of estimating atmospheric line contributions other than running MODTRAN separately in transmission mode. This cuts MODTRAN's use in half for the database generation. Additionally, the standard scaling equation used by ISAC was greatly simplified; it is now more intuitive and does not require use of the net radiance depression nor trapezoidal integration. Finally, use of the relative uncertainty of the line contributions due to transmission and path radiance improves ISAC's ability to select the proper atmospheric state.

3. **AAC and ISAC comparison** This research identified that the AAC technique is identical to the scaling technique in ISAC, with chief differences being the derivation and nomenclature. With the more intuitive scaling equation developed here for ISAC (above), this was able to be more clearly identified. This ties together two of the more popular LWIR AC techniques.

4. **FLAASH-IR segmentation** The use and performance of FLAASH-IR segmentation in analyzing oblique scenes had not been previously reported in the

literature. Initial results suggest that improved FLAASH-IR performance for oblique scenes is possible via segmentation; however, further analysis is still needed to better understand the sensitivity of this modified technique for different size subimages.

5.2 Discussion of Key Contributions

In this research, the first ever data-driven AC technique built specifically to incorporate path range changes within a scene was developed. The second was also developed. These two techniques are the only ones of their kind, specifically designed to utilize the range-dependence information within oblique scenes.

Standard data-driven techniques were not designed for scenes with variable path length and have only been able to analyze oblique scenes by segmenting images into parts and analyzing them separately. There are several problems with this type of analysis. First, by analyzing smaller portions of the scene at a time, the algorithms may have degraded performance in analyzing each individual scene since they have less data for a given iteration. Additionally, even after segmentation, the subimage will still have range-dependence within it; this is especially evident for highly oblique scenes or larger subimages. Third, these algorithms currently require direct supervision to balance these previous two considerations; they cannot divide a scene too finely without compromising algorithm statistics nor too loosely or else the range dependence will still be dominant. Last, since segmented techniques analyze portions of a scene independently, they lose the extra information inherent to an oblique scene, specifically the information of how the atmosphere is changing with range. The techniques developed here do not share these limitations.

When comparing OISAC and RD with standard AC techniques on the synthetic scenes, the benefit of incorporating range-dependence is evident. Transmission and

path radiance errors are orders of magnitude smaller than for the standard techniques. Mean RMS error and correlation of the retrieved emissivities with truth data for the nearly two dozen materials tested were nearly ideal for both humid and dry atmospheric states. The largest discrepancy arose when OISAC, a technique that requires materials with near blackbody-like features over the 11.73 μm water band, attempted to compensate for a synthetic scene where the materials were specifically chosen because of their low emissivities over the water band. OISAC and Segmented ISAC showed the largest errors; however, such a scene may not be common and when encountering such a scenario, OISAC should not be the first tool one picks to analyze such a scene.

Regarding the real-world hyperspectral imagery, since truth data was unknown, firm conclusions regarding performance are difficult to make. Numerical weather data suggested an atmospheric state with twice the path radiance and half the transmission as every AC algorithm applied, further highlighting the difficulty in analyzing the data. Despite these challenges, OISAC and RD, two techniques which operate in completely different manners, suggested similar transmission and path radiance estimates. Additionally, after applying TES techniques to the image, emissivities retrieved by the two techniques were the least correlated with atmospheric transmission. Alternatively, emissivities retrieved with FLAASH-IR and Segmented ISAC were much more correlated with the atmospheric transmission and showed evident range dependence, suggesting that parts of the image were better compensated than others. Segmentation and range-dependent artifacts from improper compensation were also evident in retrieved temperatures.

5.3 Roadmap for Future Efforts

While the development and analysis presented here is promising, this work is only an initial step in developing a suite of robust and accurate oblique atmospheric compensation tools. The effectiveness of these techniques requires further testing, and there are numerous aspects of the techniques which may be improved upon.

Oblique Imagery Generation and Collection.

The most direct means of advancing future oblique AC work involves testing these algorithms against additional oblique datasets. This may include both more complex and realistic synthetic scenes as well as real-world hyperspectral imagery, with a variety of atmospheric conditions, viewing geometries, and scene compositions. The advantage of working with synthetic scenes is the relative ease to set them up, the ability to gradually introduce increasingly more challenging and realistic conditions, and the fact that truth spectra are known. As RD is not based on a previous AC algorithm such as ISAC, which has been applied to numerous synthetic and real-world datasets the past 15 years, testing of this technique is more critical. RD compensated all synthetic scenes used in this research with near perfection. While this is desirable, it does not provide much insight into its limitations. Testing with additional real-world datasets where truth is known would also be beneficial, as some sensor artifacts are difficult to model; this series of testing would showcase algorithm limitations or provide confidence in these new techniques.

Since oblique imagery typically spans larger swaths of area, it may have additional complications not as common to nadir-collected imagery. In these more expansive scenes, there may be significant changes in the water/temperature profiles or elevation across a scene. Testing these oblique AC techniques and modifying them to account for these effects is another possible area for further research.

OISAC Improvements.

One means of potentially improving OISAC could be via modeling transmission and path radiance with a non-polynomial function. This may improve the estimates of the line contributions and lead to better identification of the atmospheric state. Also, perhaps the atmospheric database could be improved to include atmospheric states other than those defined by (T_0,C_0) pairs. This could include ozone, carbon dioxide, or alternative lapse rates for the temperature and water concentration. However, it is not known whether inclusion of these additional parameters will actually benefit the atmospheric compensation process for the low-altitude observation conditions considered here (i.e. <10km), as limitations due to noise and non-blackbody pixels may dominate. Lastly, modifications to improve OISAC's ability to compensate scenes without blackbody pixels may be made. There may be techniques to estimate the highest emissivities in a scene, and then adjust line contribution estimate to account for lower emissivities (via the forward-modeling process used here). Improved techniques to identify blackbody-like materials within a scene would also improve OISAC.

RD Improvements.

One means of advancing RD is to improve its ability to properly cluster materials. As the purpose of this research was not aimed at optimizing the clustering process, but rather in gauging the efficacy of an oblique atmospheric compensation technique based on radiance detrending, the clustering process has not been optimized. Clustering with k-means was applied to the top quarter most transmissive bands to divide data into ten clusters (synthetic scenes used here were composed of eight or 23 different materials). Perhaps using a smaller number of wavelength bands or larger number of material classes are preferable, and maybe the best option depends on viewing

conditions or scene composition. It may also be helpful to explore the impact of selecting an incorrect atmosphere on clustering. This incorrect atmosphere might be from a previous iteration of RD or one chooses to initially seed RD with a range-dependent atmospheric state (e.g. from OISAC).

The detrending step could also be advanced. One practical limitation of RD is its ability to quickly arrive at an optimal atmospheric state. While improvements to the material clustering step could reduce the number of iterations needed to stabilize on the optimal state, the speed of the iterations could also be improved. This could be done by further limiting the number of spectral bands explored, skipping material classes which meet certain criteria, or developing an algorithm to automatically and intelligently search for the surface minimum. One could also use a finer temperature and humidity grid spacing or even abandon use of an atmospheric database altogether and instead compute MODTRAN atmospheres on the fly, though this may slow performance. Also, similar to OISAC, it may be helpful to explore atmospheric states other than those defined by a (T_0,C_0) pair. Future work should also include a stress-test of RD's ability to stabilize on a final atmospheric state; while RD converged to a single atmospheric state for every scene tested, because it is by nature an iterative algorithm, this may not always be the case. If studies demonstrate that it oscillates between atmospheric states, a different stopping criteria will need to be chosen. Finally, it may be possible to develop an entirely new method which still aims to detrend the observed radiance but using a different metric, possibly changing weighting of the various material classes and wavelength bands or how the uncertainty term is used. It may also be helpful to scale (e.g. dividing by the number of bands/material classes) and possibly express the metric in terms of physical units (e.g. incorporating microflicks) to aid analysis efforts; this may be helpful in comparing the detrending process of two different iterations or scenes.

Oblique Adaptation of Other AC Algorithms.

Since FLAASH-IR relies on maximizing smoothness for diverse pixels throughout the scene using an atmospheric database, developing an oblique version of FLAASH-IR may be fairly straight-forward. Possible modifications can include utilizing different atmospheric databases for the different rows of the image. Results from the different rows may need to be weighted as there would be smaller material signals at further ranges.

One simple means to adapt any generic atmospheric compensation technique would involve compensating, matching, and then forward-modeling. First, atmospheric compensation could be performed on the closest segment of the image. Then, this atmosphere could be matched with a transmission and path radiance profile from within an atmospheric database. Finally, this new state could be forward-modeled to account for the entire range. Alternatively, a more complex version would perform atmospheric compensation for various segments of the image and then leverage a metric which determines the best atmospheric match across all segmented images. Benefits of either of these techniques are that they can quickly and easily add range-variation to any standard algorithm while also avoiding segmentation artifacts which had previously explored with Segmented ISAC. However, there are limitations, such as the fact that potentially less atmospheric data is being leveraged for any individual compensation and the ideal size of the segments would require manual supervision, as it would most likely change with the scene geometry or atmospheric state.

5.4 Concluding Remarks

The field of oblique atmospheric compensation is a new one, and there is considerable room for improvement. As the scientific community continues to collect additional oblique hyperspectral datasets, so will its ability to develop, refine, and

test methods of compensating them. With further research in this field, the challenges of analyzing oblique hyperspectral imagery may turn into benefits, leveraging content about the atmosphere contained in the range-dependence of the apparent radiance.

Bibliography

1. Adler-Golden, SM, P Conforti, M Gagnon, P Tremblay, and Martin Chamberland. "Long-wave infrared surface reflectance spectra retrieved from Telops Hyper-Cam imagery". *Proc. SPIE*, volume 9088, 90880U. 2014.

2. Adler-Golden, Steven M, Lawrence S Bernstein, Michael W Matthew, Robert L Sundberg, and Anthony J Ratkowski. *Atmospheric compensation of extreme off-nadir hyperspectral imagery from Hyperion*. Technical report, SPECTRAL SCIENCES INC BURLINGTON MA, 2007.

3. Atkinson, Gary, Edwin R Hancock, et al. "Recovery of surface orientation from diffuse polarization". *Image Processing, IEEE Transactions on*, 15(6):1653–1664, 2006.

4. Baldridge, AM, SJ Hook, CI Grove, and G Rivera. "The ASTER spectral library version 2.0". *Remote Sensing of Environment*, 113(4):711–715, 2009.

5. Berk, Alexander, Patrick Conforti, Rosemary Kennett, Timothy Perkins, Frederick Hawes, and Jeannette van den Bosch. "MODTRAN6: a major upgrade of the MODTRAN radiative transfer code". *SPIE Defense+ Security*, 90880H–90880H. International Society for Optics and Photonics, 2014.

6. Bishoff, Josef P, David W Messingerb, and Emmett J Ientiluccib. "Oblique hyperspectral target detection". *Proc. of SPIE Vol*, volume 7086, 70860O–1. 2008.

7. Borel, Christoph. "Error analysis for a temperature and emissivity retrieval algorithm for hyperspectral imaging data". *International Journal of Remote Sensing*, 29(17-18):5029–5045, 2008.

8. Cheng, Li-Jen and George F Reyes. "AOTF polarimetric hyperspectral imaging for mine detection". *SPIE's 1995 Symposium on OE/Aerospace Sensing and Dual Use Photonics*, 305–311. International Society for Optics and Photonics, 1995.

9. Eismann, Michael Theodore. "Hyperspectral remote sensing". SPIE Bellingham, 2012.

10. Felton, M, KP Gurton, JL Pezzaniti, DB Chenault, and LE Roth. "Measured comparison of the crossover periods for mid-and long-wave IR (MWIR and LWIR) polarimetric and conventional thermal imagery". *Optics express*, 18(15):15704–15713, 2010.

11. Fortin, Gilles, Jean-Marc Thériault, and Paul Lacasse. "LWIR polarization sensing: investigation of liquids and solids with MoDDIFS". *SPIE Optical Engineering+ Applications*, 88730H–88730H. International Society for Optics and Photonics, 2013.

12. Gartley, Michael G. *Polarimetric modeling of remotely sensed scenes in the thermal infrared*. Ph.D. thesis, Citeseer, 2007.

13. Goudail, François, Patrick Terrier, Yoshitate Takakura, Laurent Bigue, Frédéric Galland, and Vincent DeVlaminck. "Target detection with a liquid-crystal-based passive Stokes polarimeter". *Applied Optics*, 43(2):274–282, 2004.

14. Gu, Degui, Alan R Gillespie, Anne B Kahle, and Frank D Palluconi. "Autonomous atmospheric compensation (AAC) of high resolution hyperspectral thermal infrared remote-sensing imagery". *IEEE Transactions on Geoscience and Remote Sensing*, 38(6):2557–2570, 2000.

15. Gurton, Kristan P and Melvin Felton. "Remote detection of buried land-mines and IEDs using LWIR polarimetric imaging". *Optics express*, 20(20):22344–22359, 2012.

16. Gurton, Kristan P, Alex J Yuffa, and Gorden Videen. "LWIR polarimetry for enhanced facial recognition in thermal imagery". *SPIE Sensing Technology+ Applications*, 90990G–90990G. International Society for Optics and Photonics, 2014.

17. Hall, Jeffrey L, Richard H Boucher, Kerry N Buckland, David J Gutierrez, Eric R Keim, David M Tratt, and David W Warren. "Mako airborne thermal infrared imaging spectrometer: performance update". *SPIE Optical Engineering+ Applications*, 997604–997604. International Society for Optics and Photonics, 2016.

18. Howe, James D, Miranda A Miller, Robert V Blumer, Thomas E Petty, Mark A Stevens, David M Teale, and Matthew H Smith. "Polarization sensing for target acquisition and mine detection". *International Symposium on Optical Science and Technology*, 202–213. International Society for Optics and Photonics, 2000.

19. Iannarilli Jr, Frank J, Herman E Scott, and Stephen H Jones. "Passive IR polarimetric hyperspectral imaging contributions to multisensor humanitarian demining". *Aerospace/Defense Sensing, Simulation, and Controls*, 346–352. International Society for Optics and Photonics, 2001.

20. Kjelgren, Roger and Thayne Montague. "Urban tree transpiration over turf and asphalt surfaces". *Atmospheric Environment*, 32(1):35–41, 1998.

21. LeMaster, Daniel A and Michael T Eismann. "Passive Polarimetric Imaging". *Multi-Dimensional Imaging*, 391–428, 2014.

22. Liou, Kuo-Nan. *An introduction to atmospheric radiation*, volume 84. Academic press, 2002.

23. Martin, Jake. *Passively estimating index of refraction for specular reflectors using polarimetric hyperspectral imaging*. Ph.D. thesis, Air Force Institute of Technology, 2016.

24. Meier, F, D Scherer, J Richters, and A Christen. "Atmospheric correction of thermal-infrared imagery of the 3-D urban environment acquired in oblique viewing geometry". *Atmospheric Measurement Techniques*, 4(5):909, 2011.

25. Meola, Joseph, Jason R Kaufman, and David L Perry. *Investigating The Effects Of Long Slant Paths For Longwave Infrared Hyperspectral Data Exploitation.* Technical report, DTIC Document, 2014.

26. Miyazaki, Daisuke, Masataka Kagesawa, and Katsushi Ikeuchi. "Transparent surface modeling from a pair of polarization images". *Pattern Analysis and Machine Intelligence, IEEE Transactions on*, 26(1):73–82, 2004.

27. Morel, Olivier, Christophe Stolz, Fabrice Meriaudeau, and Patrick Gorria. "Active lighting applied to three-dimensional reconstruction of specular metallic surfaces by polarization imaging". *Applied optics*, 45(17):4062–4068, 2006.

28. Nicodemus, Fred E. "Reflectance nomenclature and directional reflectance and emissivity." *Applied Optics*, (9):1474–5, 1970.

29. Nugent, Paul W, Joseph A Shaw, and Sabino Piazzolla. "Infrared cloud imaging in support of Earth-space optical communication". *Optics express*, 17(10):7862–7872, 2009.

30. Pezzaniti, J Larry, David Chenault, Kris Gurton, and Melvin Felton. "Detection of obscured targets with IR polarimetric imaging". *SPIE Defense+ Security*, 90721D–90721D. International Society for Optics and Photonics, 2014.

31. Pieper, Michael, Dimitris Manolakis, Eric Truslow, Thomas Cooley, Michael Brueggeman, John Jacobson, and Andrew Weisner. "Performance limitations of temperature–emissivity separation techniques in long-wave infrared hyperspectral imaging applications". *Optical Engineering*, 56(8):081804–081804, 2017.

32. Richter, PH. "Estimating errors in least-squares fitting". 1995.

33. Richter, Rudolf and Daniel Schläpfer. "Geo-atmospheric processing of airborne imaging spectrometry data. Part 2: atmospheric/topographic correction". *International Journal of Remote Sensing*, 23(13):2631–2649, 2002.

34. Rutledge, Glenn K, Jordan Alpert, and Wesley Ebisuzaki. "NOMADS: A climate and weather model archive at the National Oceanic and Atmospheric Administration". *Bulletin of the American Meteorological Society*, 87(3):327–341, 2006.

35. Sadjadi, Firooz A and CornellS L Chun. "Automatic detection of small objects from their infrared state-of-polarization vectors". *Optics letters*, 28(7):531–533, 2003.

36. Schlamm, Ariel and Brent Bartlett. *Challenges Of Off-nadir Hyperspectral Image Processing And Analysis.* Technical report, DTIC Document, 2014.

37. Shaw, Joseph, Paul Nugent, Nathan Pust, Brentha Thurairajah, and Kohei Mizutani. "Radiometric cloud imaging with an uncooled microbolometer thermal infrared camera". *Optics express*, 13(15):5807–5817, 2005.

38. Smith, Matt R, Alan R Gillespie, Hugau Mizzon, Lee K Balick, Juan Carlos Jiménez-Muñoz, and Jose A Sobrino. "In-scene atmospheric correction of hyperspectral thermal infrared images with nadir, horizontal, and oblique view angles". *International journal of remote sensing*, 34(9-10):3164–3176, 2013.

39. Surface Optics Corporation. *SOC-100 User's Manual*.

40. Takebayashi, Hideki and Masakazu Moriyama. "Study on the urban heat island mitigation effect achieved by converting to grass-covered parking". *Solar Energy*, 83(8):1211–1223, 2009.

41. Theriault, Jean Marc, Gilles Fortin, Paul Lacasse, and Francois Bouffard. "Imaging FTS for Hyperspectral Polarization Sensing in the LWIR: Application to Liquid Detection". *Fourier Transform Spectroscopy*, FW1D–4. Optical Society of America, 2013.

42. Tyo, J Scott, Bradley M Ratliff, James K Boger, Wiley T Black, David L Bowers, and Matthew P Fetrow. "The effects of thermal equilibrium and contrast in LWIR polarimetric images". *Optics express*, 15(23):15161–15167, 2007.

43. Voogt, James A and CSB Grimmond. "Modeling surface sensible heat flux using surface radiative temperatures in a simple urban area". *Journal of Applied Meteorology*, 39(10):1679–1699, 2000.

44. Wilson, Kody A. *Non-destructive Techniques for Classifying Aircraft Coating Degradation*. Technical report, DTIC Document, 2015.

45. Wolff, Lawrence B. and Terrance E. Boult. "Constraining object features using a polarization reflectance model". *IEEE Transactions on Pattern Analysis & Machine Intelligence*, (7):635–657, 1991.

46. Young, Stephen J, B Robert Johnson, and John A Hackwell. "An in-scene method for atmospheric compensation of thermal hyperspectral data". *Journal of Geophysical Research: Atmospheres*, 107(D24), 2002.

47. Zhan, Hanyu, David G Voelz, Xifeng Xiao, and Sang-Yeon Cho. "Polarization-based complex index of refraction estimation with diffuse scattering consideration". *SPIE Optical Engineering+ Applications*, 96130Y–96130Y. International Society for Optics and Photonics, 2015.

REPORT DOCUMENTATION PAGE

Form Approved
OMB No. 0704-0188

PLEASE DO NOT RETURN YOUR FORM TO THE ABOVE ADDRESS.

1. REPORT DATE *(DD-MM-YYYY)*	2. REPORT TYPE	3. DATES COVERED *(From - To)*
14 Sept 2017	Graduate Research Paper	Sept 2014 - Sept 2017

4. TITLE AND SUBTITLE

Oblique Longwave Infrared Atmospheric Compensation

5a. CONTRACT NUMBER

5b. GRANT NUMBER

5c. PROGRAM ELEMENT NUMBER

6. AUTHOR(S)

O'Keefe, Daniel S., Captain, USAF

5d. PROJECT NUMBER

5e. TASK NUMBER

5f. WORK UNIT NUMBER

7. PERFORMING ORGANIZATION NAME(S) AND ADDRESS(ES)

Air Force Institute of Technology
Graduate School of Engineering and Management (AFIT/EN)
2950 Hobson Way
Wright-Patterson AFB OH 45433-7765

8. PERFORMING ORGANIZATION REPORT NUMBER

AFIT-ENP-DS-17-S-030

9. SPONSORING/MONITORING AGENCY NAME(S) AND ADDRESS(ES)

AFRL/RYMT
Joseph Meola
2241 Avionics Circle
Wright-Patterson AFB, OH 45433
joseph.meola.1@us.af.mil

10. SPONSOR/MONITOR'S ACRONYM(S)

AFRL/RYMT

11. SPONSOR/MONITOR'S REPORT NUMBER(S)

12. DISTRIBUTION/AVAILABILITY STATEMENT

Distribution Statement A. Approved for Public Release; Distribution Unlimited

13. SUPPLEMENTARY NOTES

14. ABSTRACT

This research introduces two novel oblique longwave infrared atmospheric compensation techniques for hyperspectral imagery, Oblique In-Scene Atmospheric Compensation (OISAC) and Radiance Detrending (RD). Current atmospheric compensation algorithms have been developed for nadir-viewing geometries which assume that every pixel in the scene is affected by the atmosphere in nearly the same manner. However, this assumption is violated in oblique imaging conditions where the transmission and path radiance vary continuously as a function of object-sensor range, negatively impacting current algorithms in their ability to compensate for the atmosphere. The techniques presented here leverage the changing viewing conditions to improve rather than hinder atmospheric compensation performance. Initial analyses of both synthetic and measured hyperspectral images suggest improved performance in oblique viewing conditions compared to standard techniques.

15. SUBJECT TERMS

atmospheric compensation, hyperspectral imaging, longwave infrared, oblique, off-nadir

16. SECURITY CLASSIFICATION OF:			17. LIMITATION OF ABSTRACT	18. NUMBER OF PAGES	19a. NAME OF RESPONSIBLE PERSON
a. REPORT	b. ABSTRACT	c. THIS PAGE			Dr. Kevin C. Gross, AFIT/ENP
U	U	U	UU	148	19b. TELEPHONE NUMBER *(Include area code)* (937) 255-3636 x4558 kevin.gross@afit.edu